

A STUDY OF AQUATIC BIOMIMETIC PROBLEMS USING A MULTI-BODY DYNAMICS METHOD

Ruoxin Li

*A thesis submitted in fulfilment of the requirements for the degree of
Doctor of Philosophy*

Department of Naval Architecture, Ocean and Marine Engineering
University of Strathclyde
Glasgow

March 2021

Declaration

This thesis is the result of the author's original research. It has been composed by the author and has not been previously submitted for examination which has led to the award of a degree.

The copyright of this thesis belongs to the author under the terms of the United Kingdom Copyright Acts as qualified by University of Strathclyde Regulation 3.50. Due acknowledgement must always be made of the use of any material contained in, or derived from, this thesis.

Ruoxin Li

Signature: *Ruoxin Li* Date: 31/03/2021

Acknowledgements

First of all, I would like to express my sincere gratitude to my first supervisor Dr Qing Xiao for her continuous support and guidance throughout all phases of this work with her patience and expertise in CFD. Dr Xiao has devoted a great deal of time and effort to guiding me in my research, helping me with my life in the UK and encouraging me to be a better person, which is very much appreciated.

I would like to thank my second supervisor Prof Alexander Day for offering his help and invaluable advice on my PhD. His enthusiasm for life and work has always inspired me.

I am thankful to Dr Jianxin Hu for generously providing insightful suggestions and help to my PhD research. I would like to thank Mrs Thelma Will, Mrs Susan Pawson and all other staff in the department of NAOME for their kind help with all the administrative issues.

I would like to show my appreciation to my colleagues in the department of NAOME for assisting me in my research and all my friends in Glasgow for bringing lots of fun to my life in the past years.

I am deeply indebted to my parents for their everlasting love, support and encouragement. Being their daughter is the luckiest thing ever in my life. I am truly grateful to my beloved husband Dr Yuanchuan Liu for always keeping me company and making every day special. Finally, I would like to express my love to my daughter Miss Ruiyu Liu for her shining smiles and thunderous cries. Her fast growth pushes me to finish my PhD as soon as possible.

Abstract

To adapt themselves to the aquatic environment, fish have developed extraordinary propulsion and manoeuvring abilities. The physical and biological mechanisms observed in swimming fish can be applied to improve designs of Autonomous Underwater Vehicles (AUV), which can be used for the exploration of undersea resources. Fish swimming is a typical fluid-structure interaction problem, which involves several complicated mechanisms including vortex generation, the coupling of hydrodynamics and body-dynamics, as well as the interplay of fish body locomotion and the kinematics of multiple fins with flexural properties. Although relevant research has been carried out for several decades, there are still lots of phenomena behind aquatic swimming which are worth investigation. This work aims to improve the understanding of the underlying physics and sophisticated interactions in fish swimming. For this purpose, a coupled fluid-structure analysis tool is developed in the current thesis for solving aquatic biomimetic problems.

The developed numerical tool takes advantage of the commercial CFD software ANSYS Fluent to solve the fluid field surrounding swimming fish with high fidelity and utilises the theory of Multi-Body Dynamics (MBD) to simulate the complex locomotion of various types of fish swimming, such as the undulating motion of fish body, self-propelled motion of fish with flexible fins. The MBD theory is implemented in ANSYS Fluent as User Defined Function (UDF). The coupling of these two solvers is achieved by compiling and exchanging force and motion data between the UDF and ANSYS Fluent at each time step. Additionally, to tackle the complex mesh movement in fish swimming simulations, a dynamic mesh function is employed to regenerate and smooth deformed computational mesh.

A series of test cases is firstly studied to validate the various features of the tool, including three actuated connection cases (a discrete undulating fish, the undulating motion of a continuous Anguilliform fish, and the cupping motion of a fish peduncle-

caudal model) and one passive connection case (a flapping wing with two foils). Results obtained from all these cases meet well with previously published data, which successfully validate the coupled tool developed in this work.

Subsequently, the study of a pufferfish model driven by its multiple fins is carried out to investigate the effects of rigid and flexible fins. Dorsal, anal and caudal fins are included in the model. The morphology and kinematics of the flexible fins are obtained from a live fish experiment. The deformation of the caudal peduncle and the spanwise deformation of fins are ignored. Hydrodynamic performance of the fish with rigid and flexible fins are investigated, focusing on their differences in induced velocity, hydrodynamic force, surface pressure, vortex structure, power and efficiency.

The role of dorsal and anal fins during unsteady swimming is lastly analysed. Comparisons are made by simulating the pufferfish model with and without the dorsal and anal fins. A perturbation is given in the flow as a constant incoming velocity to study the performance of the models under unsteady flow conditions. The results are analysed from the following aspects: displacement, velocity, hydrodynamic force, power and efficiency. Interactions between the fish and fluid flow are analysed by visualising the vortices generated by the fish body as well as its multiple fins.

Table of Contents

Acknowledgements	I
Abstract	II
Table of Contents	IV
List of Figures	VIII
List of Tables	XIII
Chapter 1 Introduction	1
1.1 Background	1
1.1.1 Unmanned Underwater Vehicles	1
1.1.2 Fish swimming.....	3
1.1.3 Bio-inspired Devices.....	5
1.2 Objectives of the Thesis	11
1.3 An Outline of the Thesis	11
Chapter 2 Critical Review	14
2.1 Body motion.....	14
2.1.1 Methodology	14
2.1.2 Analysis of swimming	15
2.2 Single fin studies	24
2.3 Fish motion with multiple fins	31
2.4 Concluding remarks	38
Chapter 3 Numerical Methods	40
3.1 Introduction	40
3.2 Fluid Dynamics	41

3.2.1 Governing Equations and Numerical Methods	41
3.2.2 Mesh Motion Handling	44
3.3 Structure Modelling	46
3.3.1 Multi-Body Model Description.....	47
3.3.2 Deformation on each body/element	50
3.3.3 Mathematical Derivations	50
3.4 FSI Coupling Algorithm	57
3.5 Example of Pufferfish Model.....	61
3.5.1 MBD Model Establishment	61
3.5.2 FSI Response Calculation	62
3.5.3 Important performance parameters	63
3.6 Concluding remarks	66
Chapter 4 Four Kinds of Aquatic Biomimetic Problems	68
4.1 Actuated joints case studies	68
4.1.1 Discrete undulating fish	69
4.1.2 Continuous Anguilliform fish undulation	74
4.1.3 Fish Peduncle-Caudal Cupping Motion.....	78
4.2 Passive connection case study.....	85
4.3 Concluding remarks	92
Chapter 5 Self-Propelled Pufferfish with Multiple Fins.....	94
5.1 Problem Descriptions	94
5.1.1 Kinematics of a Pufferfish Body-Caudal-Dorsal-Anal Model	94
5.1.2 Computational domain and boundary conditions	100
5.1.3 Grid and time step size independence tests.....	102
5.2 Results and Discussions	104

5.2.1 Induced velocity U	106
5.2.2 Hydrodynamic force and surface pressure	107
5.2.3 Vortex structure.....	116
5.2.4 Power and Efficiency	122
5.3 Concluding remarks	123
Chapter 6 The Role of Dorsal and Anal Fins during Unsteady Fish Swimming	125
6.1 Motivation.....	125
6.2 Model Description.....	126
6.2.1 Model creation	126
6.2.2 Simulation cases.....	127
6.3 Results.....	127
6.3.1 Displacement and Velocity Development.....	127
6.3.2 Hydrodynamic Forces	130
6.3.3 Vorticity Structure.....	134
6.3.4 Power and Efficiency	137
6.4 Discussions.....	139
6.5 Concluding remarks	140
Chapter 7 Conclusions, Discussions and Future Work	142
7.1 Conclusions	142
7.1.1 Four Kinds of Aquatic Biomimetic Problems.....	142
7.1.2 Self-Propelled Pufferfish with Multiple Fins.....	142
7.1.3 The Role of Dorsal and Anal Fins during Unsteady Fish Swimming	143
7.2 Discussions.....	144
7.3 Recommendations for future work.....	146

References	149
Publications.....	156

List of Figures

Figure 1.1 Examples for typical Unmanned Underwater Vehicles.....	2
Figure 1.2 Resultant force and induced angular motion (Sfakiotakis et al., 1999).....	3
Figure 1.3 Sketches of fish morphology (Sfakiotakis et al., 1999).....	4
Figure 1.4 Classification of fish propulsion (Sfakiotakis et al., 1999)	6
Figure 1.5 Eel-like robots.....	7
Figure 1.6 G9 Fish model (Liu and Hu, 2010).....	8
Figure 1.7 RoboTuna and its internal structure.....	9
Figure 1.8 Example of Robotic fish for MPF mode (MAINONG et al., 2017).....	10
Figure 2.1 Effects of travelling index on the swimming performance of Carangiform fish (Cui et al., 2017).....	16
Figure 2.2 Comparisons of vorticity contours between 2D and 3D models (Kern and Koumoutsakos, 2006)	18
Figure 2.3 Velocity field for the three-identical-element model (a) without skin and (b) with skin, and trajectory for the three-different-element model (c) without skin and (d) with skin (Kajtar and Monaghan, 2012)	19
Figure 2.4 Variation of total drag, form drag and skin drag with Strouhal number at $Re=300$ and 4000 (Borazjani and Sotiropoulos, 2008).....	21
Figure 2.5 Comparisons of vortex structures between Carangiform and Anguilliform fish with $Re=9000$ at $t=5.0$ from vertical (left) and lateral (right) view, respectively. (Ogata et al., 2017)	22
Figure 2.6 The vortex structures of 2D and 3D elliptical foil with the asymmetry movement.....	23
Figure 2.7 Variations of propulsion efficiency η and caudal length R at $St=0.3, 0.4$ and 0.5 (Esfahani et al., 2013)	24

Figure 2.8 Average thrust and utilization wave power coefficients for the foil versus wave encounter frequency (Liu et al., 2018).....	26
Figure 2.9 Effects of varying the bending stiffness on the cruising speed and the swimming efficiency (Kim et al., 2016)	26
Figure 2.10 Variations of the hydrodynamic performance with the phase angle (Li and Su, 2016)	27
Figure 2.11 Numerical and experimental models (Zhou et al., 2017)	28
Figure 2.12 Three types of caudal shapes for a virtual swimmer	29
Figure 2.13 A geometrically and structurally simplified fin (Zhu and Shoele, 2008)	31
Figure 2.14 Example for live fish experiment with PIV method (Standen and Lauder, 2007)	32
Figure 2.15 Proposed 3D vortex structure around a swimming bluegill sunfish (Tytell, 2006)	33
Figure 2.16 Variation of force on the downstream fin with ten different distances and frequencies (Zhang et al., 2013).....	34
Figure 2.17 Overall propulsive efficiency versus overall thrust coefficient. The arrows mark the optimal cases in different number tandem foils (Yuan et al., 2015)	35
Figure 2.18 The prior body swims along the horizontal line, the follower adapt with the vortices relative to the leader (Guido et al., 2017)	36
Figure 2.19 Sketches of three models (Liu et al., 2017a)	37
Figure 3.1 Sketch of present tool for solving Fluid Structure Interaction (FSI) problems	40
Figure 3.2 Sketch of cell centroid	43
Figure 3.3 Examples of serial- and tree-like structure models	46
Figure 3.4 Sketch of Multi-Body tree-like and serial-like model. The tree-like model has one reference body (as coloured in grey) and more than one terminal bodies ($B_1, B_i, B_{i+m}, B_{i+m+n}$). The serial-like model has only one reference body and	

one terminal body. A tree-like model can be treated as being composed of several branches of serial-like models and all the branches share one reference body.....	49
Figure 3.5. Coordinate transformation: transformation matrix jT_i from local coordinate O_i of body B_i to the local coordinate O_j of body B_j	51
Figure 3.6 Flow chart of the hybrid algorithm (adapted from Porez et al. (2014a))..	58
Figure 3.7 Coordinate establishment of a self-propelled pufferfish	61
Figure 3.8 Selected fin rays for dorsal (shown as D), anal (A) and caudal (C) fins used to track motion in the experiment (Li et al., 2018)	66
Figure 4.1 Sketch of coordinate setting for the discrete fish body model.....	69
Figure 4.2 Computational domain of discrete fish body simulation.....	70
Figure 4.3 Velocity and Displacement comparisons between Eldredge (2008) and present study on the rotational motion, X and Y direction of the reference body	72
Figure 4.4 Vorticity structure comparisons with the values from -5 to 5 in 40 levels	73
Figure 4.5 Anguilliform fish model	74
Figure 4.6 Prescribed angular motion on hinges of anguilliform fish	76
Figure 4.7 Computational domain of anguilliform fish	76
Figure 4.8 Time history of forward and lateral velocity (Blue lines: results of Carling et al. (1998); red lines: present results)	77
Figure 4.9 Vorticity contour for 15 undulating periods (z vorticity with the values from -3 to 3 in 20 intervals)	77
Figure 4.10 Experimental model of fish peduncle-caudal (Hu et al., 2016).....	78
Figure 4.11 Fish peduncle-caudal CFD model and dimensions	79
Figure 4.12 Sketch of fish peduncle-caudal computational domain	80
Figure 4.13 Definition of θ for peduncle-caudal model.....	81

Figure 4.14 Thrust comparisons between CFD results and experiment results (Hu et al., 2016).....	83
Figure 4.15 Forces on peduncle and caudal fin in x direction at $St=0.3$	83
Figure 4.16 Vortex topology (vorticity magnitude with values from 0 to 15 in 16 levels) for peduncle-caudal model at $St=0.3$ in one period from XZ and XY view..	84
Figure 4.17 Sketch of the passive flapping wing model	85
Figure 4.18 Prescribed motions on reference body	86
Figure 4.19 Computational domain of the passive flapping wing model	89
Figure 4.20 Included angle comparison between Toomey and Eldredge (2008) and present study	89
Figure 4.21 Dimensionless force comparisons in x direction	90
Figure 4.22 Vortex development in one flapping cycle (z vorticity from -8 to 8 with 7 intervals).....	92
Figure 5.1 Live pufferfish in the experiment (Li et al., 2018) and CFD model and sketches for flexible dorsal, caudal and anal fins.....	95
Figure 5.2 Sketches for the definition of θ , leading, trailing fin ray and fin tip for (a) dorsal, (b) anal and (c) caudal fins. Red lines are X and Z axis in the local coordinate for each fin, and blue line stands for a random fin ray.....	96
Figure 5.3 Sketches for the envelopes of dorsal, anal and caudal fins in one motion period. Each envelope slice represents one motion moment. Red and blue lines in flexible condition (Case 4 left) stand for undulating from left to right and right to left respectively. Fins with rigid condition are presented at right and use Case 3 as an example. The motion period is split into 10 moments evenly for the rigid condition.....	100
Figure 5.4 Computational domain. The whole domain is split into inner and outer zone. Inner zone has finer mesh, comparing to outer zone, to better capture the flow structure of fluid field.....	101
Figure 5.5 Grid and time-step size independence tests	104

Figure 5.6 Velocity comparisons between rigid (Case 1 and 3) and flexible (Case 2 and 4) fins cases	105
Figure 5.7 Comparisons of Cycle-averaged total forces \bar{F}_T and total force F_T between rigid (Cases 1 and 3) and flexible (Cases 2 and 4) fins cases	109
Figure 5.8 Hydrodynamic propulsive force F_p , force on dorsal F_D , anal F_A , caudal F_C and body F_B for four cases.....	112
Figure 5.9 Distribution of pressure on fish surface relative to gauge pressure at outlet boundary.....	115
Figure 5.10 Vortex topology for $t/T=1.3-2.2$ with Iso-surface $Q=2$ for (a) Case 3 and (b) Case 4	117
Figure 5.11 Contours of slices for dorsal, anal and caudal fins for Cases 3 and 4 at $t/T=$ (1) 1.3, (2) 1.4, (3) 1.6, (4) 1.9, (5) 2.1, (6) 2.2.....	120
Figure 5.12 3D vortex topology of Iso-surface $Q=2$ at $t/T=5.2$ for four cases from (a) XZ view with included angle A , (b) XY view with included angle B and (c) zoomed-in XZ view.....	121
Figure 6.1 Sketches of Body, Dorsal, Anal, Caudal (BDAC, left) and Body, Caudal (BC, right) models.....	125
Figure 6.2 Displacement in X direction for Cases 2 and 4	128
Figure 6.3 Velocity comparisons for four cases	129
Figure 6.4 Force on the fish in 2nd and 50th period	132
Figure 6.5 Vortex structures for Case 1 and Case 2 during the 2 nd time period	135
Figure 6.6 Vortex structures for Case 3 and Case 4 during the 2 nd time period	136
Figure 6.7 Output power in the 50th period.....	138
Figure 6.8 Hydrodynamic force F_C on caudal fin and the induced velocity U of the self-propelled BC model in the still water in 50 th period.....	139

List of Tables

Table 2.1 Numerical models in past studies about undulating motions of fish body	17
Table 4.1 Categories of cases with actuated joints	68
Table 4.2 Motion parameters for peduncle-caudal model	82
Table 4.3 Parameters used in the passive flapping wing model	87
Table 5.1 Parameters in the kinematics equations	97
Table 5.2 Information for three different meshes	102
Table 5.3 Time-averaged velocity in x direction for quasi-steady stage	106
Table 5.4 Averaged Power and Efficiency	123
Table 5.5 Efficiency comparisons for different swimmers	123
Table 6.1 Case Number and Condition	126
Table 6.2 Averaged power and efficiency	138

Chapter 1 Introduction

1.1 Background

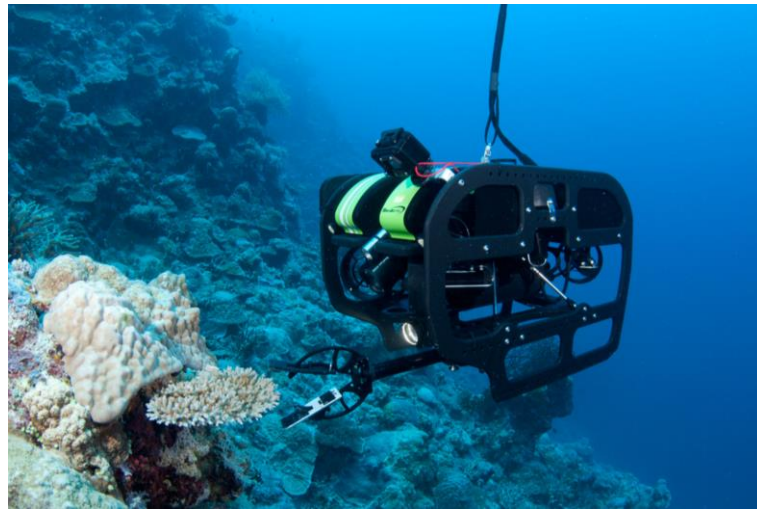
1.1.1 Unmanned Underwater Vehicles

The world's demand for energy has soared over the past few decades. Thus, scientists have been seeking new ways to satisfy the ever-increasing need for energy consumption, such as exploring and making use of offshore resources. The environment undersea is more complicated than on land and is full of uncertain factors. It is hence vital to develop underwater vehicles to replace humans to work in deep water conditions. In the past decades, Unmanned Underwater Vehicles (UUV) have been invented and applied to the exploration of undersea resources. Similar to drones, this kind of vehicle is able to work underwater without the need of any human operating on board. Remotely Operated Vehicle (ROV) & Autonomous Underwater Vehicle (AUV) are two typical kinds of such devices.

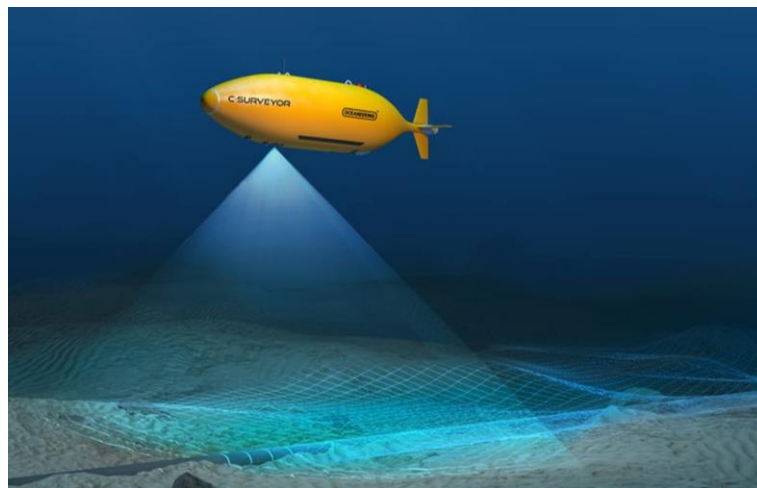
One example of ROV is shown in Figure 1.1(a). It is tethered to a remote operator via cables, which are used to communicate with the ROV as well as to supply power. Due to the dark working environment in deep water, most ROVs are equipped with lights and video cameras for illumination and recording. To perform intricate tasks such as taking samples, manipulators are also included in the ROVs and they react only after receiving specific commands from its remote operator. As ROVs are tethered by cables, their operation range is limited.

Different from ROVs, no cable is connected to an AUV during cruising and its locomotion is pre-programmed. This enables it to move more flexibly than ROVs. A typical AUV can be referred to in Figure 1.1(b). However, communicating with operators becomes challenging for AUVs without cables, and the power source should be carried by themselves (Blidberg, 2001). The environment in deep sea is complicated and always changing. If one AUV loses communications or runs out of power during

a mission, a heavy loss will be suffered. With the increasing requirement for endurance hours, battery performance becomes an urgent issue. Most recent demand is to allow AUVs to charge themselves by travelling to a specific location undersea, such as a base station built below offshore wind turbines. Under this circumstance, the abilities of cruising and manoeuvring for AUVs should be improved in an intelligent way. The so-called bio-inspired devices, which apply the mechanisms learnt from aquatic animals to man-made vehicles, could be one way to solve this problem.



(a) ROV (source: CATLIN SEAVIEW SURVEY and the Deep Reef Science Team)



(b) AUV (source: OCEANEERING)

Figure 1.1 Examples for typical Unmanned Underwater Vehicles

1.1.2 Fish swimming

Aquatic animals like fish have evolved excellent propulsive and manoeuvring abilities to adapt themselves to the underwater environment. Swimming is a process that involves momentum transfer between a fish and its surrounding fluid. This mechanism can be achieved via force generation.

Forces acting on a swimming fish are illustrated as Figure 1.2. The physical forces on animals swimming in water are quite different from those creeping on the land or flying in the sky. In the horizontal direction, there are thrust and resistance forces. The latter one includes friction drag and pressure drag. For fish swimming in the water, the friction drag is insignificant while the pressure drag is relatively large. This is in contrast to those animals living on the land. As the density of water is larger than air, pressure drag from the air can be negligible. With a large friction drag, some unsteady locomotion cannot be done by terrestrial animals. For example, a snake has almost the same form of motions as an eel, i.e., bending the whole body into a wave shape and propagating the wave along the body to move forward or backward. However, crawling on the ground, snake cannot move rapidly. Some animals have evolved limbs for walking. This can reduce the friction force from the ground to better adapt to the continental life.

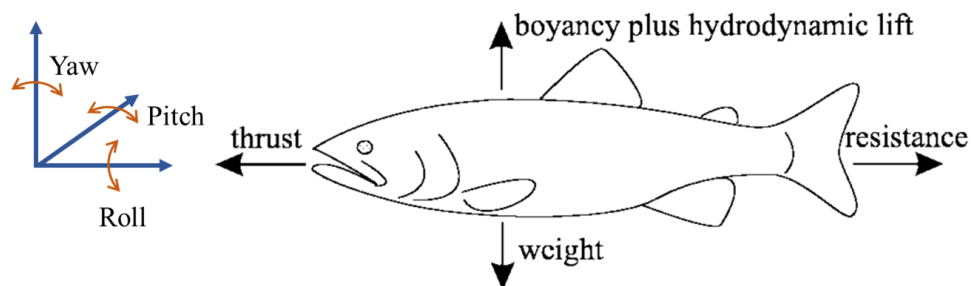


Figure 1.2 Resultant force and induced angular motion (Sfakiotakis et al., 1999)

Buoyancy, lift, and weight forces exist in the vertical direction. Water can offer buoyancy to those immersed organisms and it can always balance the weight. To some

large fish, such as whales and tunas, substantial lift is also generated by the tail to compensate the weight. There is no need for fish to grow strong internal structure to carry their weight. Thus, gravity seems not to be a big issue for creatures living in water. However, it matters a lot to flying birds and insects. Those animals that abandon the aquatic environment must grow strong bones to support their locomotion. As gravity is much larger than the buoyancy that air offers, the lift force must be greater than the weight so that birds and insects could get off the ground. By enlarging the surface area, flying animals could obtain large enough lift force.

For cruising swimming, the forces are balanced, i.e., weight is equal to the sum of buoyancy and lift forces in the vertical direction, while thrust is equal to resistance in the horizontal direction. However, the majority of motion status for fish in their living environment is unsteady. For example, fish need to start rapidly to escape from predators, and constantly accelerate in a short time to prey for food. These kinds of locomotion break the balance of forces that act on the fish, which would lead to angular motions, such as yaw, roll and pitch as shown in Figure 1.2.

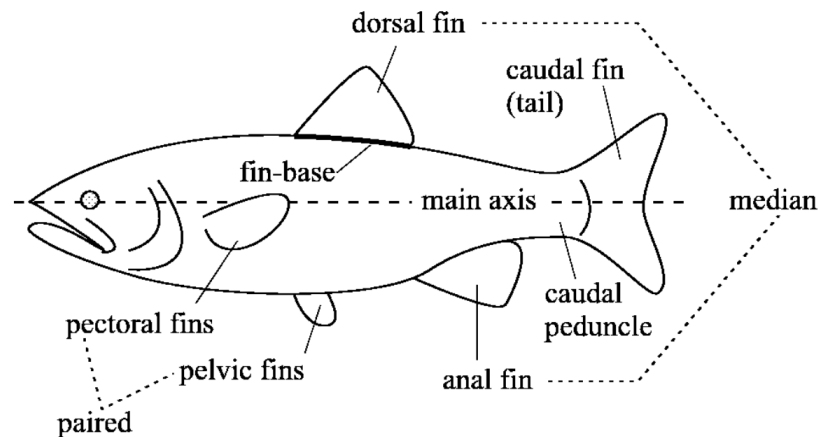


Figure 1.3 Sketches of fish morphology (Sfakiotakis et al., 1999)

Fish fins work together with its body to produce hydrodynamic forces. Meanwhile, they could also control the whole fish to manoeuvre, rotate or remain steady. Figure 1.3 identifies the different fins and other features of fish. Caudal fin is the most

important propeller in fish swimming and has been investigated intensively in previous studies. Apart from the oscillating motion with caudal peduncle, it also has its individual undulating motion. Moreover, its flexibility could also affect the hydrodynamic performance of fish swimming.

Some fins, such as pectoral and pelvic fins, are paired and symmetry. These kinds of paired fins are normally used for controlling swimming directions and manoeuvring. Median fins include dorsal and anal fins. The motions of these two fins are synchronistical to avoid rolling motion (Standen and Lauder, 2005). To some species, pectoral, dorsal and anal fins can also generate propulsive force. Although not all functions of these fins are the same, normally they work together to enable various locomotion of a fish.

1.1.3 Bio-inspired Devices

In the past decades, the so-called bio-inspired device has become a new hot topic for scientific research. Their principles, i.e., the *bio-inspired locomotion*, could be learnt from various creatures in nature, such as fish, birds and insects, and applied to newly invented equipment. It is expected that these devices can have better performance than traditional ones. It is believed that they can work with less power consumption, produce lower noise level, and move more flexibly (Habib and Davim, 2013; Salazar et al., 2018). As a result, they have been applied to multiple research areas and industrial activities, such as biomedical engineering, ocean engineering and aerospace engineering.

Before being applied in the engineering industry, a series of comprehensive and scientific investigations about these creatures has been carried out during the past few decades. Various man-made robotic devices have thus been designed. With a microscopic approach, it is challenging to understand the mechanisms, such as the mechanical function of fish muscle under different swimming conditions, how the nerves control fish behaviours in diverse environments. A prosperous future of man-

made robots could be achieved by applying these mechanisms. From the point of macroscopic view, the bio-inspired robots could employ the biological locomotion and morphology directly. This is also what the present research focuses on, and these kinds of robots will be introduced briefly in the rest of this section.

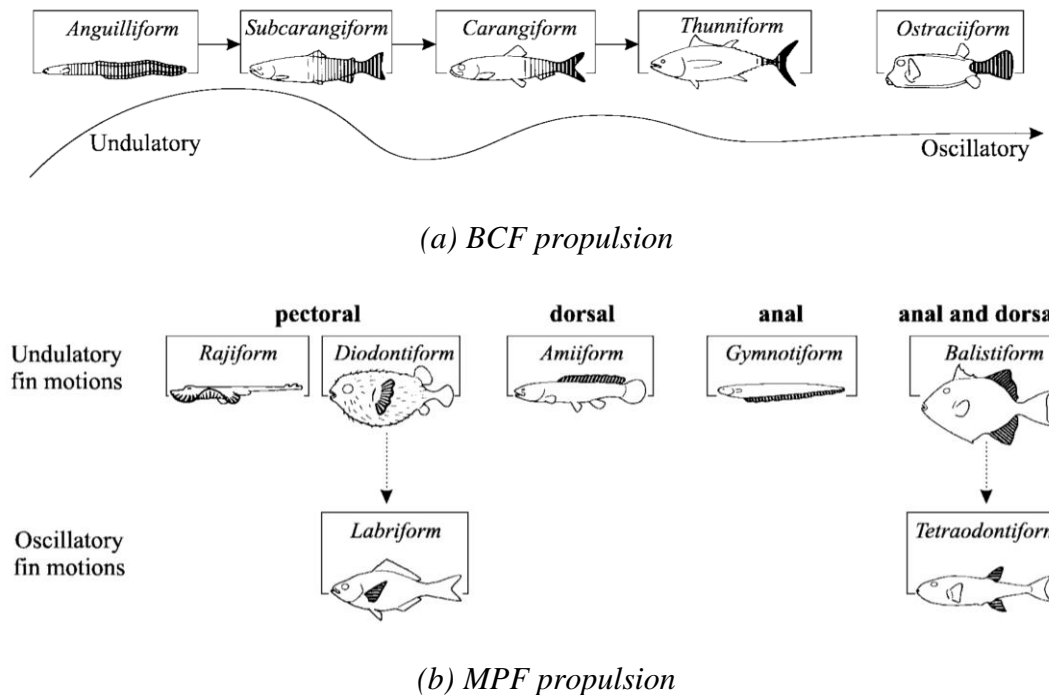
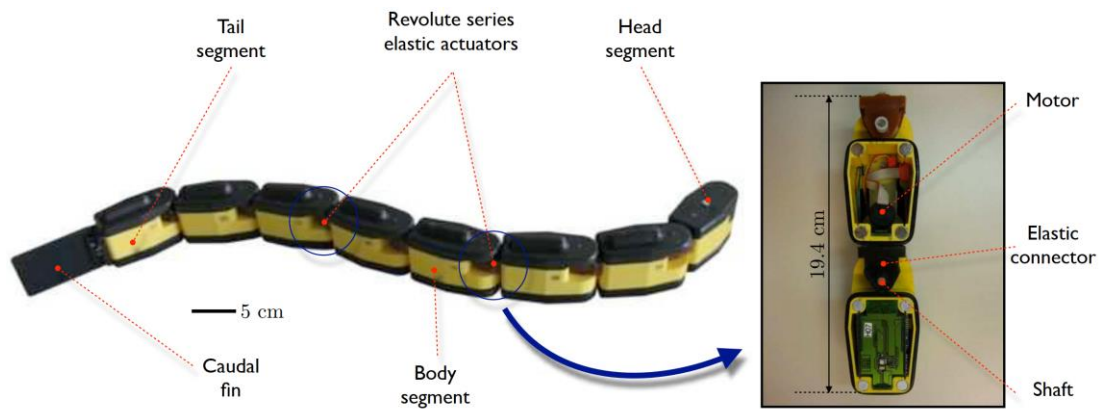


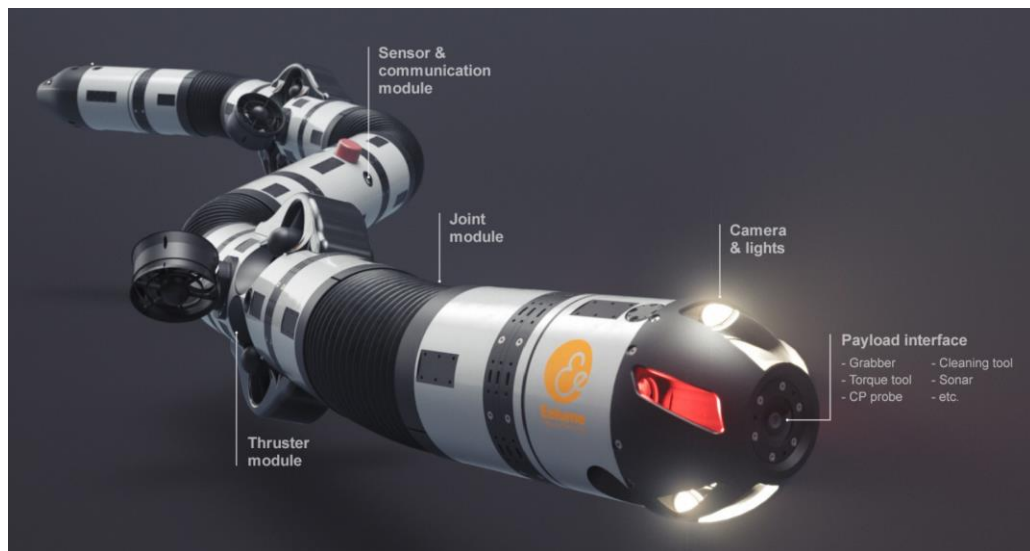
Figure 1.4 Classification of fish propulsion (Sfakiotakis et al., 1999)

Due to the diversity of fish propulsion method, one common categorisation was given by Lindsey (1978) as the BCF mode (Body and/or Caudal Fin) and MPF mode (Median and/or Paired Fin). Figure 1.4 summarises the classification of fish swimming and the shaded part stands for the part of the fish that contributes most to thrust generation. In general, it is difficult to distinguish between the BCF and MPF modes of a fish, because fish always employ more than one method for locomotion. The oscillatory and undulatory motion can be roughly distinguished by the number of waves that are propagated on the shaded part. If there is more than one complete wave on the shade part, the motion can be considered as pure undulatory. With the decrease of wave number, the motion mode of a fish changes from undulatory to oscillatory.

Relevant research has mainly paid attention to five parts of a fish, i.e., the fish body, caudal fin including caudal peduncle, pectoral, dorsal and anal fin.



(a) *AmphiBot III robot (Porez et al., 2014b)*

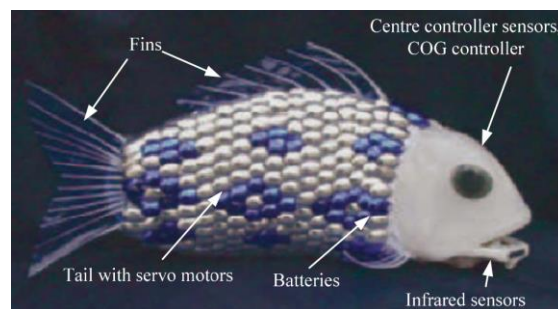


(b) *Eelume (source: EELUME)*

Figure 1.5 Eel-like robots

For the BCF mode, fish uses its body, caudal peduncle and caudal fin for propulsion. The streamlined-shape body enables high propulsion efficiency of fish swimming. The motion of typical Anguilliform fish, such as eel, is purely undulatory. Its shape is elongated, and the caudal fin is very small. Learning from this, the frame of some eel-like robots can be made of a series of modular units and two successive units are

connected by joints, as illustrated in Figure 1.5. For example, apart from the head and tail segments, the other body parts of the AmphiBot III robot in Figure 1.5(a) are comprised of identical segments so that the length of the robot could be controlled to meet different demands. Another advantage of this modular formation is that if modifications are required somewhere on the robot, changes do not need to be applied on the whole model. One representative bio-inspired device is a commercial robot called *Eelume*, as shown in Figure 1.5(b). It can be used for operation and maintenance of underwater equipment. The configurations of this robot are diverse. The propulsion mechanism can be either self-propelled or with thrusters as long as the corresponding module is installed, so that it could move even in the server environment undersea, such as in a strong current condition. Its slender body enables flexible movement in deep water. Moreover, by adding some specific manipulators, it can work undersea to replace human operation, such as examining pipelines in some dangerous and restricted areas on the seabed.



(a) Structure sketch of G9 Fish model



(b) Cruising motion



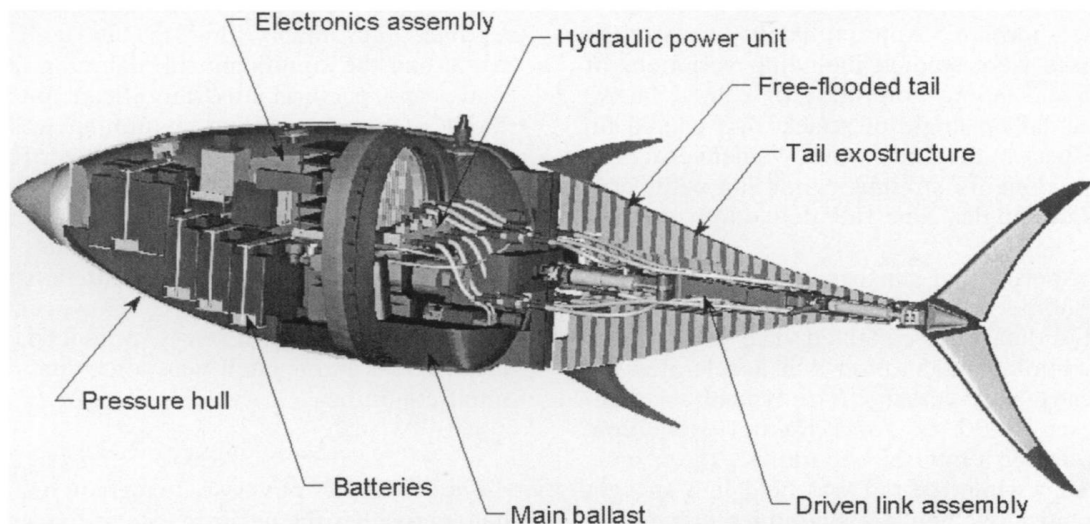
(c) C-turning swimming

Figure 1.6 G9 Fish model (Liu and Hu, 2010)

With the change of fish motion from undulating to oscillating modes, two main differences could be observed. The first one is that the occupied region for motion becomes smaller and mainly locates at the posterior part of the fish. For example, Carangiform fish uses its latter half body for propulsion. A staple design of fully equipped robotic fish is shown in Figure 1.6(a). Its body is made of three actuated motors and combined with sensors. Cooperating with the passive deformed fins, the robot could perform cruising and C-turning motions as shown in Figure 1.6(b) and (c).



(a) *RoboTuna* (source: *THESWELLESLEYREPORT*)



(b) *Internal structure of RoboTuna* (Anderson and Chhabra, 2002)

Figure 1.7 RoboTuna and its internal structure

Another obvious difference is that the morphology of caudal fin changes a lot. Typical Thunniform fish, such as tuna and shark, has a lunate tail, which is connected to the main body with a narrow caudal peduncle. Comparing to Anguilliform fish, its caudal fin is more rigid but is able to generate most thrust. Figure 1.7 presents an early robotic fish called RoboTuna. It followed the morphology of the yellowfin tuna. As a Thunniform fish only oscillates its caudal peduncle and fin, posterior part of this robot is made of articulated components with water-proof covers. The main body of this robot is a rigid hull and contains necessary equipment. It was used to study the kinematics and movements of these kinds of robotics and researchers found that the steady swimming speed of this fish could reach 1.2m/s.

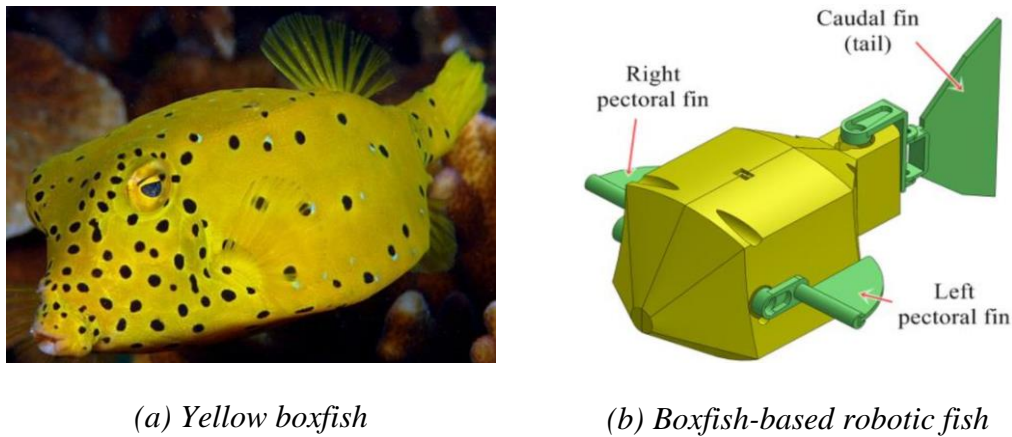


Figure 1.8 Example of Robotic fish for MPF mode (MAINONG et al., 2017)

The paired and median fins could also contribute to the swimming of fish. These fins could be used for either propulsion or manoeuvring. Boxfish is a classic swimmer that employs multiple fins for swimming. Its carapace is rigid and non-streamlined, as shown in Figure 1.8(a). Even though its dorsal, caudal and anal fins can be used for propulsion, its forward swimming seems more cumbersome and the velocity in the forward direction is rather small. However, it has excellent manoeuvring performance. With the cooperation of a pair of pectoral fins and the caudal peduncle, it could perform 180° turn with near zero turn radius. This sheds light on the invention of innovative underwater vehicles. A corresponding bio-inspired robotic fish inspired by

boxfish is given in Figure 1.8(b). By varying the shape of pectoral fins, the hydrodynamic performance of this type robots could be tested and furthermore applied in the industry.

1.2 Objectives of the Thesis

The main objectives of this thesis are to gain a better understanding of the underlying physics and sophisticated interactions between the locomotion of aquatic animals and their surrounding fluid field, especially the self-propelled motion of real fish. In particular, the following two problems will be investigated: the influences of fish fin flexibility on self-propulsion and the role of dorsal and anal fins during unsteady swimming. These are achieved by taking the following steps:

1. Develop a coupled fluid-structure analysis tool to solve the complicated dynamics of different fish swimming, including the motions of fish body and various fins.
2. Validate the numerical tool by studying several classical fish swimming problems and comparing results with published data.
3. Analyse the flexibility effects of fish fins on the self-propulsive motion of a pufferfish by comparing the performance of the fish with either rigid or flexible fins.
4. Investigate the role of dorsal and anal fins during unsteady swimming of the pufferfish by setting up two models with/without the two fins subject to a constant current.

1.3 An Outline of the Thesis

The structure of this thesis is outlined as follows.

Chapter 1 introduces the background of this study by providing an overview of typical unmanned underwater vehicles and pointing out the shortcomings in the present designs. After giving a brief introduction to fish swimming, several different types of bio-inspired devices are listed.

To give a comprehensive review on the fish swimming problem, three aspects of the classical problems from previous investigations in the past decades with various methods will be given in Chapter 2.

In Chapter 3, the coupled CFD-MBD tool developed in this project for numerical analysis of fish swimming is introduced. Detailed description of the various numerical methods and techniques adopted in the present tool is presented, including CFD modelling of fluid flow, CFD mesh motion handling, the utilization of parallel simulation, calculation of structural response with MBD theory and the coupling between fluid solver and structure solver. Meanwhile, detailed descriptions on a typical fish model established based on the MBD approach is presented.

Due to the complexity of the problems investigated, Chapter 4 presents a series of case studies to validate the various usages of the developed coupled MBD-CFD tool by comparing results from the present code with published experimental and numerical data. These studies include basic fish undulating motion with both discrete and continuous model, a simplified peduncle-caudal motion model, and a theoretical passive connection case.

The following two chapters focus on the application of the numerical tool to real fish problems with accelerating and quasi-steady swimming. A pufferfish is selected to study its self-propelled motion driven by its caudal, dorsal and anal fins. Chapter 5 analyses the impacts of the deformation of multiple fins on self-propelled fish swimming. A corresponding rigid condition is thus also simulated as a comparison, where the motion of the whole fin surface is uniform.

Chapter 6 then further investigates the role of dorsal and anal fins during unsteady fish swimming. Two fish models are established, including one with all three fins and the other with only the caudal fin. Both models are subjected to an unsteady flow condition, i.e., a constant incoming current is specified. Results are also compared with those associated with the still water condition to assess the hydrodynamic performance of the two models under different environmental conditions.

Finally, conclusions from this project are drawn in Chapter 7, followed by suggestions made for future work.

Chapter 2 Critical Review

Over the past few years, along with the growing interest in the exploration of ocean resources, lots of research concerning the motion of aquatic animals has been carried out numerically in various aspects. Traditionally, studies on fish swimming can be classified into three major groups with increasing complexity: (a) fish body motion without considering the influence of different fins; (b) interactions between multiple fins without considering the fish body; and (c) complicated motions combining fish body and multiple fins. In this chapter, these three parts will be reviewed separately.

2.1 Body motion

Various investigations of fish body motion have been carried out in the past few decades. They are well summarised in several comprehensive review papers (Webb, 1984, 1994; Sfakiotakis et al., 1999; Borazjani, 2015; Lauder, 2015; Liu et al., 2017b). Fish swimming is a typical fluid-structure interaction problem: on one hand, muscle constrains cause body deformation, and thus pushes the coherent flow downstream, which leads to the momentum transfer from the swimmer to the flow; on the other hand, the surrounding fluid can also impart forces on the fish, which would push it to deform or swim (Bhalla et al., 2013).

2.1.1 Methodology

Some classical methods were used to solve the motion of Anguilliform swimming at the very early stage. Lighthill's Elongated Body Theory (EBT) (Lighthill, 1960; Lighthill, 1970, 1971) is one of the early analytical approaches to identify the physical mechanism behind undulating motions. It simplifies the fish body as a curve/slender-body and assumes a completely inertial flow condition. This results in elegant mathematical expressions which can be solved without computers. Therefore, such simplifying assumptions in analytical models enable us to expediently analyse the essence of swimming, albeit at a considerable sacrifice of applicable range and

accuracy. By assuming that a swimming fish is in a quasi-steady state, this analytical model reduces the complexity of live fish swimming during the modelling process. This method concentrates on the primary fluid dynamic characteristics while neglecting secondary effects. Particularly, as the unsteady mechanism is found to cause considerable extra hydrodynamic forces, it is beyond the capability of any analytical model, such as Li et al. (2016).

Apart from analytical models, Computational Fluid Dynamics (CFD) methods can predict the fluid flow around fish with good accuracy and have thus been increasingly used for fish swimming problems over the past few years. Past studies adopting CFD methods can be generally divided into two categories, i.e., non-boundary-conforming and boundary-conforming methods (Borazjani, 2015).

Immersed Boundary Method (IBM) is one of the typical non-boundary-conforming methods. Since IBM employs fixed grid, no remeshing is needed, which ensures that grid quality is maintained. However, additional work is required, such as identifying the grid nodes adjacent to the moving boundaries and transferring the forcing effects onto those nodes. Meanwhile, most of the simulations that currently use IBM are 2D problems and classic IBM-based approaches cannot solve problems with high Reynolds number. On the contrary, boundary-conforming methods pay close attention to moving boundaries, which may cause large deformation of grids. Some dynamic mesh functions are hence used to maintain the quality of mesh and the accuracy of simulations, such as remeshing and smoothing functions in ANSYS Fluent. Although computational time is sacrificed somehow due to mesh motion, this method can be used to solve problems in 3D and with high Reynolds number.

2.1.2 Analysis of swimming

The locomotion of Anguilliform fish is a representative type of undulating motion of fish body that can be found in various previous studies. Most studies prescribed the kinematics of the midline of their models (Carling et al., 1998; Borazjani and

Sotiropoulos, 2009; van Rees et al., 2013). The motion amplitude increases from head to tail (Vorus and Taravella, 2011) and thrust is generated continuously along the body with increasing magnitude toward the tail (Chen et al., 2011). Head never produces thrust, but is responsible for the majority of the drag force (Reid et al., 2012).

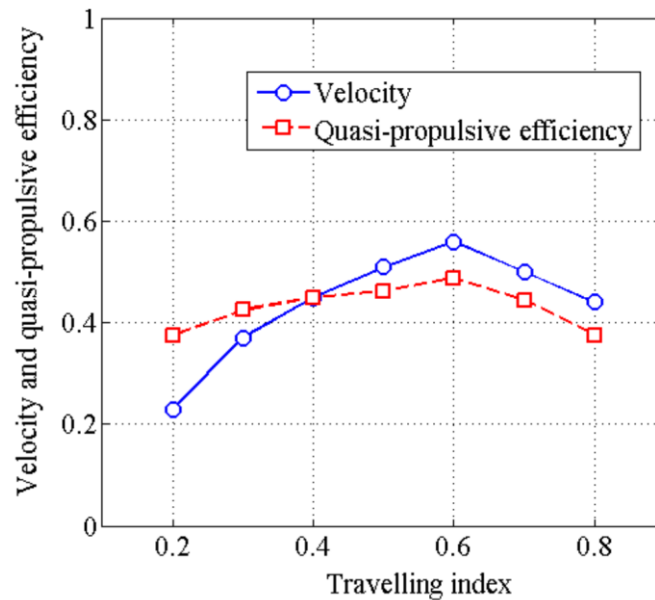


Figure 2.1 Effects of travelling index on the swimming performance of Carangiform fish (Cui et al., 2017)

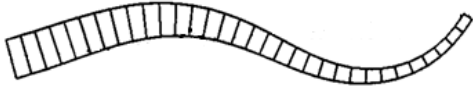
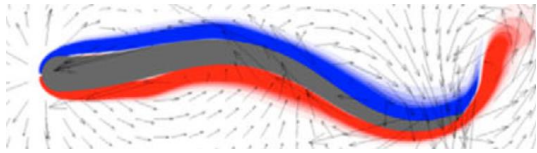

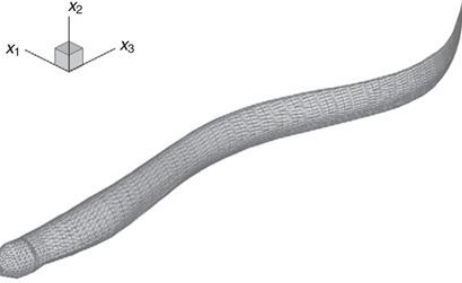
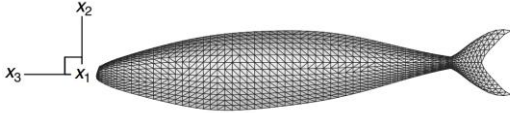
In some studies, the undulatory motion of fish body could be measured by the number of wavelength and the travelling index. Nangia et al. (2017) found that an undulating model could gain maximum propulsive force and swimming speed by employing an optimal specific wavelength. Meanwhile, the wavelength of creatures in nature is almost close to the optimal specific wavelength. The travelling index was defined by the ratio between the travelling part and standing part of the midline motions (Feeny, 2008; Feeny and Feeny, 2013).

Cui et al. (2017) investigated a self-propelled fish of Carangiform mode. As depicted in Figure 2.1, results showed that when the travelling index is around 0.6, the swimmer could gain a fast and efficient swimming motion. The forward speed is related to the

travelling index and tail-beat frequency as well. When the beating frequency and amplitude of the tail increase, the corresponding swimming efficiency also increases.

Previous CFD studies with boundary-conforming methods on Anguilliform swimming have mostly employed 2D models, where fish body can be modelled either as a continuous body or a multi-body system with several discrete elements connected via joints as illustrated in Table 2.1. Typical work with continuous fish models includes Carling et al. (1998), Kern and Koumoutsakos (2006), Borazjani and Sotiropoulos (2009). Discrete models can be found from as Kanso et al. (2005) and Eldredge (2007).

Table 2.1 Numerical models in past studies about undulating motions of fish body

Dimension	No.	Model sketches	References
2D	(a)		Carling et al. (1998)
	(b)		Kern and Koumoutsakos (2006)
	(c)		Kanso et al. (2005)
3D	(d)		Borazjani and Sotiropoulos (2009)
	(e)		Borazjani and Sotiropoulos (2008)

The shape of a continuous model could be various. Carling et al. (1998) set up a 2D self-propelled Anguilliform model as shown in Table 2.1(a). Its motion was firstly induced by the interaction between fluid and the prescribed deformation of shape rather than imposing a forward velocity on the fish as in previous studies and was solved with their in-house CFD code. Results showed that the induced forward velocity had an oscillatory rather than linear characteristic. However, due to the limitations of 2D studies, this study could only represent the behaviour of a swimming sheet extending in directions perpendicular to the plane of swimming.

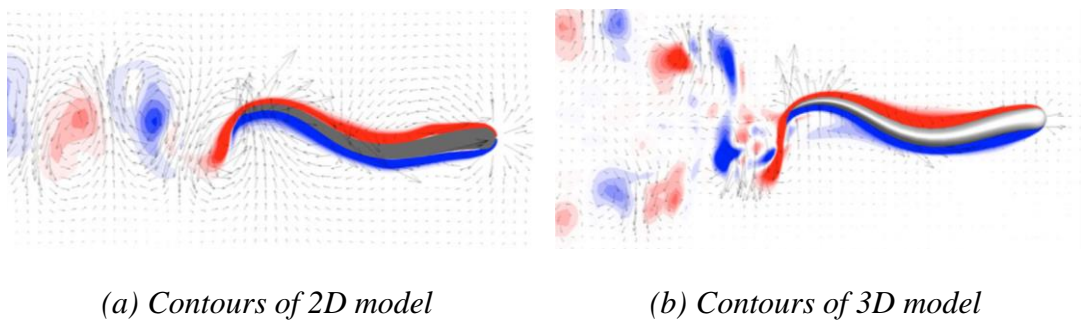


Figure 2.2 Comparisons of vorticity contours between 2D and 3D models (Kern and Koumoutsakos, 2006)

Kern and Koumoutsakos (2006) studied a self-propelled anguilliform swimmer with the commercial CFD software package STAR-CD. The geometry of the model was updated without sharp corners and the lateral displacement was prescribed following the work of Carling et al. (1998). Both 2D and 3D simulations were carried out, with the 2D model shown in Table 2.1(b). Results of 3D condition were compared with experimental and 2D studies. Modelling results indicated that, propulsion thrust was generated by different portions of fish body motion depending on whether swimming is steady or burst. Both velocity and wake patterns for 3D simulations matched well with the experimental study. However, significant differences could be found in the wake between 2D and 3D, as illustrated in Figure 2.2. A two-dimensional fish generated a single row wake, whereas 3D fish created double rows wake. Moreover, although the development of velocity had the same tendency, the velocity in 2D study

was larger than its 3D counterpart. Thus, the phenomenon of fish swimming could not be completely revealed by simplifying the fish as a 2D model.

3D simulations about tethered Anguilliform swimming were carried out by Borazjani and Sotiropoulos (2009). Their model is shown in Table 2.1(d). One improvement in this study was that the kinematics and geometry of fish were obtained from experimental observations. Thus, the simulations were more realistic than previous studies. Similar to the conclusions about the wake structures of Kern and Koumoutsakos (2006), Borazjani and Sotiropoulos (2009) also found two rows in the wake that were generated by the 3D eel model. Moreover, further analysis showed that the wake structure depended on the Strouhal number (St). A single-row pattern occurred at low St , while at higher St the double-row structure could be observed.

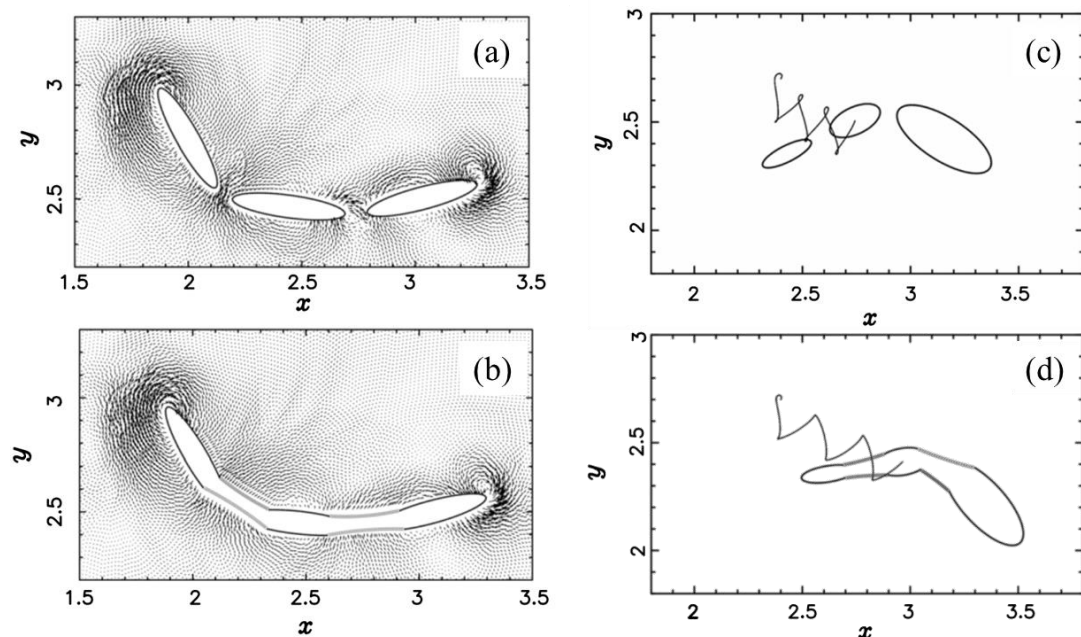


Figure 2.3 Velocity field for the three-identical-element model (a) without skin and (b) with skin, and trajectory for the three-different-element model (c) without skin and (d) with skin (Kajtar and Monaghan, 2012)

The undulating motion of fish swimming could also be studied with discrete models. By modelling a fish as several articulated solid bodies, Kanso et al. (2005) firstly

analysed its locomotion in ideal fluid as shown in Table 2.1(c). Furthermore, a series of investigations about a simplified undulation motion of an anguilliform free-swimming fish was studied (Eldredge, 2006; Eldredge, 2007; Eldredge, 2008). The model was two-dimensional and made of three identical rigid elements. A Viscous Vortex Particle Method (VVPM) was used to examine such system propulsion performance. With a particle method called Smoothed Particle Hydrodynamics (SPH), Kajtar and Monaghan (2012) also investigated a discrete fish model. Two types of discrete models were simulated, i.e., three identical rigid elements and three rigid elements with different size, and the mass for both models remained the same. The influence of skin on the hydrodynamic performance was also tested. The rotational motions on the hinges that connected two successive elements were also prescribed. Results illustrated that if proper motions were prescribed on the hinges, the induced locomotion of the model with identical discrete elements could behave like the swimming mode of an Anguilliform fish.

Unlike the Anguilliform mode, studies of undulating motion about the Carangiform fish focused on their last third portion of the body along with the caudal fin. A typical Carangiform model is shown in Table 2.1(e). Kajtar and Monaghan (2012) studied the characteristic of Carangiform swimming with a model comprising of three elements. The velocity field and trajectory were compared for the model with/without skin as shown in Figure 2.3. Velocity field for the model with/without skin was similar and their trajectory was zig-zag. It was noted that the presence of skin could improve the efficiency of motion for both types of models. Meanwhile, the fish with skin could swim faster for a given distance while using less power and energy compared with the model without skin. This reveals that although slight differences exist, the fish swimming problem could be solved by splitting a continuous model into discrete elements.

Besides the studies about self-propelled motion, tethered swimming offers another aspect to investigate the hydrodynamic mechanism. With the commercial software ANSYS Fluent, Adkins and Yan (2006) found that high pressure zones are obvious at

the rear of the body, especially the caudal fin, which indicated that strong vortex and turbulence effects happened. Some simplifications were made in the study such as a rigid tail and no appendages except a caudal fin.

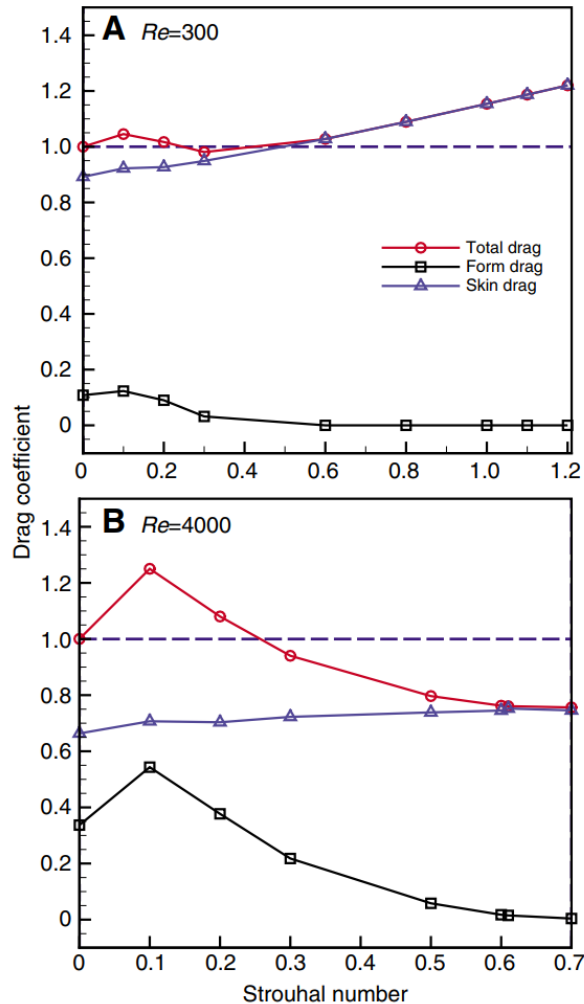


Figure 2.4 Variation of total drag, form drag and skin drag with Strouhal number at $Re=300$ and 4000 (Borazjani and Sotiropoulos, 2008)

Borazjani and Sotiropoulos (2008) numerically investigated the influences of Reynolds number and Strouhal number defined by tail beat frequency on a flexible mackerel-like model with prescribed kinematics from experimental observations. Results showed that a more flexible body required larger swimming power than the rigid one at the same swimming speed. With a small Reynolds number $Re = 300$, the

drag force of flexible model is larger than the rigid one and it would be significantly reduced when Re becomes 4000, as presented in Figure 2.4. They concluded that with a sufficient high Re the form drag dominated the drag force of the fish.

Borazjani and Sotiropoulos (2010) further studied the influences of form and kinematics on the hydrodynamic performance of undulating swimming. Both Anguilliform and Carangiform swimmers were selected. Results showed that the swimmer with the Anguilliform kinematics could reach a higher velocity with better efficiency in both viscous and transitional regimes. Carangiform kinematics achieves a higher swimming speed than its Anguilliform counterpart and becomes more efficient when the flow is in the inertial regime.

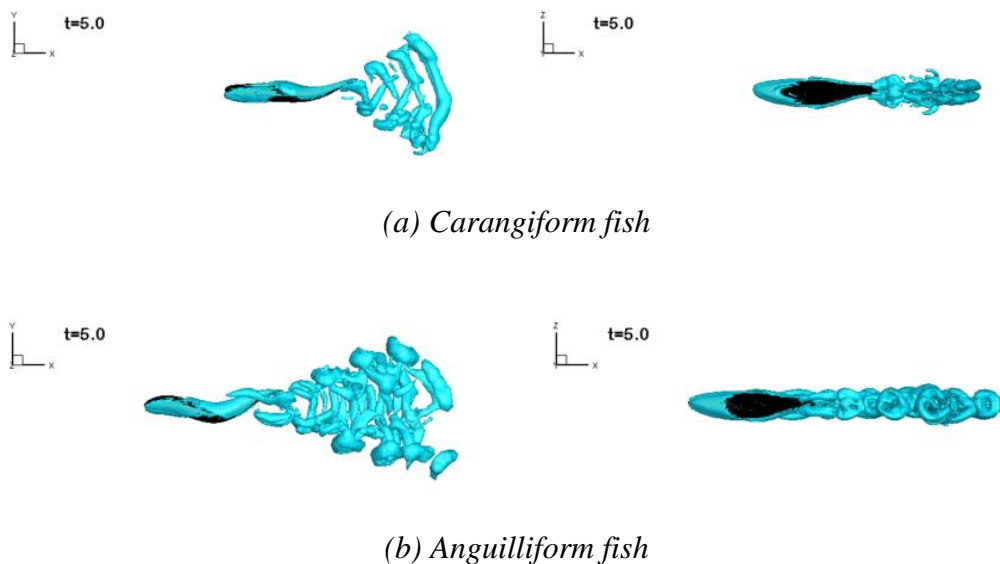
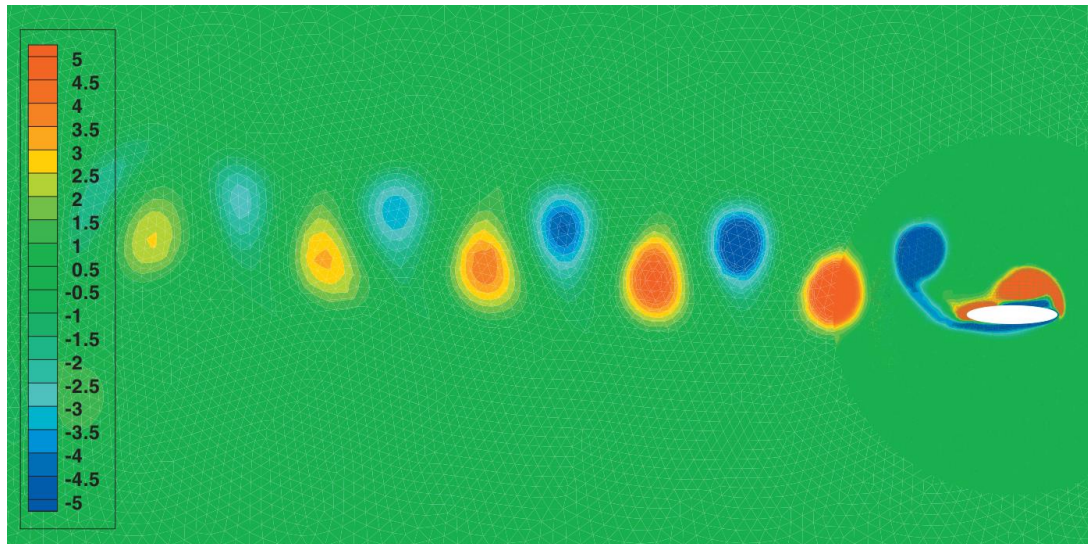


Figure 2.5 Comparisons of vortex structures between Carangiform and Anguilliform fish with $Re=9000$ at $t=5.0$ from vertical (left) and lateral (right) view, respectively.

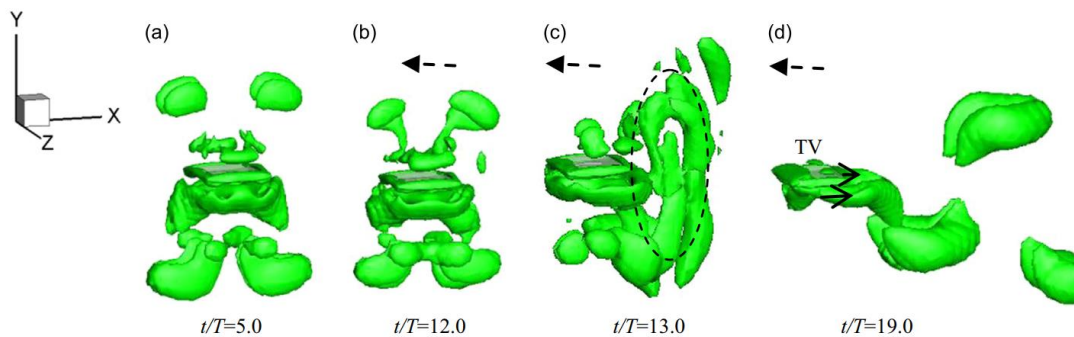
(Ogata et al., 2017)

Ogata et al. (2017) also discussed the differences between the Anguilliform and Carangiform swimming. These two kinds of motions were prescribed on the same three-dimensional model. The accelerating stage is investigated. It was found that the

model with Anguilliform motion could accelerate more rapidly due to the strong transverse vortex in the wake generated by the fish and the large variation of the body pressure, as presented in Figure 2.5.



(a) Reversed von Kármán vortex street generated by the induced asymmetry movement of a 2D elliptical foil (Zhang et al., 2009)



(b) Vortex topology generated by the 3D foil (Hu and Xiao, 2014)

Figure 2.6 The vortex structures of 2D and 3D elliptical foil with the asymmetry movement

Maertens et al. (2017) studied the optimal undulating motion with a specific Reynolds number $Re = 5000$. By optimizing the motions of measured displacement for

Carangiform fish, its efficiency could increase from 35% to 50% and from 22% to 34% for 2D and 3D simulations, respectively.

2.2 Single fin studies

Some experimental studies investigated the performance of a single fin. Caudal fin is a typical model as it produces the most propulsive force for fish. For example, Coral et al. (2015) designed a bio-inspired caudal fin composed of several Shape Memory Alloy (SMA) wires and cellulose acetate film to mimic the behaviour of muscles. By applying different electrical current on the SMA wires, the evolution of maximum contraction on the caudal fin was successfully simulated. Hu et al. (2016) observed the cupping motion of the caudal fin on a live yellow perch and extracted the biological kinematics. A robotic caudal fin model was then established. Its hydrodynamic performance was tested by specifying the obtained kinematics. Results showed that when the cupping motion was imposed on the caudal fin, greater vortices could be generated.

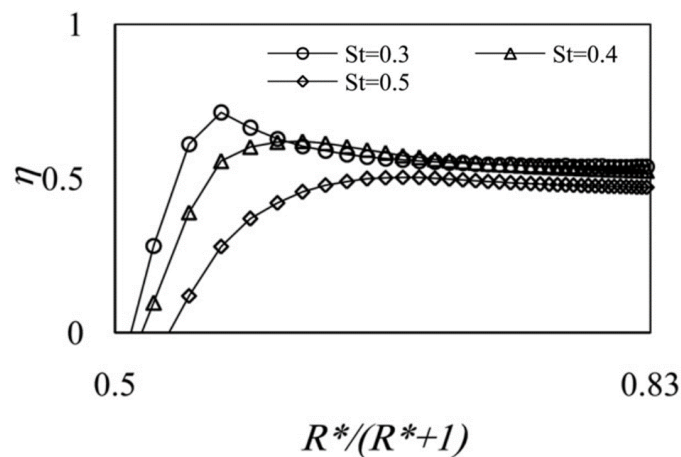


Figure 2.7 Variations of propulsion efficiency η and caudal length R at $St=0.3, 0.4$ and 0.5 (Esfahani et al., 2013)

Some numerical investigations simplified the problem of fish swimming and only concentrated on the performance of a single fish fin. As an initially simplified step, the

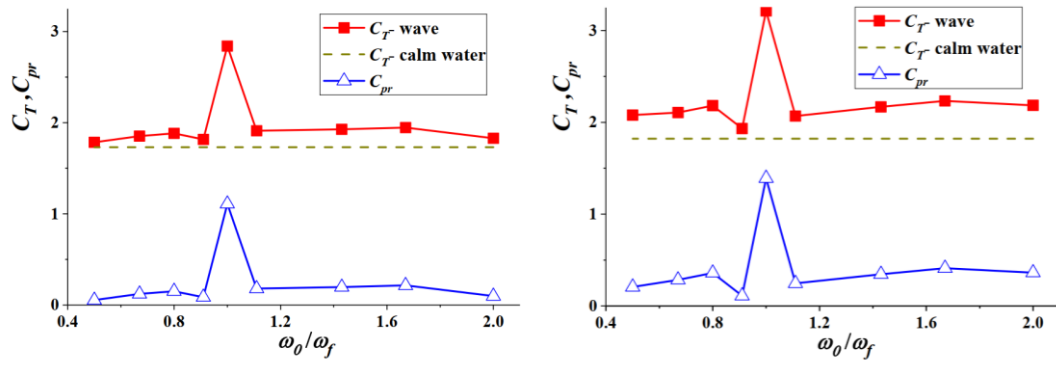
morphology of fins could be modelled as a flat plate while the fish body was ignored. The numerical model could be an ellipse in the studies of Zhang et al. (2009); Hu and Xiao (2014) or a foil shape, such as NACA0012 in the studies of Esfahani et al. (2013); Abbaspour and Ebrahimi (2015); Liu et al. (2018). In some studies, a single fin was modelled as a thick fibre, such as Kim et al. (2016).

Zhang et al. (2009) investigated the influence of chord-thickness ratio (CR) on a 2D elliptical foil with a prescribed vertical movement. The horizontal motion of the model was fully induced. With the changing of CR, the symmetry of the system was found to be broken and the model developed a horizontal velocity, as illustrated in Figure 2.6(a).

Hu and Xiao (2014) further tested the asymmetry problem with a 3D elliptical foil by varying its aspect ratio (AR), as shown in Figure 2.6(b). Results indicated that the induced translational velocity could increase along with AR. Meanwhile, during the evolution procedure, the density of the model would influence its sensitivity to the change of fluid environment, i.e., the wing with a smaller density could react to the transition more quickly.

Esfahani et al. (2013) used a flapping NACA 0012 foil to model the caudal fin of a fish. The length effect was investigated by prescribing the rotational and translational motions on the foil. Results shown in Figure 2.7 indicated that the propulsion efficiency could be improved by manipulating the length of the caudal fin at a moderate Strouhal number.

Abbaspour and Ebrahimi (2015) studied the flow patterns and the hydrodynamic performance of a NACA 0012 foil with two kinds of motions: flapping and undulating. The flapping motion could be considered as a unified motion prescribed on the foil. On the contrary, an ununified motion was imposed to an undulating foil. It was noted that compared to the undulating foil with the same settings, the flapping foil could gain a larger thrust at a lower Strouhal number but also consumed a larger input power.



(a) Rigid foil

(b) Flexible foil

Figure 2.8 Average thrust and utilization wave power coefficients for the foil versus wave encounter frequency (Liu et al., 2018)

Liu et al. (2018) used the NACA 0012 foil to study the hydrodynamic performance of a flexible foil in the wave environment. In order to assess the advantages of the flexible characteristic, a rigid condition was also taken into account. It was noted from Figure 2.8 that compared to a rigid foil, a flexible model could achieve a larger thrust force and a higher propulsive efficiency.

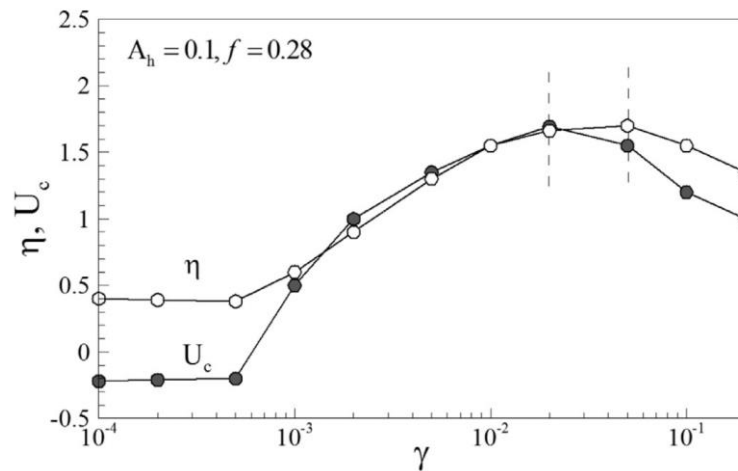


Figure 2.9 Effects of varying the bending stiffness on the cruising speed and the swimming efficiency (Kim et al., 2016)

Kim et al. (2016) used a fibre to simulate the flexible fin with pitch and heaving motions in still water. The motion of the whole model was induced by the active movement of the head part, and the deformation of the fibre was passive. Results in Figure 2.9 indicated that if the fin was either too rigid or too flexible, it could only achieve a slow speed.

In addition to simplified shapes, some researchers also studied the characteristics of actual fish fins. Wang et al. (2010) numerically simulated a rigid pectoral fin with two-degree-of-freedom motions including feathering and lead-lag modes. They found that the biased angle of rowing and feathering motions could affect the hydrodynamic performance of the fin.

Li and Su (2016) further investigated the hydrodynamic performance of a single pectoral fin with a low aspect ratio via an immersed boundary method and found that the optimal phase angle between rowing and feathering motions is 90° , at which a largest thrust and highest efficiency could be generated, as shown in Figure 2.10.

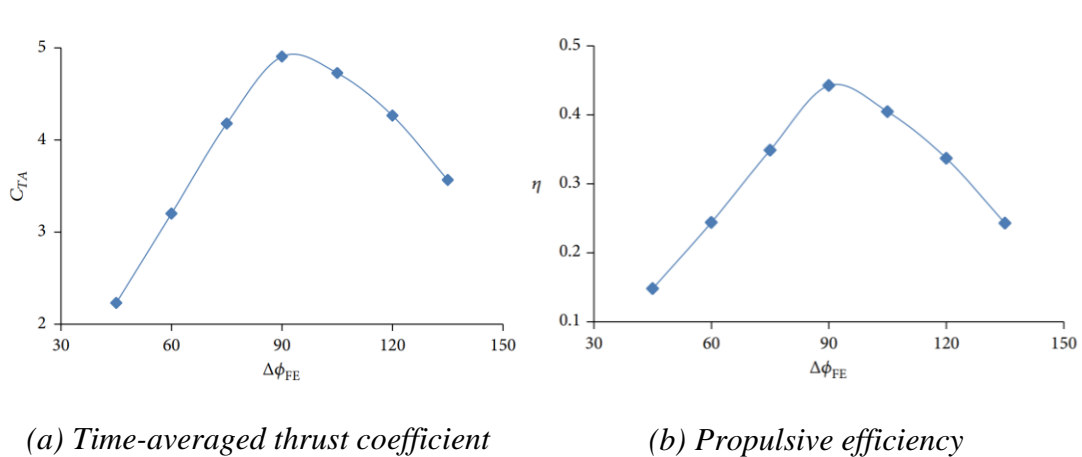
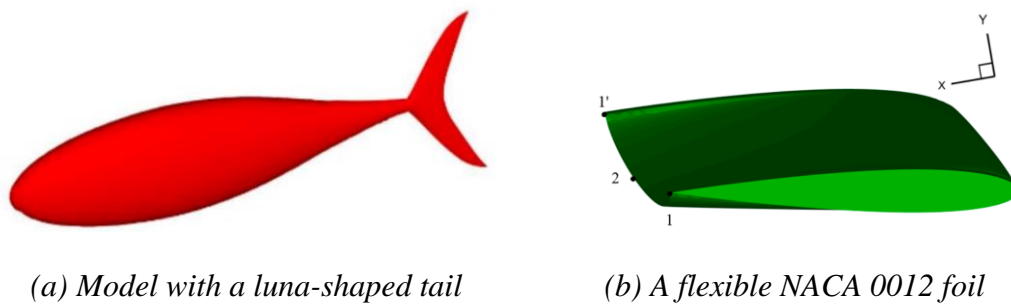


Figure 2.10 Variations of the hydrodynamic performance with the phase angle (Li and Su, 2016)

Some studies compared the rigid and flexible conditions of fins to assess their hydrodynamic performance. Yang et al. (2011) studied the caudal fin of a tuna fish

from two aspects: rigid and flexible. Results revealed that when the caudal fin underwent an oscillating motion, a pair of leading-edge vortices would be generated. Meanwhile, a critical value of the input power coefficient was given as 2.8. This means that when the input power is larger than 2.8, the performance of flexible tail is better than the rigid one. Otherwise, the rigid fin could generate a large thrust and gain a higher efficient.

David et al. (2017) tested the hydrodynamic performance of a rigid foil with a flexible tail. Pitching motion was given on the rigid foil and the deformation of the tail was passive. Results showed that with proper flexural rigidity on the tail, the efficiency could be enhanced up to 3 times compared to the model without the flexible tail.



(c) Experiment with a luna-shaped tail (d) Experiment with a NACA 0012 foil

Figure 2.11 Numerical and experimental models (Zhou et al., 2017)

Zhou et al. (2017) took the spanwise deformation of the caudal fin into account. Two types of caudal shapes were investigated with numerical method: a luna-shaped tail from Thunniform swimmers and a NACA 0012 foil as presented in Figure 2.11(a) and (b), respectively. Meanwhile, corresponding experimental models (Figure 2.11(c) and (d)) were made and tested to validate the results from the numerical simulations. The results showed that the flexibility of the fin in the spanwise direction can influence the formation of vortex rings and consequently affect its swimming performance. Meanwhile, it was noted that under the condition that the phase difference of spanwise flexibility is between 10° and 20° , the tail made of the NACA 0012 foil can achieve a higher mean thrust force and become more efficient than its luna-shaped counterpart.

Park and Sung (2018) investigated the hydrodynamic performance of a self-propelled flexible fin swimming near ground. A prescribed heaving motion was given on the trailing edge of the fin and the rest part was passively deformed. It was noted that when the fin moved near ground, it could gain a faster speed than that far from ground.

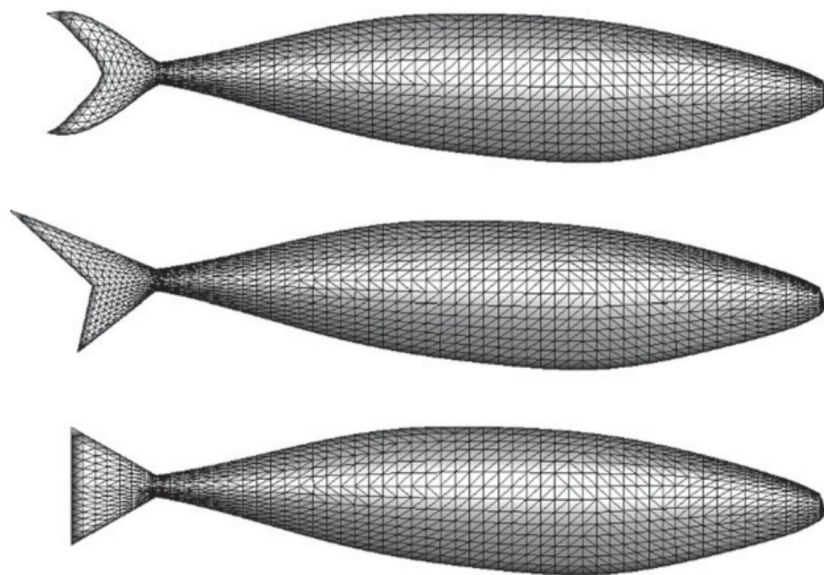


Figure 2.12 Three types of caudal shapes for a virtual swimmer

The influence of fin shape on the hydrodynamic performance has also been investigated by some researchers. Borazjani and Daghooghi (2013) compared the fluid

flow disturbed by a caudal fin with three kinds of shapes, as shown in Figure 2.12. They found that when the Strouhal number was close to $St \approx 0.25$, leading-edge vortices could be formed. Meanwhile, a delta-shaped tail was helpful in the growth of the leading-edge vortices.

Kara and George (2015) also tested the tail shape effects of a simplified self-propelled swimmer with different stiffnesses on its swimming performance. By comparing the swimming speed, forces, torques, consumed and output power of different models, it was noted that no single tail shape could achieve the best performance in all metrics and that the shape and stiffness of the tail interacted in complicated ways.

Krishnadas et al. (2018) studied the hydrodynamic performance of caudal fins that had the same surface area but different aspects of the leading-edge angle (the delta angle). Results showed that a small delta angle could increase the consumed power. The fin with a small delta angle could also generate thrust if the area of the downstream surface was large enough to separate the vortices generated by the leading edge.

There have also been studies focusing on the influences of fin rays. A typical series of work to examine the performance of a three-dimensional flexible fin could be found from (Zhu and Shoele, 2008; Shoele and Zhu, 2009, 2010; Zhu and Shoele, 2012) and a typical model employed in the study can be found in Figure 2.13. A number of uniformed Euler-Bernoulli beams was used to model the passive deformation of fin rays and the structural model was combined with a potential flow solver (Zhu and Shoele, 2012). Zhu and Shoele (2008) found that the flexibility of caudal fin can enhance the propulsion efficiency. Subsequent studies were extended to a skeleton-strengthened pectoral fin. Shoele and Zhu (2009) showed that the phase differences between fin rays were important to the performance of the fin. The deformation of fin rays led to the passive deformation of the fin surface, and further increased the generated thrust and propulsion efficiency. Subsequently, Shoele and Zhu (2010) investigated the performance of the pectoral fin during the labriform swimming. Their predicted results revealed that the strengthening of the leading fin ray was vital to the

reduction in the effective angle of attack and the decrease of the consumed power during the recovery stroke. Furthermore, Shoele and Zhu (2012) studied the effects of fin ray stiffness on the thrust generation. A ray-reinforced fin with flapping motions was modelled. Each fin ray and the membrane were treated as a spring and a flexible but inextensible plate, respectively. It was noted that the strengthened leading fin ray could change the characteristics of the wake, i.e., mitigating flow separation.

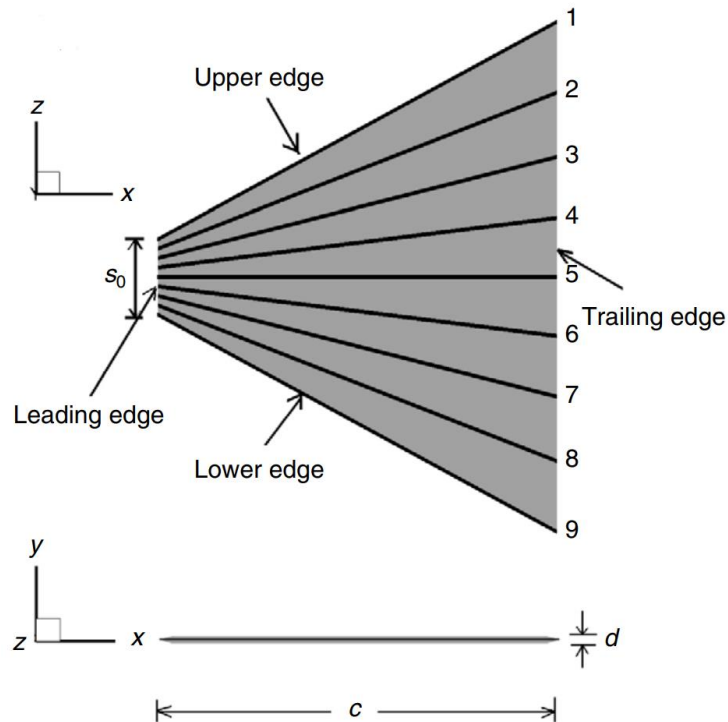


Figure 2.13 A geometrically and structurally simplified fin (Zhu and Shoele, 2008)

2.3 Fish motion with multiple fins

Comparing with the studies about one single fin, investigations on the fish motion with multiple fins are more complicated. Some experimental studies investigated the function of fins by observing and measuring the locomotion of live or robotic fish and provided the most reliable data for analysis and direct evaluation of the robots. Tangorra et al. (2011) developed a robotic fish that contained a modular body, multiple fins with sensory systems, and a neural controller. Each fin could undergo independent

motion. Besides, a mass control system on the fish body was employed to achieve various stability and manoeuvring motions. Benefitting from newly developed measuring techniques, the experimental approach can directly record the changes of fluid field via the Particle Imaging Velocimetry (PIV) method.

Drucker and Lauder (2001) investigated the interaction between dorsal and caudal fins. Their results revealed that the vortices generated by the upstream dorsal fin could interact with those generated by the downstream caudal fin.

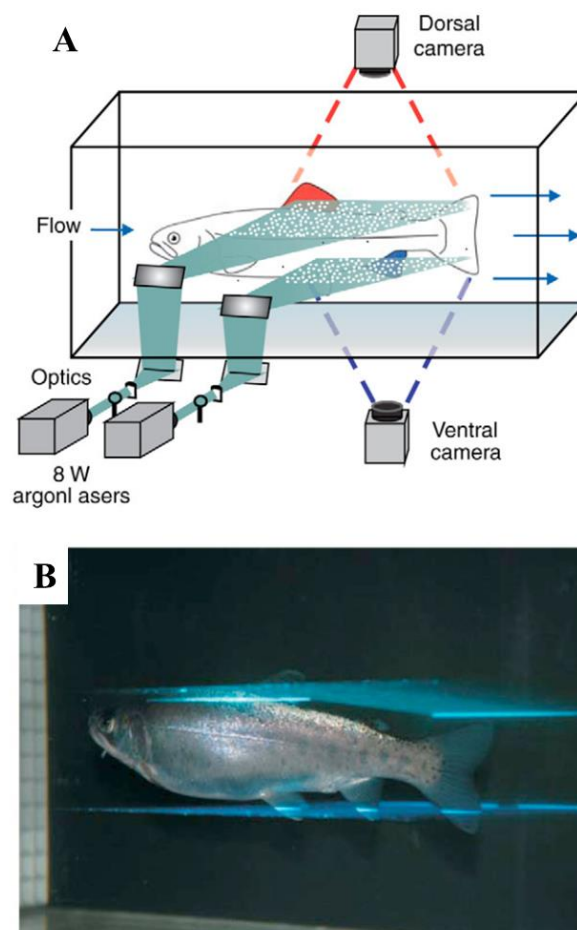


Figure 2.14 Example for live fish experiment with PIV method (Standen and Lauder, 2007)

The study of Standen and Lauder (2007) extended from the dorsal and caudal fins to the influence of an anal fin. Figure 2.14 presents one typical example for measuring the locomotion of dorsal and anal fins in their study. The flow experienced by the caudal fin was found to be greatly affected by the dorsal and anal fins.

Tytell (2006) pointed out that the three-dimensional vortex wake structure associated with a caudal fin should be a hair-pin vortex and linked up with those generated by the dorsal and anal fins as presented in Figure 2.15.

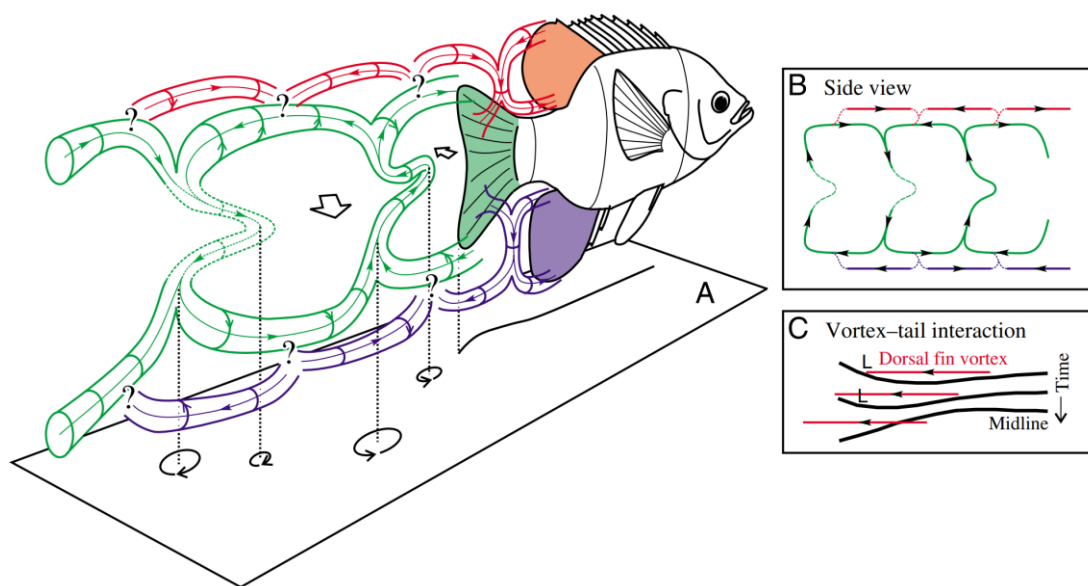


Figure 2.15 Proposed 3D vortex structure around a swimming bluegill sunfish (Tytell, 2006)

Most experimental studies measure steady/tethered fish swimming, i.e., a constant incoming current is applied to keep the fish at a stationary position. However, some other key physical parameters which are beyond the capability of experimental records remain unresolved (such as the surface stress of a swimming fish). While an experimental approach can deal with the morphological, behavioural, and environmental complexities in nature, these complexities sometimes hinder research's ability to arrive at mathematical principles. Numerical simulations are thus increasingly used for fish swimming problems.

One traditional approach to simulating fish swimming was to fix a swimming object in an incoming flow condition, which is equivalent to a water-tunnel experiment and commonly used in some commercial CFD software. Nowadays, simulations of fish swimming tend to allow fish to propel themselves in still water (free-swimming), which could help better understand the unsteady locomotion of fish in the nature. These simulations could be further categorized into two aspects: fin-fin and body-fin.

Extensive studies have focused on the advantages of flow and vortex generation mechanisms for fin-fin interactions and multiple fins over a single fin. It is widely illustrated that, in a tandem configuration, the vortices generated by the upstream fin travel backward and interact with the downstream one, influencing its thrust generation and the overall propulsion efficiency (Broering and Lian, 2012; Kourosh and Qiang, 2015).

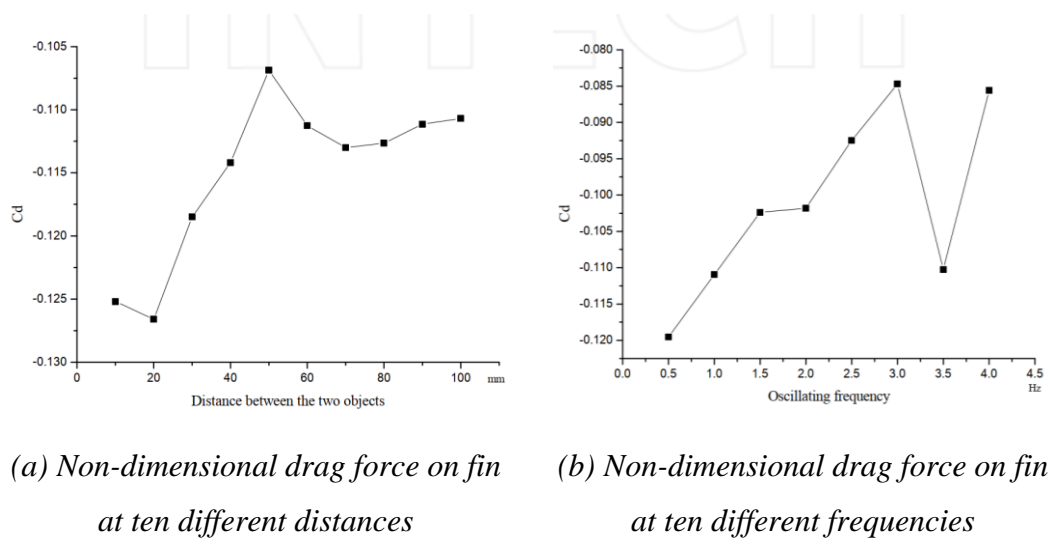


Figure 2.16 Variation of force on the downstream fin with ten different distances and frequencies (Zhang et al., 2013)

Zhang et al. (2013) carried out a two-dimensional numerical simulation for a simplified undulating fin in the wake of a periodic oscillating plate with the ANSYS Fluent software. With a systematic parametric study, the results, as shown in Figure

2.16, illustrated that the downstream fin could create a larger thrust if the fin was located in a shorter distance away from the plate, and the plate oscillated with a lower frequency and larger amplitude.

Uddin et al. (2015) used two tandem flags to emulate the anterior and posterior part of the fish body to study the interactions between flexible bodies and vortices. The passive flapping motion on the upstream flag was induced by the uniform incoming flow. Prescribed pitching and heaving motions were given on the head of the downstream flag. It was noted that the heaving phase could influence the downstream flag more than the pitch phase, and that by adjusting the heaving and pitching amplitudes, drag could be minimized. They concluded that the fish might adjust its head motion to accommodate with the vortical wake for minimizing the drag force.

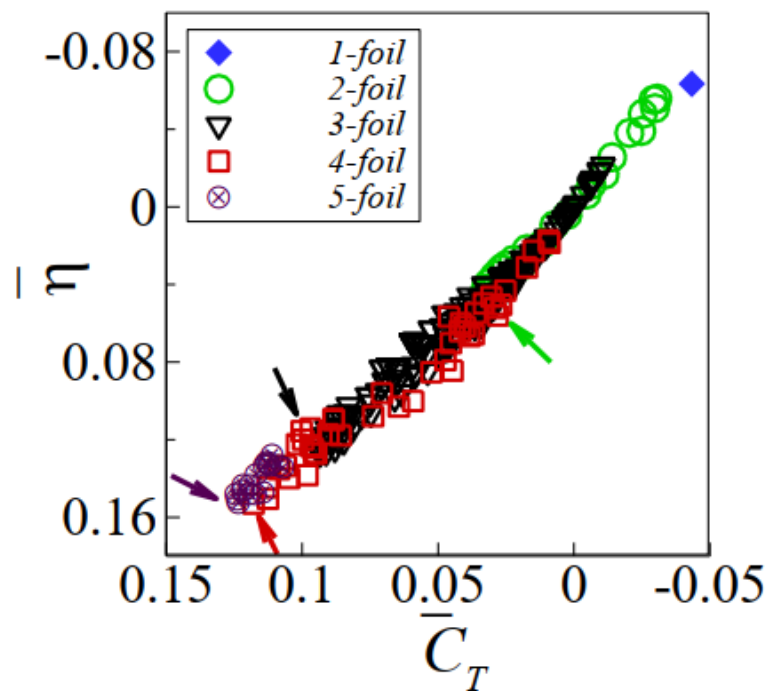


Figure 2.17 Overall propulsive efficiency versus overall thrust coefficient. The arrows mark the optimal cases in different number tandem foils (Yuan et al., 2015)

Yuan et al. (2015) studied the hydrodynamic performance of multiple tandem foils. The number of the foils was gradually increased, and all foils were placed in line with prescribed pitching motion. It was found that the performance of the whole system was not significantly improved with an increase in the foil number, as illustrated in Figure 2.17. The number of the foils with the optimal performance was two, and the averaged performance converged when the number exceeded three.

Guido et al. (2017) examined two fish-like bodies with two different swimming patterns. For the first pattern, both motions on the two bodies were pre-specified. Results illustrated that this prescribed pattern could not sustain synchronized motions of the two bodies. The second pattern was to prescribe a steady gait on the prior body and let the latter body adapt with the vortices generated by the prior one, as presented in Figure 2.18. Results showed that the energy consumption for the latter body to remain the synchronized motion reduced and the swimming efficiency for the whole system increased. It was noted that the vortices could be captured and made good use of by the swimmers, and thus were beneficial.

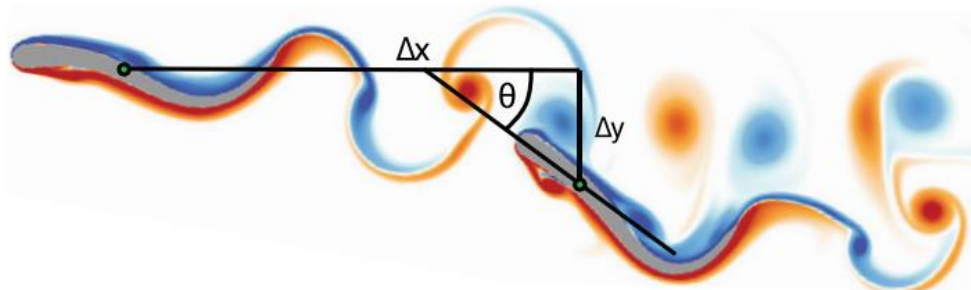


Figure 2.18 The prior body swims along the horizontal line, the follower adapt with the vortices relative to the leader (Guido et al., 2017)

In recent years, the interaction of body-fin and fin-fin has been taken into account with more realistic fish models in CFD simulations under either tethered-swimming (a constant velocity of the incoming flow is specified, and the fish is not allowed to move freely) or free-swimming (the fish can move freely) conditions. The geometry and

kinematics of a three-dimensional fish can be obtained from the relevant experimental measurement. In some studies, the dorsal and anal fins of fish were geometrically included in the fish model while the fins only moved along with the fish body without considering their individual kinematic motions (Borazjani et al., 2012; Borazjani, 2013; Han et al., 2016; Li et al., 2016). Indeed, it is technically a challenging task to model a free-swimming fish body together with their individual fins motion. While the self-propelling (free-swimming) arrangement requires additional coupling of hydrodynamics and body-dynamics, the main challenge is to handle the complex deformations caused by the locomotion.

Liu et al. (2017a) studied a carangiform fish under the tethered-swimming condition with three established CFD models, as shown in Figure 2.19, given the name of M1 (fish body with dorsal, anal and caudal fins), M2 (body-caudal fin) and M3 (caudal fin only). Comparing results from all three models, they concluded that the drag force of the fish body could be reduced if the interaction among all three fins was taken into account even though the individual motions of anal and dorsal fins were not numerically modelled in M1.

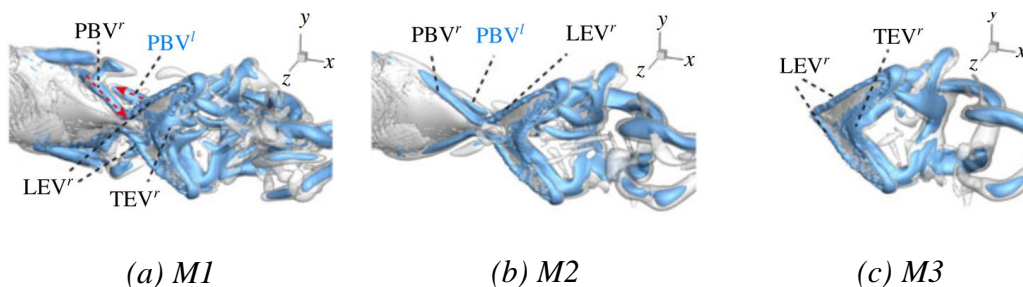


Figure 2.19 Sketches of three models (Liu et al., 2017a)

Yu et al. (2011) investigated the tethered swimming of a model with an undulating fish body and a pair of fixed pectoral fins. Results revealed that a pair of vortices could be formed immediately behind the pectoral fins and it could interact with the undulating fish body.

More sophisticated studies have also been carried out, taking into account individual fin motions in their fish models. Xu and Wan (2012) studied the self-propelled motion of a fish with a pair of rigid pectoral fins while flapping and feathering motions of the fins were considered. It was found that adjusting parameters of fin motions would change the forces generated by the fins and consequently the fish motion.

However, experimental findings on live fish suggest that the fin rays of real fish have different kinematic locomotion parameters (Lauder and Madden, 2007; Li et al., 2018). Wang et al. (2012) simulated the vortex structures of a 3D fish-like swimmer with finlets. The finlets were simplified as thin rigid plates and undulated with the body. It was found that as the finlets were near the caudal peduncle, it could reuse the local flow around the caudal peduncle without changing the structures.

2.4 Concluding remarks

In this chapter, a comprehensive review has been made on the relevant topics about fish swimming, including body motion, single fin studies and fish motion with multiple fins. Summarising from previous studies, the following problems could be further investigated:

1. Most existing publications, especially in some experimental studies, treated the swimming speed as a known input. Comparing with real conditions in nature, the predicted CFD results should be able to explore the kinematic and morphological parameter map beyond experimental observation.
2. CFD studies do not necessarily need to be limited to any stable forward motions. Instead, it can be expanded to various unstable or manoeuvring situations.
3. As real aquatic creatures are 3D in nature, the CFD tool should be able to simulate 3D problems.

4. Most existing research simplified fish fins in fish swimming studies. However, it is necessary to take into consideration the morphological changes in the fin shape while studying fish swimming behaviour.
5. With the development of the simulation methods, it is necessary to investigate an entire fish including different functional fins with their own motions. To be more realistic, fish fins should be flexible. Generally, two types of flexibility have been presented in past studies: (a) the model deforms passively due to fluid forces and (b) the deformation kinematics of the model is prescribed. In the rest parts of the present thesis, the flexibility of the model is achieved by the latter method.

Therefore, the following chapters of this thesis try to achieve these goals listed above with an in-house developed CFD code.

Chapter 3 Numerical Methods

3.1 Introduction

As the interactions between fluid field and the fish model are complicated, several numerical problems are required to be solved, including fluid flow modelling, mesh motion handling, fish motion simulation and fluid-structure coupling. A general sketch in Figure 3.1 is given to illustrate the structure of the present tool, including both fluid and structure parts.

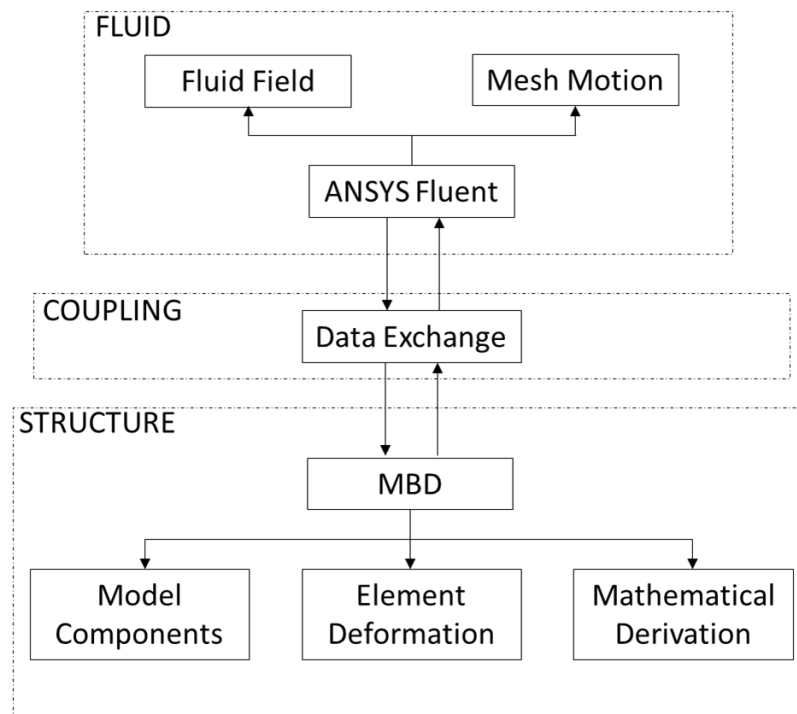


Figure 3.1 Sketch of present tool for solving Fluid Structure Interaction (FSI) problems

In this chapter, detailed descriptions of the fluid solver will be given in Section 3.2, including the numerical schemes and mesh motion handling. The structure part is based on the theory of Multi-Body Dynamics and is explained in Section 3.3. Present methodology could cope with the complex dynamics of body and multiple rigid and/or

deformable fins locomotion. Major components of the model dynamics include the calculation of force, acceleration, velocity, and position for the multi-body system. An in-house code is developed and embedded as User Defined Function (UDF) in ANSYS Fluent. In Section 3.4, the coupling procedure between the fluid solver and the structure code will be introduced. Finally, an example of a pufferfish model, including the model establishment, FSI response calculation and performance parameter, will be presented in Section 3.5. This model will be further employed in Chapter 5 and Chapter 6 for comprehensive investigations.

3.2 Fluid Dynamics

3.2.1 Governing Equations and Numerical Methods

For fish swimming problems, the fluid, i.e., water, can be assumed to be incompressible. The governing equations for incompressible fluid flow are the following continuity and momentum equations:

$$\begin{aligned}\nabla \cdot \vec{u} &= 0 \\ \frac{\partial \vec{u}}{\partial t} + (\vec{u} \cdot \nabla) \vec{u} &= -\frac{1}{\rho} \nabla p + \frac{\mu}{\rho} \nabla^2 \vec{u}\end{aligned}\quad (3.1)$$

where $\vec{u} = (u, v, w)$ is the fluid velocity vector, p is the fluid pressure, μ is the fluid viscosity and ρ is the fluid density.

In order to solve the fluid flow, the equations must be discretised and solved numerically. The fluid field in present study is solved using the commercial software ANSYS Fluent, which is a CFD tool based on the Finite Volume Method (FVM). Various schemes can be chosen in ANSYS Fluent and those adopted in this thesis will be introduced briefly in this part.

For time-dependent flows, the discretised form of the generic equation for transport of a scalar quantity ϕ in integral form for an arbitrary control volume V is as:

$$\int_V \frac{\partial \rho \phi}{\partial t} dV + \oint \rho \phi \vec{v} \cdot d\vec{A} = \oint \Gamma_\phi \nabla \phi \cdot d\vec{A} + \int_V S_\phi dV \quad (3.2)$$

where ρ is water density, \vec{v} is the velocity vector, \vec{A} is surface area vector, Γ_ϕ is diffusion coefficient for ϕ , $\nabla \phi$ is gradient of ϕ , and S_ϕ is source of ϕ per unit volume.

In ANSYS Fluent, the flow problem could be solved in either separated or coupled way with pressure-based solver. In this work, pressure-velocity decoupling is achieved by enabling Non-Iterative Time Advancement (NITA) and selection of Fractional Step Method (FSM). The NITA scheme does not require outer iterations and is thus less CPU intensive compared to iterative schemes.

A first-order implicit time marching scheme is adopted for the transient terms. An advantage of this implicit scheme is that it is stable with respect to the time step size.

Let us set the function $F(\phi) = \frac{\partial \phi}{\partial t}$ which incorporates any spatial discretization, and an implicit time integration to evaluate ϕ^{n+1} at the next time level could be expressed as:

$$\phi^{n+1} = \phi^n + F(\phi^{n+1}) \cdot \Delta t \quad (3.3)$$

A second-order upwind scheme is employed for the discretisation of the convective term. Quantities at cell faces are computed using a multidimensional linear reconstruction approach for second-order accuracy. Higher-order accuracy is achieved at cell faces through a Taylor series expansion of the cell-centred solution about the cell centroid. The face value ϕ_f is computed as:

$$\phi_{f,sou} = \phi + \nabla \phi \cdot \vec{r} \quad (3.4)$$

where ϕ and $\nabla \phi$ are the cell-centred value and its gradient in the upstream cell, and \vec{r} is the displacement vector from the upstream cell centroid to the face centroid.

A Least Squares Cell Based approach is employed for the gradient terms. This is the default gradient method in the ANSYS Fluent solver because the solution is supposed to vary linearly and it is less expensive to compute comparing with the other methods, such as cell-based and node-based gradient method. The change in cell values between cell $c0$ and ci along the vector Δr_i from the centroid of cell $c0$ to cell ci can be expressed as:

$$(\nabla \phi)_{c0} \cdot \Delta r_i = (\phi_{ci} - \phi_{c0}) \quad (3.5)$$

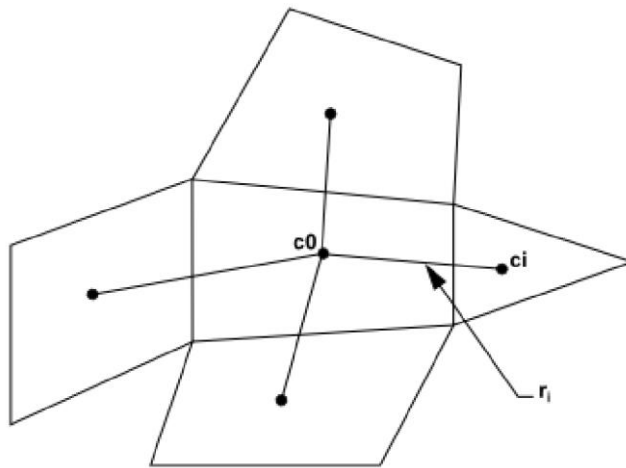


Figure 3.2 Sketch of cell centroid

The gradient at the cell centre $c0$ ($\nabla \phi = \phi_x \cdot i + \phi_y \cdot j + \phi_z \cdot k$) as shown in Figure 3.2 is computed as:

$$\begin{aligned}
(\phi_x)_{c0} &= \sum_{i=1}^n W_{i0}^x \cdot (\phi_{ci} - \phi_{c0}) \\
(\phi_y)_{c0} &= \sum_{i=1}^n W_{i0}^y \cdot (\phi_{ci} - \phi_{c0}) \\
(\phi_z)_{c0} &= \sum_{i=1}^n W_{i0}^z \cdot (\phi_{ci} - \phi_{c0})
\end{aligned} \tag{3.6}$$

W_{i0}^x , W_{i0}^y and W_{i0}^z are the three components of the weight that are produced for each of the faces of cell $c0$.

A Second-order scheme is used for pressure interpolation. It reconstructs the face pressure ϕ_f in the following manner:

$$\phi_f = \frac{1}{2}(\phi_0 + \phi_1) + \frac{1}{2}(\nabla \phi_0 \cdot \vec{r}_0 + \nabla \phi_1 \cdot \vec{r}_1) \tag{3.7}$$

where 0 and 1 indicate the cells that share face f , $\nabla \phi_{r,0}$ and $\nabla \phi_{r,1}$ are the reconstructed gradients at cells 0 and 1, respectively, and \vec{r} is the vector directed from the cell centroid toward the face centroid. This method can improve accuracy.

3.2.2 Mesh Motion Handling

Due to the large deformation of the mesh when fish swim, the dynamic mesh module available in ANSYS Fluent is employed. In order to guarantee the mesh quality during each time step of simulation, smoothing and re-meshing functions are employed.

The smoothing method is operated as if the nodes could move with the connected springs. For diffusion-based smoothing, the mesh motion is governed by the diffusion equation:

$$\nabla \cdot (\gamma \nabla \vec{v}) = 0 \tag{3.8}$$

where \vec{v} is the mesh displacement velocity, and γ is the diffusion coefficient used to control how the boundary motion affects the interior mesh motion. Boundary-distance-based diffusion is used to preserve the mesh quality in the vicinity of the moving boundary. The diffusion coefficient γ can be manipulated primarily by adjusting the diffusion parameter α with the equation:

$$\gamma = \frac{1}{d^\alpha} \quad (3.9)$$

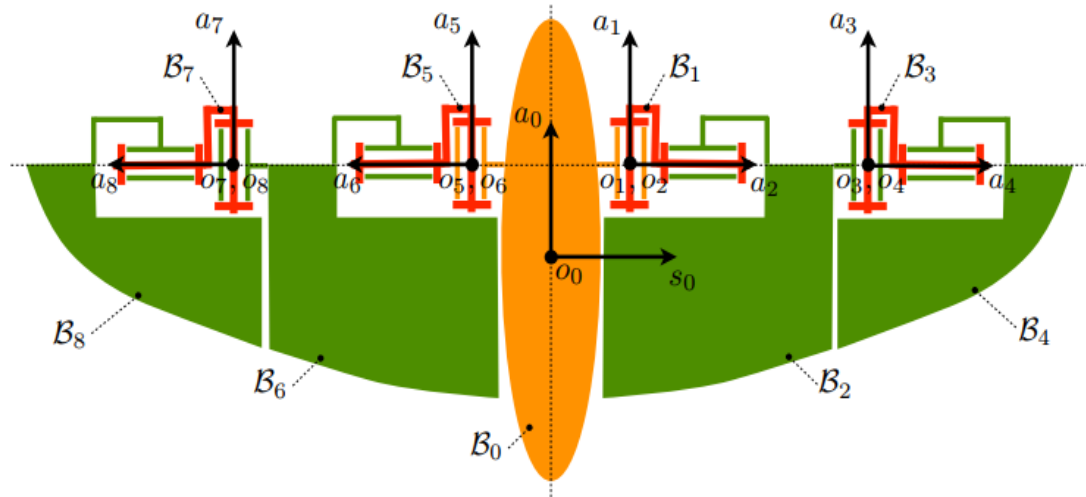
where d is the minimum distance between an interior grid point and boundaries. In simulations of this thesis, a default value of 0 is used for α , which specifies $\gamma = 1$ and yields a uniform diffusion of the boundary motion throughout the mesh. Next, the new position of mesh node will be updated as:

$$\vec{x}_{new} = \vec{x}_{old} + \vec{v}\Delta t \quad (3.10)$$

If the relative motions of the boundaries are large, such as rotational and translational motions are contained, and the skewness and size exceed the expected limits, the remeshing function should be enabled. This means the connectivity of mesh will be reconstructed to guarantee mesh quality. The local cell re-meshing method contains several parameters, including Maximum Cell Skewness, Maximum/Minimum Length Scale and Size Remeshing Interval. The maximum cell skewness is set to 0.9, which is the default value in Fluent for 3D cases. If the skewness of cells is larger than the maximum set skewness, these cells are marked for remeshing. The Max/Min Length Scale specifies the upper/lower limit of cell size, above/below which the cells are marked for remeshing depending on the mesh size of model. Based on these size criteria and the given interval value (which equals to 1 for all the cases in current work), remeshing will occur in each time step. A large remeshing interval value may lead to the negative mesh, but a small value is relatively time-consuming, for three-dimensional modelling particularly.



(a) A serial-like Multi-Body model: Amphibot III (Porez et al., 2014b)



(b) Schematic of a tree-like virtual flying bird (Porez et al., 2014a)

Figure 3.3 Examples of serial- and tree-like structure models

3.3 Structure Modelling

In the present research, the structure modelling part focuses on solving the problem of biomimetic locomotion. The locomotion of a fish may include multiple degrees of freedom, such as translation and rotation. Fish forward motion induced by the undulation of body or fins also need be computed from numerical FSI simulations. In addition, fish fins may undergo independent locomotion, which is different from main fish body. It is thus very challenging to use traditional rigid body dynamics to solve this problem. To cope with this, the dynamics of the models in present study is handled by a Multi-Body Dynamics (MBD) method, based on previous work (Porez et al., 2014a; Porez et al., 2014b; Hu, 2016). The whole algorithm is written as User Defined Function (UDF) and compiled into ANSYS Fluent.

3.3.1 Multi-Body Model Description

A mobile Multi-Body model is comprised of various linked elements. According to the definition given by Khalil, a *serial-* or *tree-like* structure can be nominated to describe the formation of a model. Typical serial- and tree-like models were established in the studies of Porez et al. (2014b) and Porez et al. (2014a), as shown in Figure 3.3. The serial-like model can solve the problem of undulatory fish locomotion as all the elements are in one line. Regarding the tree-like model, it can take more comprehensive factors into account, such as median fins of a fish or a pair of wings for a flying bird.

A serial-like Multi-Body Dynamics solver was developed and combined with a Computational Fluid Dynamics (CFD) tool to investigate a simplified 2D self-propelled fish by Hu (2016). Built on top of her work, in the present project the previously implemented serial-like MBD solver is further extended and a tree-like solver is developed. Meanwhile, the serial-like algorithm can be considered as a special case of the tree-like one. In general, a Multi-Body Dynamics-based model is considered as being constructed with several separate elements/bodies as given in Figure 3.4(a). A reference element B_0 is selected which is used as a starting element for both models. The primary difference between the two models is that, in a serial-like model, the n th element is the terminal body, but a tree-like model has more than one terminal body. There are two types of coordinates in this MBD system, i.e., the earth coordinate O_e and the local coordinate O_i . The reference element B_0 is specified and coloured in grey in Figure 3.4. Several branches exist, indicated by blue dashed lines with arrows, relative to the reference element B_0 . Apart from reference element B_0 , other elements in the branches are given numbers in the orders of 1 to the last element. Two adjacent elements are connected with one virtual joint H_i . At each joint, only one-degree-of-freedom motion can be imposed, i.e., rotational motion about local z axis. By adding more than one virtual joint, multi-degree of freedoms can be

achieved. An index vector a_i is employed to store element/body connection information, which is vital for a tree-like MBD system.

This MBD algorithm can also be referred to as a hybrid algorithm because there are two types of input methods defined for joints: actuated and passive input. For a model with multiple joints, the input rule of each joint does not need to be unified. A Boolean variable b_j is introduced to define the joint type in the algorithm as:

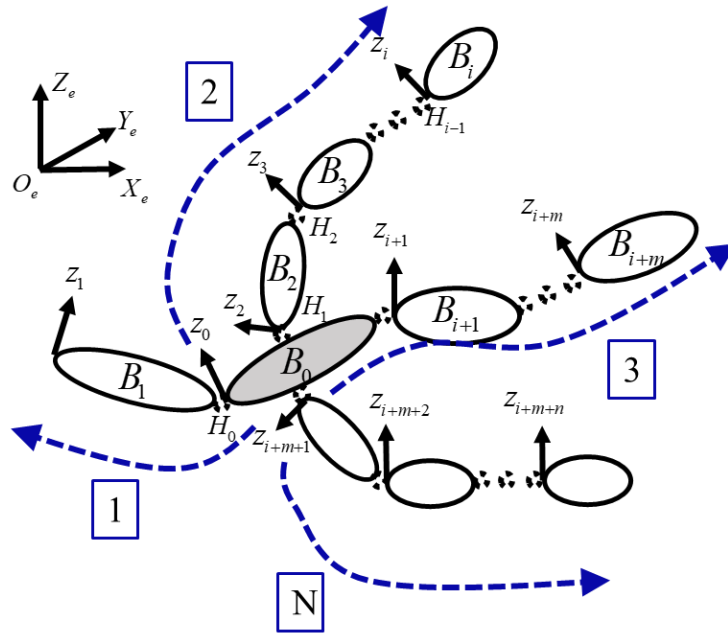
$$\forall j, b_j = \begin{cases} 1 & \text{actuated, } \ddot{\theta}_j(t) \text{ is imposed} \\ 0 & \text{passive, } \tau_j(t) \text{ is imposed} \end{cases} \quad (3.11)$$

An actuated joint defines the angular acceleration $\ddot{\theta}_j$ on a joint and two successive elements can rotate around the joint. The motion of the whole system is induced by the prescribed motions on hinges. For a passive joint, the torque acting upon the joint is defined. A passive joint can be considered as a rotational spring with stiffness K and damping R . The torque τ_j given on a joint can be computed as:

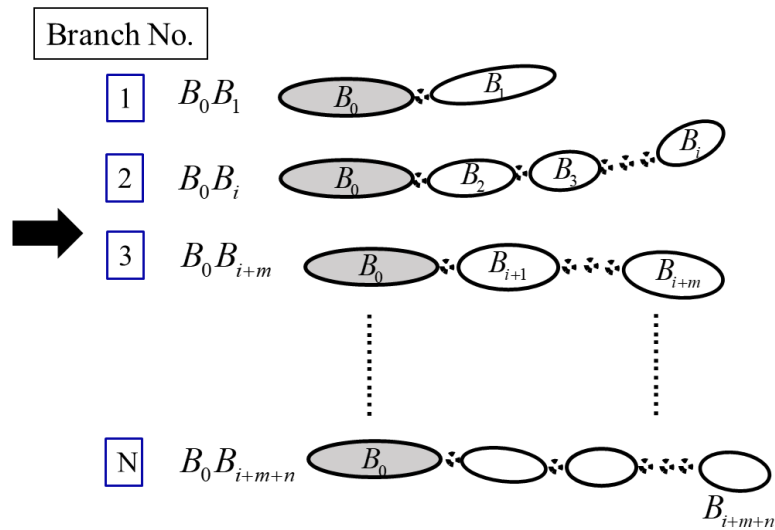
$$\tau_j = -R \cdot \dot{\theta}_j - K \cdot \theta_j \quad (3.12)$$

With a passive joint, τ_j is imposed and the induced angle θ_j can be obtained at each time step. The passive connection can only be applied under the condition that the motion of the reference element is prescribed, and the motions of other elements are passively induced.

Two directions are specified in the model, i.e., forward recursion and backward recursion. The forward recursion means that motion variables are calculated from the reference body to all the terminal bodies. While for backward recursion the calculation for variables starts from the terminal bodies to the reference body.



(a) A general tree-like/structured model



(b) Serial-like/structured model

Figure 3.4 Sketch of Multi-Body tree-like and serial-like model. The tree-like model has one reference body (as coloured in grey) and more than one terminal bodies ($B_1, B_i, B_{i+m}, B_{i+m+n}$). The serial-like model has only one reference body and one terminal body. A tree-like model can be treated as being composed of several branches of serial-like models and all the branches share one reference body.

3.3.2 Deformation on each body/element

Unlike the traditional method that considers structural flexibility as the deformation of a whole model, present method separates the model into several bodies. There are two methods to achieve structural flexibility of a model with the present MBD method: each body could be deformed respectively or obey particular rules to make the whole system flexible, i.e., bodies in the system can be either deformable or rigid.

For a deformable body, each mesh node on the body has been prescribed with a different motion profile. At every time step, new node positions will be calculated. This is written in the macro `DEFINE_GRID_MOTION` in the UDF.

The rigid body condition is easier to implement than the deformable one, because every node on the body follows a uniform motion. By taking advantage of the UDF macro `DEFINE_CG_MOTION`, only the velocity of each body need be known.

3.3.3 Mathematical Derivations

Several vital variables are defined in this part before introducing the coupling procedures.

3.3.3.1 Euler Transformation

Transformation between two successive local coordinates is completed based on the Newton-Euler frame. A homogeneous transformation matrix ${}^j\mathbf{T}_i$ which transforms the initial location/position from a local coordinate of body $B_i(O_i, x_i, y_i, z_i)$ to body $B_j(O_j, x_j, y_j, z_j)$ is defined as:

$$\begin{aligned}
{}^j\mathbf{T}_i &= \text{rot}(x_i, \alpha_j) \text{trans}(x', d_j) \text{rot}(z'', q_j) \text{trans}(z^*, r_j) \\
&= \begin{pmatrix} \cos q_j & -\sin q_j & 0 & d_j \\ \cos \alpha_j \sin q_j & \cos \alpha_j \cos q_j & -\sin \alpha_j & -r_j \sin \alpha_j \\ \sin \alpha_j \sin q_j & \sin \alpha_j \cos q_j & \cos \alpha_j & -r_j \cos \alpha_j \\ 0 & 0 & 0 & 1 \end{pmatrix} \quad (3.13)
\end{aligned}$$

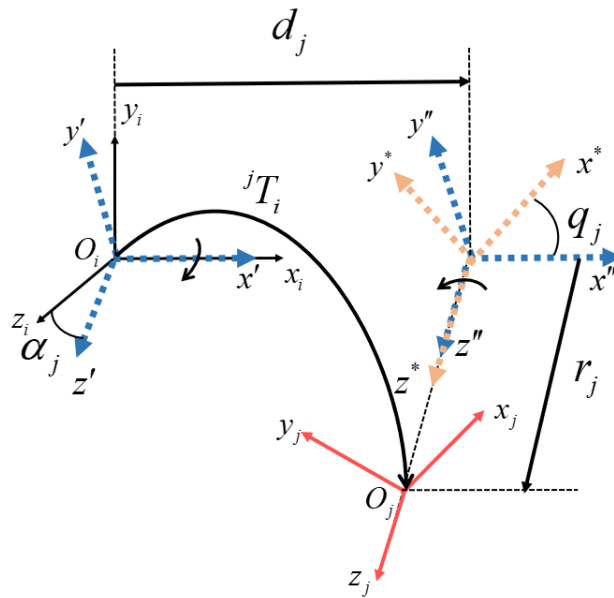


Figure 3.5. Coordinate transformation: transformation matrix jT_i from local coordinate O_i of body B_i to the local coordinate O_j of body B_j

Referring to Figure 3.5, transformations operate along x and z axis in order. The local coordinate of body $B_i(O_i, x_i, y_i, z_i)$ firstly rotates around x_i axis with an angle of α_j , translates along x' axis with a distance d_j , then rotates about z'' axis with an angle of q_j , and finally translates along z^* axis with the distance r_j to get the final local coordinate of body $B_j(O_j, x_j, y_j, z_j)$.

When the angular motion θ_a on the hinge connecting two consecutive bodies is specified, the transformation matrix ${}^j\mathbf{T}_i(\theta_a)$ is divided into one (3×3) rotation matrix ${}^j\mathbf{R}_i(\theta_a)$ and one (3×1) position vector ${}^j\mathbf{P}_i$ as:

$$\begin{aligned} {}^j\mathbf{T}_i(\theta_a) &= \text{rot}(x_i, \alpha_j) \text{trans}(x', d_j) \text{rot}(z'', q_j + \theta_a) \text{trans}(z^*, r_j) \\ &= \begin{pmatrix} {}^j\mathbf{R}_i(\theta_a) & {}^j\mathbf{P}_i \\ 0 & 1 \end{pmatrix} \end{aligned} \quad (3.14)$$

The angle θ_a is determined by looking through the index vector a and it is added to the rotational z axis. An adjoint map operator $Ad_{j g_i}$ is introduced for the transformation of inertia, force and velocity from body B_i to body B_j and is defined as:

$$Ad_{j g_i} = \begin{pmatrix} {}^j\mathbf{R}_i(\theta_a) & {}^j\mathbf{R}_i(\theta_a) {}^i\hat{\mathbf{P}}_j^T \\ 0 & {}^j\mathbf{R}_i(\theta_a) \end{pmatrix} \quad (3.15)$$

${}^i\hat{\mathbf{P}}_j$ is a (3×3) skew-symmetric tensor and can be obtained from the (3×1) position vector ${}^i\mathbf{P}_j$ as:

$${}^i\hat{\mathbf{P}}_j = \begin{pmatrix} 0 & d_j & r_j \cos \beta_j \\ -d_j & 0 & -r_j \sin \beta_j \\ -r_j \cos \beta_j & r_j \sin \beta_j & 0 \end{pmatrix} \quad (3.16)$$

3.3.3.2 Force and Acceleration

The fluid force of each element, which is also known as external force, is obtained by the fluid solver at each time step and notated as a (6×1) force vector $F_{ext,j}$. It includes

force and moment in three directions (X, Y and Z). The net force β_j^* on the terminal body is defined as:

$$\beta_j^* = \beta_j - F_{ext,j} \quad (3.17)$$

where β_j is a (6×1) Coriolis and centrifugal forces vector with the following derivation:

$$\beta_j = \begin{pmatrix} -\Omega_j \times (MS_j \Omega_j) + \Omega_j \times (M_j V_j) \\ \Omega_j \times (I_j \Omega_j) + MS_j (\Omega_j \times V_j) \end{pmatrix} \quad (3.18)$$

In Equation (3.18), MS_j , M_j and I_j are the (3×3) tensor of body mass, the (3×3) tensor of first inertia moments and the tensor of angular inertia of the local coordinate origin of body B_j , respectively. The inertia tensor M_j can be defined as:

$$M_j = \begin{pmatrix} M_j & -M\hat{S}_j \\ M\hat{S}_j & I_j \end{pmatrix} \quad (3.19)$$

For the other elements, the net force and generalized inertia tensor of each element can be calculated accordingly, depending on the different type of joint that connects two successive elements. Meanwhile, the net force and inertia tensor are accumulated backward from the terminal elements in all the branches to the reference body. With actuated connection, if it is supposed that body B_i is followed by body B_j , the generalized inertia tensor and net force between these two bodies are calculated via the following equations:

If $b_j = 1$:

$$\mathbf{M}_i^* = \mathbf{M}_i + \text{Ad}_{i_{g_j}}^T \mathbf{M}_j^* \text{Ad}_{i_{g_j}} \quad (3.20)$$

$$\beta_i^* = (\beta_i - F_{ext,i}) + \text{Ad}_{i_{g_j}}^T \left(\mathbf{M}_j^* (A\ddot{\theta}_j + \zeta_j) + \beta_j^* \right)$$

For passive connection, with the torque τ_j on the joint as input, these two variables are computed as:

If $b_j = 0$:

$$\mathbf{M}_i^* = \mathbf{M}_i + \text{Ad}_{i_{g_j}}^T \kappa \text{Ad}_{i_{g_j}} \quad (3.21)$$

$$\beta_i^* = (\beta_i - F_{ext,i}) + \text{Ad}_{i_{g_j}}^T \left(\kappa \zeta_j + \mathbf{M}_j^* A (A^T \mathbf{M}_j^* A)^{-1} (\tau_j - A^T \beta_j^*) + \beta_j^* \right)$$

where κ is a transition variable expressed as:

$$\kappa = \mathbf{M}_j^* - \mathbf{M}_j^* \left(A (A^T \mathbf{M}_j^* A)^{-1} A^T \right) \mathbf{M}_j^* \quad (3.22)$$

By accumulating the force and generalized inertia tensor from the terminal body backward to the reference element, the acceleration of reference element B_0 can be estimated as:

$$\dot{\eta}_0 = -(\mathbf{M}_0^*)^{-1} \beta_0^* \quad (3.23)$$

3.3.3.3 Velocity, Torque and Position

The status of the whole system relative to the earth coordinate is determined by the reference body $B_0(O_0, x_0, y_0, z_0)$. Its velocity η_0 in the global coordinate is solved using a 4th order Runge-Kutta scheme as follows:

$$\eta_0|_{t+\Delta t} = \begin{pmatrix} V_0^T \\ \Omega_0^T \end{pmatrix} \Big|_{t+\Delta t} = \eta_0|_t + \frac{\Delta t}{6} \left(\dot{\eta}_0|_t^1 + 2\dot{\eta}_0|_{t+\frac{\Delta t}{2}}^2 + 2\dot{\eta}_0|_{t+\frac{\Delta t}{2}}^3 + \dot{\eta}_0|_{t+\Delta t}^4 \right) \quad (3.24)$$

where eV_0 and ${}^e\Omega_0$ represent the (3×1) linear and (3×1) angular velocity vector in X, Y, Z direction of earth coordinate, respectively. A (4×1) orientation vector eQ_0 is obtained through the Quaternion-derived rotation vector of ${}^e\Omega_0$ to determine the orientation matrix eR_0 .

The status for the rest elements is calculated recursively from the reference element forward to the terminal element. For instance, if B_j is connected to B_i by an actuated joint, which means that the prescribed angular acceleration is given, the velocity and torque will be calculated and output. If the joint type is passive joint, i.e., the stiffness and damping are given, the angular acceleration can also be obtained besides the velocity.

For an actuated joint connecting elements B_j and B_i , the velocity of element B_j is a (6×1) velocity vector denoted as η_j and its value should be transferred from its anterior element B_i as:

$$\eta_j = \begin{pmatrix} V_j^T \\ \Omega_j^T \end{pmatrix} = Ad_{j_{g_i}} \eta_i + \dot{\theta}_a A \quad (3.25)$$

where V_j and Ω_j represent the linear and angular Galilean velocity vector in three dimensions, respectively; A is a (6×1) union vector. By applying time differentiation to Equation (3.25), the acceleration of element B_j relative to its own coordinate can be expressed as:

$$\dot{\eta}_j = Ad_{j_{g_i}} \dot{\eta}_i + \ddot{\theta}_a A + \zeta_j \quad (3.26)$$

Here, ζ_j represents the acceleration induced by the acceleration transformation between local coordinates of two successive bodies through the detailed expression as referred to Porez et al. (2014a):

$$\zeta_j = \begin{pmatrix} \left({}^jV_i + {}^jP_i \times {}^j\Omega_i \right) \times \dot{\theta}_a b \\ \dot{\theta}_a {}^j\Omega_i \times b \end{pmatrix} \quad (3.27)$$

b stands for the (3×1) union vector. The torque on the hinge can be calculated with the Equation (3.28).

$$\tau_j = A \left(M_j^* \left(Ad_{j_{g_i}} \dot{\eta}_i \right) + \beta_j^* \right) \quad (3.28)$$

If element B_j is connected to B_i with a passive spring, the derivation of the angular acceleration on the hinge is based on the torque as:

$$\ddot{\theta}_j = \left(A^T M_j^* A \right)^{-1} \left(\tau_j - A^T \left(M_j^* \left(Ad_{j_{g_i}} \dot{\eta}_i + \zeta_j \right) + \beta_j^* \right) \right) \quad (3.29)$$

The derivation of acceleration for element B_j is the same as the actuated condition as Equation (3.26).

With a (3×1) position vector eP_0 , the transformation matrix eT_0 between the earth coordinate and the reference element is:

$${}^e\mathbf{T}_0 = \begin{pmatrix} {}^eR_0 & {}^eP_0 \\ 0 & 1 \end{pmatrix} \quad (3.30)$$

The position of other elements relative to the global coordinate is also obtained by transforming from the reference body forward to the terminal body using the following equation:

$$\begin{aligned} {}^e\mathbf{T}_j &= {}^e\mathbf{T}_i {}^i\mathbf{T}_j(\theta_a) \\ &= \begin{pmatrix} {}^eR_j & {}^eP_j \\ 0 & 1 \end{pmatrix} \end{aligned} \quad (3.31)$$

where ${}^e\mathbf{T}_i$ and ${}^e\mathbf{T}_j$ are the transformation matrices for elements B_i and B_j ; eR_j and eP_j are the orientation matrix and position vector of element B_j . All the variables are defined in the earth coordinate.

3.4 FSI Coupling Algorithm

When a coupled simulation is performed, both the CFD solver, i.e., ANSYS Fluent, and the structure code, i.e., MBD hybrid algorithm written in the UDF, run simultaneously. Data transferring is needed between the fluid solver and the UDF. As the UDF is compiled into ANSYS Fluent, a two-step process is needed, i.e., first build the UDF and then load the shared library object file from the source code. At the beginning of each time marching step, velocity and position of each body relative to the global coordinate is transferred to Fluent to calculate fluid forces around the fish model. Such information is then delivered back to the MBD code to predict the velocity and position of the fish at the next time step.

The developed in-house code is able to work with ANSYS Fluent in both serial and parallel computing mode. Given that large computational grids are required for three-dimensional self-propelled fish swimming simulations, parallel computing is necessary in the present study to reduce the computational time. There are two kinds of processes involved when Fluent runs in parallel computing mode, i.e., host and node(s). The role of host is for message-passing and displaying purposes. It

communicates with compute node-0 directly, which then distributes the variables to other compute nodes. Detailed description about parallelisation can be found in the ANSYS Fluent UDF manual(ANSYS Fluent, 2013).

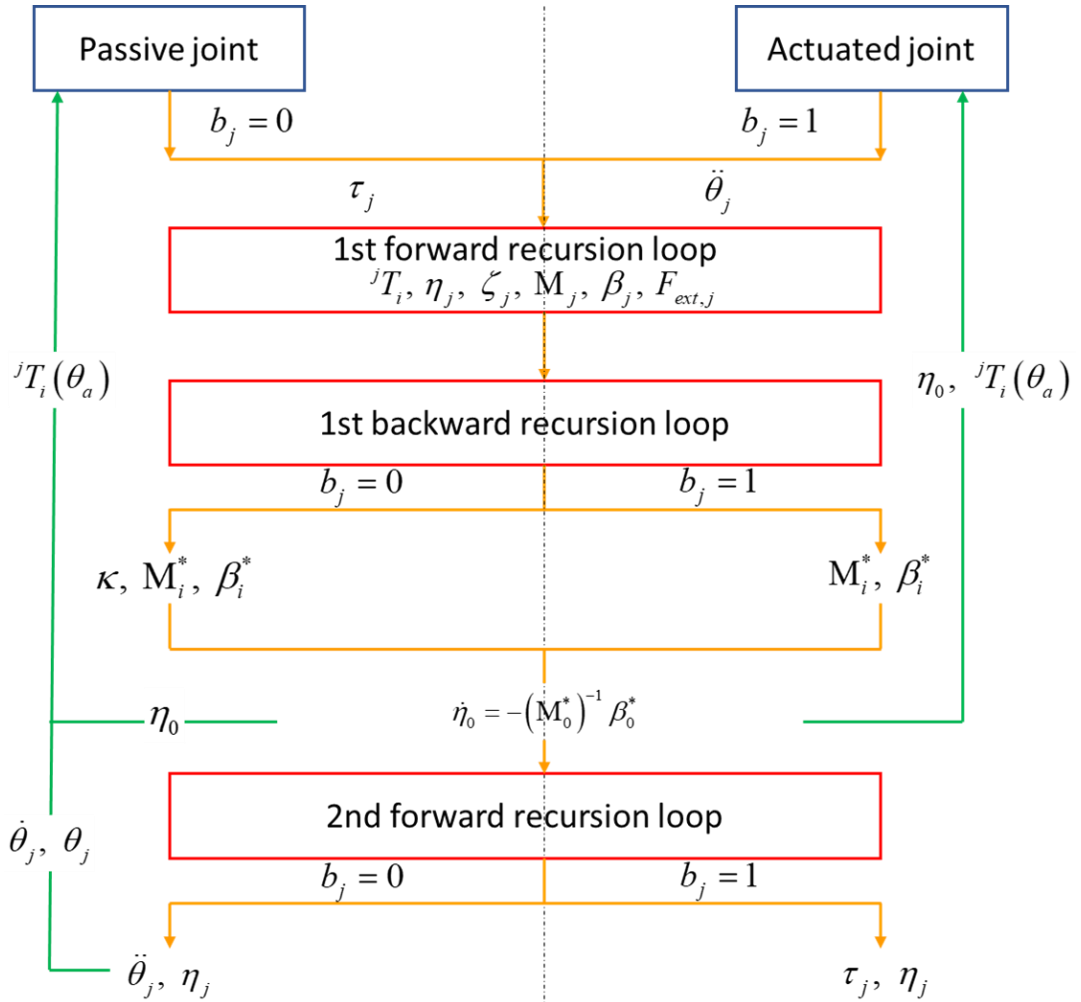


Figure 3.6 Flow chart of the hybrid algorithm (adapted from Porez et al. (2014a))

A brief flow chart about the solution procedures is illustrated in Figure 3.6. A vector $\mathfrak{R}(X_{state}, \dot{\theta}_j, \theta_j)$ collects the status X_{state} of reference body B_0 relative to the earth coordinate, the angular velocity $\dot{\theta}_j$ and the angle θ_j of all the hinges, j in total, in a model:

$$\mathfrak{R}(X_{state}, \dot{\theta}_j, \theta_j) = \mathfrak{R}({}^eV_0, {}^e\Omega_0, {}^eP_0, {}^eQ_0, \dot{\theta}_j, \theta_j) \quad (3.32)$$

This is the input vector at the initialization stage. Meanwhile, the relative position of each element at the initialization is also known, i.e., α_j , d_j , q_j , r_j referring to Figure 3.5, and these values remain the same during the whole simulation. Next, the dynamics of the structure will follow the procedures presented below, which is also the solving method of the hybrid algorithm:

1. 1st forward recursion loop. In this recursion, the status of each element in its local coordinate will be calculated, including the Newton-Euler transformation matrix jT_i , velocity vector η_j , partial acceleration ζ_j , the inertia tensor M_j , the Coriolis and centrifugal forces vector β_j . All the variables are derived forward from the reference element to each of the terminal elements. The external fluid force $F_{ext,j}$ is obtained from the fluid solver at each time marching step.

For $b_j = 0$ and 1,

Calculate	jT_i	Equation (3.13)
	η_j	Equation (3.25)
	ζ_j	Equation (3.27)
	M_j	Equation (3.19)
	β_j	Equation (3.18)
Obtain external force	$F_{ext,j}$	from fluid solver

2. 1st backward recursion loop. For both joint types, the net force β_i^* and generalized inertia tensor M_i^* are calculated in this loop by following the direction backward from the terminal element of each branch to the reference element. This recursion can also be considered as accumulating the net force and the generalized inertia tensor of the whole model on the reference element. Once β_0^* and M_0^* are known, based on Newton's Second Law, the acceleration of the reference element, as well as the whole system, can be

obtained. Generally, to predict a new time step, a 4th order Runge-Kutta explicit time discretization is employed as:

$$\mathfrak{R}|_{t+\Delta t} = \mathfrak{R}|_t + \frac{\Delta t}{6} \left(\dot{\mathfrak{R}}|_t^1 + 2\dot{\mathfrak{R}}|_{t+\Delta t/2}^2 + 2\dot{\mathfrak{R}}|_{t+\Delta t/2}^3 + \dot{\mathfrak{R}}|_{t+\Delta t}^4 \right) \quad (3.33)$$

Here, Δt stands for the time step size. For those elements that are connected with actuated joints, the prescribed angular velocity $\dot{\theta}$ and angle θ are thus predicted. The new Newton-Euler transformation matrix ${}^j\mathbf{T}_i(\theta_a)$ that contains the new angle is updated for the actuated joints.

For $b_j = 0$

Calculate	\mathbf{M}_i^* and β_i^*	Equation (3.21)
	$\dot{\eta}_0$	Equation (3.23)
	η_0	Equation (3.24)

For $b_j = 1$

Calculate	\mathbf{M}_i^* and β_i^*	Equation (3.20)
	$\dot{\eta}_0$	Equation (3.23)
	η_0	Equation (3.24)
	$\dot{\theta}_j, \theta_j$	Equation (3.33)
	${}^j\mathbf{T}_i(\theta_a)$	Equation (3.14)

3. 2nd forward recursion loop. Finally, the algorithm ends with a second forward recursion loop at each time marching step. For those elements that are connected with passive joints, the predicted velocity in its own local coordinate, as well as the angular acceleration on the joint, will be calculated. Furthermore, the angular velocity, angle and new Newton-Euler transformation matrix will be updated. In terms of the actuated joints, the torque could be obtained. The elements that are connected with actuated joints will also gain the new velocity.

For $b_j = 0$

Calculate	$\ddot{\theta}_j$	Equation (3.29)
	$\dot{\theta}$ and θ	Equation (3.33)
	η_0	Equation (3.24)

	η_j	Equation (3.25)
	${}^j\mathbf{T}_i(\theta_a)$	Equation (3.14)
For $b_j = 1$		
Calculate	τ_j	Equation (3.28)
	η_j	Equation (3.25)

3.5 Example of Pufferfish Model

In Chapter 5 and Chapter 6, a self-propelled pufferfish with multiple fins is employed. Detailed information will be listed in the following section as an example of the tree-structure model establishment and motion solving. Important performance parameters will also be given.

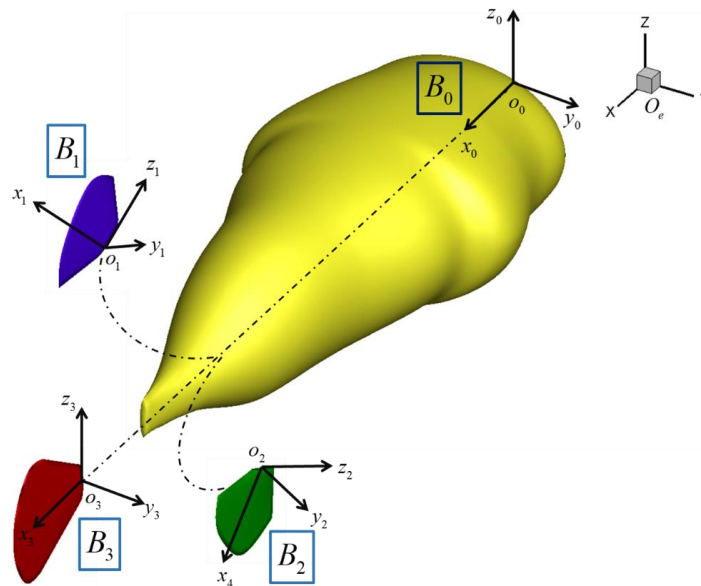


Figure 3.7 Coordinate establishment of a self-propelled pufferfish

3.5.1 MBD Model Establishment

As the swimming of pufferfish is fully induced by the motions of rigid/flexible median fins, the motion of the fish is solved by adopting a Multi-Body Dynamics (MBD) algorithm implemented as a User Defined Function (UDF) in ANSYS Fluent. By adopting the MBD concept, the CFD pufferfish model can be considered as a tree-

structured model with four “bodies/elements” and virtual hinges connecting two successive elements as shown in Figure 3.7. To solve this problem, in addition to an earth or global coordinate, a local coordinate is defined for each element. A reference element B_0 is selected to represent the key parameters of fish model, such as the swimming velocity, the position and the orientation relative to earth coordinate. In the present study, the fish body, coloured in yellow in Figure 3.7, is selected as the reference element B_0 and the dorsal, anal and caudal fins are set at three different branches numbered as B_1 , B_2 and B_3 .

3.5.2 FSI Response Calculation

The connection between each fin and fish body is considered to be an actuated joint.

1. Update the prescribed kinematic motion of fish fins at the beginning of each time step as described in Section 5.1.1.
2. Calculate hydrodynamic force $F_{ext,i}$ of each element using fluid solver. At each time step, fluid force and moment exerted upon each element are integrated over its surface and then transferred to the MBD solver.
3. Transfer fluid force on each element to the reference element B_0 . The forces on fins are transferred backwards to the reference element, i.e., fish body B_0 , by using the following equations:

for $i = 1, 2, 3$

$$\beta_i^* = \beta_i - F_{ext,i}$$

$$\beta_0^* = (\beta_0 - F_{ext,0}) + \sum_i Ad_{0g_i}^T (M_i^* (A\ddot{\varphi}_i + \zeta_i) + \beta_i^*) \quad (3.34)$$

$$M_0^* = M_0 + \sum_i Ad_{0g_i}^T M_i Ad_{0g_i}$$

4. Obtain the acceleration $\dot{\eta}_0$ from Eq (3.23).

5. Determine the velocity ${}^e\eta_i$ for each element and transfer motion data to the fluid solver. After obtaining the acceleration $\dot{\eta}_0$, the velocity η_0 for reference element can be calculated with Eq (3.24). Once η_0 is estimated, the velocity of other bodies in their local coordinates can be determined in the following way:

$$\eta_i = Ad_{i_{g_0}} {}^e\eta_0 + \dot{\varphi}_i A \quad i = 1, 2, 3 \quad (3.35)$$

Here, the angular velocity $\dot{\varphi}_i$ is the derivation of angular motion φ_i . Velocity for all elements relative to earth coordinate can be obtained as:

$${}^e\eta_i = \begin{pmatrix} {}^eR_i & 0 \\ 0 & {}^eR_i \end{pmatrix} \eta_i \quad (3.36)$$

6. The velocity component of reference element ${}^e\eta_0$ in X direction is denoted as “induced velocity U ” for the whole fish system. Newly updated velocity ${}^e\eta_i$ for each element is sent back to the fluid solver for calculations at the next time step.
7. Repeat steps 1-5 for all time marching steps during a coupled simulation loop.

3.5.3 Important performance parameters

As fish swim freely in water, the swimming Reynolds number is an important parameter to evaluate the propulsion performance. In the present study, it is estimated using the induced time-averaged velocity \bar{U} when a fish approaches a quasi-steady swimming status, the body length L , and the kinematic viscosity ν of water as:

$$\text{Re} = \frac{\bar{U}L}{\nu} \quad (3.37)$$

For the four cases in Chapter 5, Re numbers are equal to 7.3e3, 1.2e4, 1.05e4 and 2.06e4, which are typical values for fish swimming (Anderson et al., 2001).

The comparisons between rigid and flexible fins are carried out by assessing fluid force on fish body and fins, the cyclic-averaged output power \bar{P}_{out} , consumed power \bar{P}_c and the propulsion efficiency η_{eff} . Fluid force is analysed from two aspects: cycle-averaged total force \bar{F}_T and propulsive force F_p . These vital parameters are calculated using the following definitions:

1. Cycle-averaged total force \bar{F}_T . Total force F_T is defined as the sum of forces acting on the fish body F_B , dorsal F_D , anal F_A and caudal F_C fins as:

$$F_T = F_B + F_D + F_A + F_C \quad (3.38)$$

The cycle-averaged \bar{F}_T for each motion cycle can illustrate the development history of the induced velocity U . Based on Newton's Second law, zero \bar{F}_T indicates zero acceleration and thus fish swim at a cruising speed, which is defined as a quasi-steady status in the present work.

2. Propulsive force F_p . In the present study, it is equal to the sum of forces generated by dorsal fin F_D , anal fin F_A and caudal fin F_C as:

$$F_p = F_D + F_A + F_C \quad (3.39)$$

3. Vortex visualisation. The Q-criterion is employed to visualise vortices which are represented by the iso-surface of the 2nd invariant of the velocity gradient tensor defined as:

$$Q = \frac{1}{2} \left(\|\Omega\|^2 - \|\Phi\|^2 \right) \quad (3.40)$$

where Ω and Φ is the asymmetric and symmetric parts of the dimensionless velocity gradient, and $\| \cdot \|$ stands for the matrix norm (Hunt et al., 1988).

4. Averaged output power \bar{P}_{out} and consumed power \bar{P}_c . As the self-propelled pufferfish mainly moves along X axis, the output power P_{out} is considered as the product of the propulsive force F_p and the induced velocity U for quasi-steady swimming as follows:

$$P_{out} = F_p \cdot U \quad (3.41)$$

As the deformation of fish body is not considered in the present work, the consumed power P_c is defined in Eq. (3.42) as the summation of the required power that dorsal, anal and caudal fins contribute to the fish self-propulsion.

$$P_c = \sum (\bar{\tau} \cdot \dot{\bar{\phi}}) \quad (3.42)$$

For each fin, its required power is defined by the multiplication of torque $\bar{\tau}$ and the angular velocity $\dot{\bar{\phi}}$. Torque τ is obtained by integrating the moment of pressure force along the fin rotation axis over each fin surface. For rigid fins cases, the angular velocity $\dot{\phi}$ on each hinge is used, while for flexible fins, an averaged angular velocity $\dot{\phi}$ along seven fin rays is adopted due to the variations of undulating amplitude for each fin ray. These seven fin rays include the leading, trailing fin ray and five other fin rays evenly distributed along the fin tips. In their experiment, Li et al. (2018) tracked these seven fin rays to obtain the kinematic motion of one fin surface through an interpolation methodology described briefly in Figure 3.8.

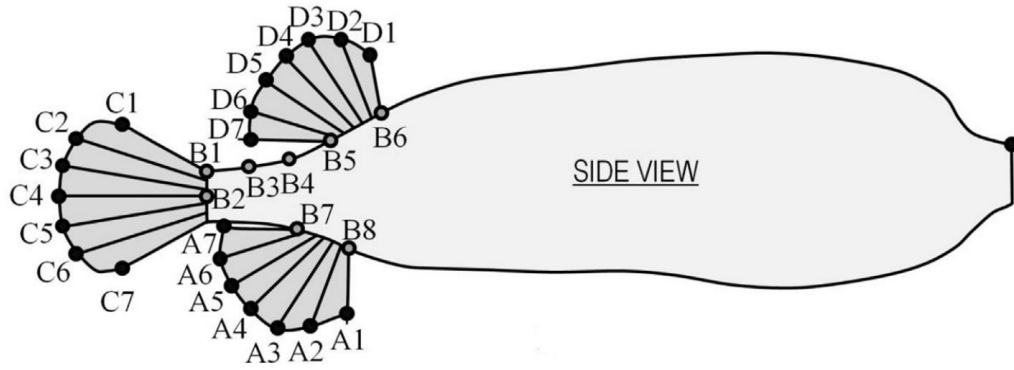


Figure 3.8 Selected fin rays for dorsal (shown as D), anal (A) and caudal (C) fins used to track motion in the experiment (Li et al., 2018)

5. Propulsion efficiency η_{eff} . The propulsion efficiency is another vital metric to assess the swimming performance. In the present self-propulsion studies, it is estimated as the time-averaged output power \bar{P}_{out} over the averaged consumed power \bar{P}_c :

$$\eta_{eff} = \frac{\bar{P}_{out}}{\bar{P}_c} \quad (3.43)$$

This definition, also known as the Froude efficiency (Sfakiotakis et al., 1999), has been widely used in a number of previous self-propelled swimmer studies, such as the anguilliform and carangiform fish (Borazjani and Sotiropoulos, 2010), the thunniform fish (Li et al., 2017), as well as some researches on flapping wings (Abbaspour and Ebrahimi, 2015; Zhou et al., 2016).

3.6 Concluding remarks

In this chapter, the various numerical methods based on ANSYS Fluent that are employed in this work are presented. The in-house code based on the MBD theory is discussed in detail. A pufferfish example that is investigated in Chapter 5 and Chapter 6 is also described. The coupling procedure between the fluid solver and the in-house code is given. Primarily, at each time step, the fluid force applied on each

element/body in MBD model is obtained from fluid solver and passed to the in-house code. The overall force on the entire model is summed up from all relevant elements. With the use of Newton's Second Law, the acceleration of the entire dynamic model is determined. By integrating acceleration once and twice with time, the velocity and location relative to global coordinate is obtained. The above process always starts with a specified reference body B_0 , and then passes on to each element along different branches based on an Euler transformation matrix and constraints on the joints.

With the implemented features, the present CFD-MBD tool is capable of numerically simulating and analysing various problems in the field of aquatic animal swimming, including:

- Discrete and continuous undulating fish swimming
- Peduncle-caudal model modelling
- Passive flapping wing
- Self-propelled pufferfish swimming propelled by multiple fins

Chapter 4 Four Kinds of Aquatic Biomimetic Problems

In this chapter, the Multi-Body Dynamics algorithm developed in this work will be validated with a series of aquatic biomimetic cases. As there are two types of input methods for joints, these cases will be organised into two categories, i.e., the actuated input method and the passive input method. For the actuated input method, three cases with different configurations are studied. For the passive input method, a flapping wing problem will be investigated. These four cases, in total, will demonstrate the capabilities of the algorithm in coping with complex and diverse problems. It should be mentioned that the independence tests of time step and mesh density for the four cases presented in this chapter have been carried out to minimise numerical uncertainty before making comparisons with published data.

4.1 Actuated joints case studies

For actuated connections between elements in MBD model, prescribed rotational motions should be given on hinges. Different from the original code of Hu (2016), the present code is capable of solving the problem of a continuous fish model. Furthermore, in addition to serial-like models, the code has been extended to deal with more complex tree-like models, in which each element can be either rigid or deformable. Table 4.1 lists the principal differences among the three cases. Detailed problem descriptions and results are given in the following sub-sections.

Table 4.1 Categories of cases with actuated joints

Case No.	Problem type		Dimension	Rigid/Deformable Element in Model	Algorithm Type
4.1.1	Fish body undulation	Discrete model	2D	Rigid	Tree-like
4.1.2		Continuous model	2D	Rigid	Serial-like
4.1.3	Single caudal fin		3D	Rigid+Deformable	Serial-like

4.1.1 Discrete undulating fish

By modelling a fish as several articulated solid bodies, Kanso et al. (2005) firstly analysed its locomotion in ideal fluid. Furthermore, Eldredge (2008) simulated a simplified undulation motion of an anguilliform free-swimming fish with a two-dimensional model made of three identical rigid elements. This can be considered as splitting a continuous eel-like fish body into several separate elements connected by joints. The geometric shape of each element is ellipse, with an aspect ratio for major vs. minor axis of 10. The length of each element is a , and the distance d between each body is $0.2a$. To use the MBD method, the middle body is selected as the reference body B_0 , the other two bodies, numbered as B_1 and B_2 , are treated as two different branches, forming a tree-like model. The local coordinate system for each body is illustrated in Figure 4.1.

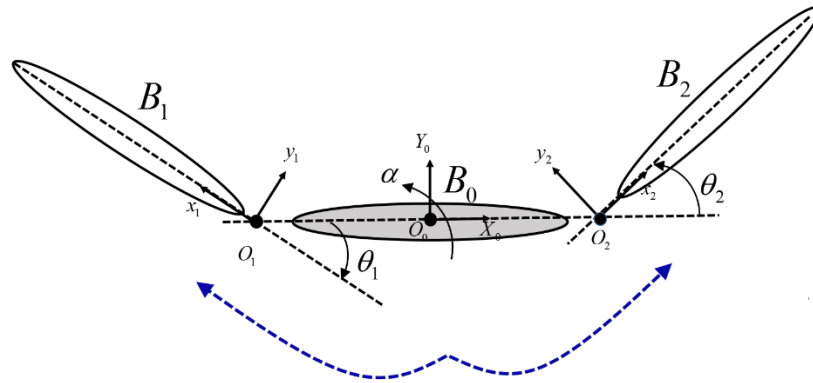


Figure 4.1 Sketch of coordinate setting for the discrete fish body model

In order to obtain comparable results with the previous study, the rotational angular motions (θ_1 and θ_2) are specified between two adjacent bodies (B_0 and B_1 , B_0 and B_2) as:

$$\begin{aligned}\theta_1(t) &= \cos\left(t - \frac{\pi}{2}\right) \\ \theta_2(t) &= -\cos(t)\end{aligned}\tag{4.1}$$

An undulation Reynolds number defined in Eldredge (2008) is used in the present study and it is equal to 200 via the following equation:

$$\text{Re} = \frac{\dot{\theta}_{\max} a^2}{\nu} \quad (4.2)$$

where $\dot{\theta}_{\max}$ is the maximum angular velocity, a is the length of each ellipse, and ν is the kinematic viscosity of water.

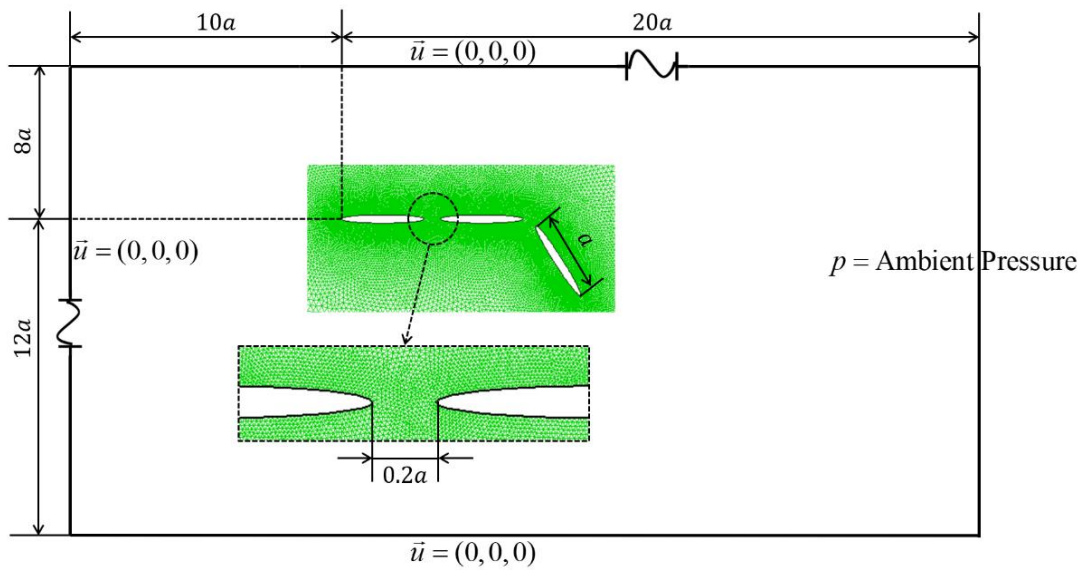
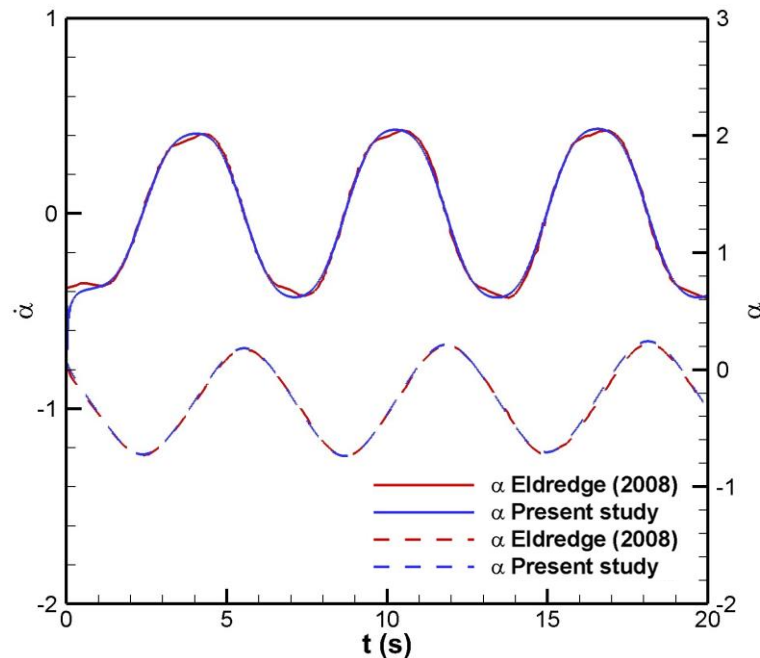


Figure 4.2 Computational domain of discrete fish body simulation

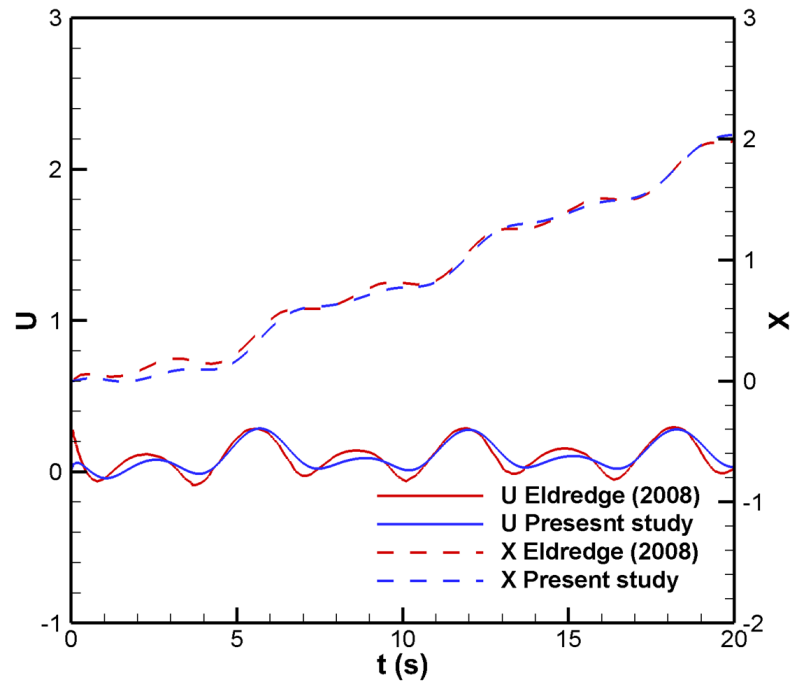
The computation is performed in a domain with a size of $30a \times 20a$, shown in Figure 4.2, which is large enough to avoid the boundary influence. The model is placed $10a$ and $8a$ away from the inlet and upper boundaries, respectively. Around the model, a small inner zone is designed for mesh refinement to better capture the vortex structure around the swimming body. Unstructured triangular meshes are applied to the whole computational domain and the overall grid number is around 141,000. At the surface of the three elements, no slip boundary conditions are imposed. A constant velocity ($\vec{u} = (0, 0, 0)$) are set to the left, upper and lower boundaries and the pressure at the

right boundary is set to ambient pressure. Time step is set as $\Delta t = \frac{T}{500}$ after testing, where $T = 2\pi$ is the undulating period.

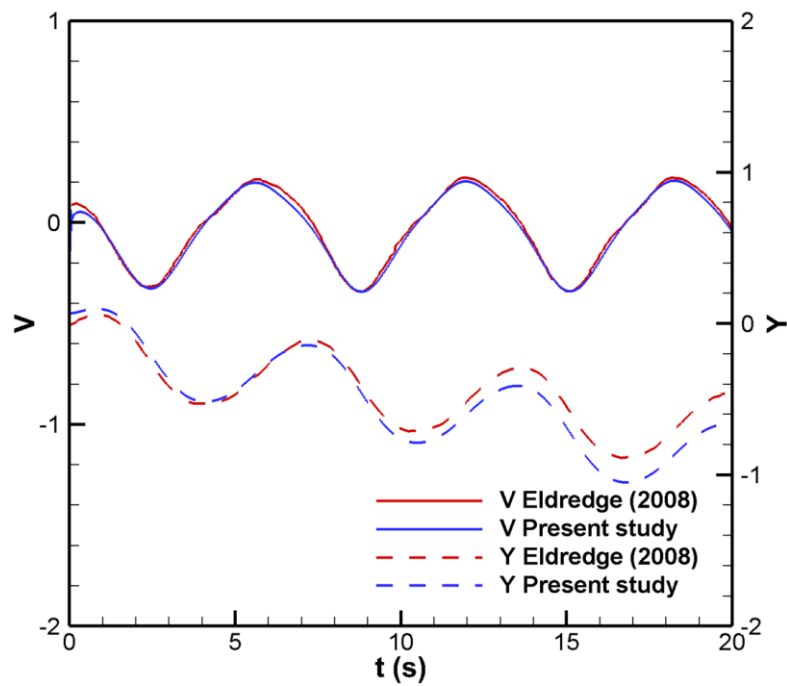
Detailed comparison of results between the present study and Eldredge (2008) is given in Figure 4.3, in terms of the induced rotational angle α , the angular velocity $\dot{\alpha}$, the velocity and displacement in X and Y direction at the central point O_0 of body B_0 , normalized either by the body length a or velocity $\dot{\theta}_{\max} a$. It should be noted that, the whole numerical model is free in X and Y directions, while a rotational motion is possible for the central element. The induced velocity is periodic for both rotational ($\dot{\alpha}$) and translational (U and V) motion. The mean linear velocity is positive for U and negative for V, and hence the undulating fish moves towards the positive X and negative Y direction. Meanwhile, the displacement in the Y direction is smaller and oscillates more than that in the X direction. For rotational motion, the rotational angle α varies approximately from -0.8 rad to 0.2 rad.



(a) Rotational motion



(b) X direction



(c) Y direction

Figure 4.3 Velocity and Displacement comparisons between Eldredge (2008) and present study on the rotational motion, X and Y direction of the reference body

Figure 4.4 compares the vorticity field at five instantaneous time. The foremost element generates a vortex, which moves backward from the two sides and merges with the boundary layer. The vortex sheds off at the tip of body B_1 and obvious vortex street can be observed in the downstream of the model. Overall good agreement with the previous study by Eldredge (2008) is clearly demonstrated.

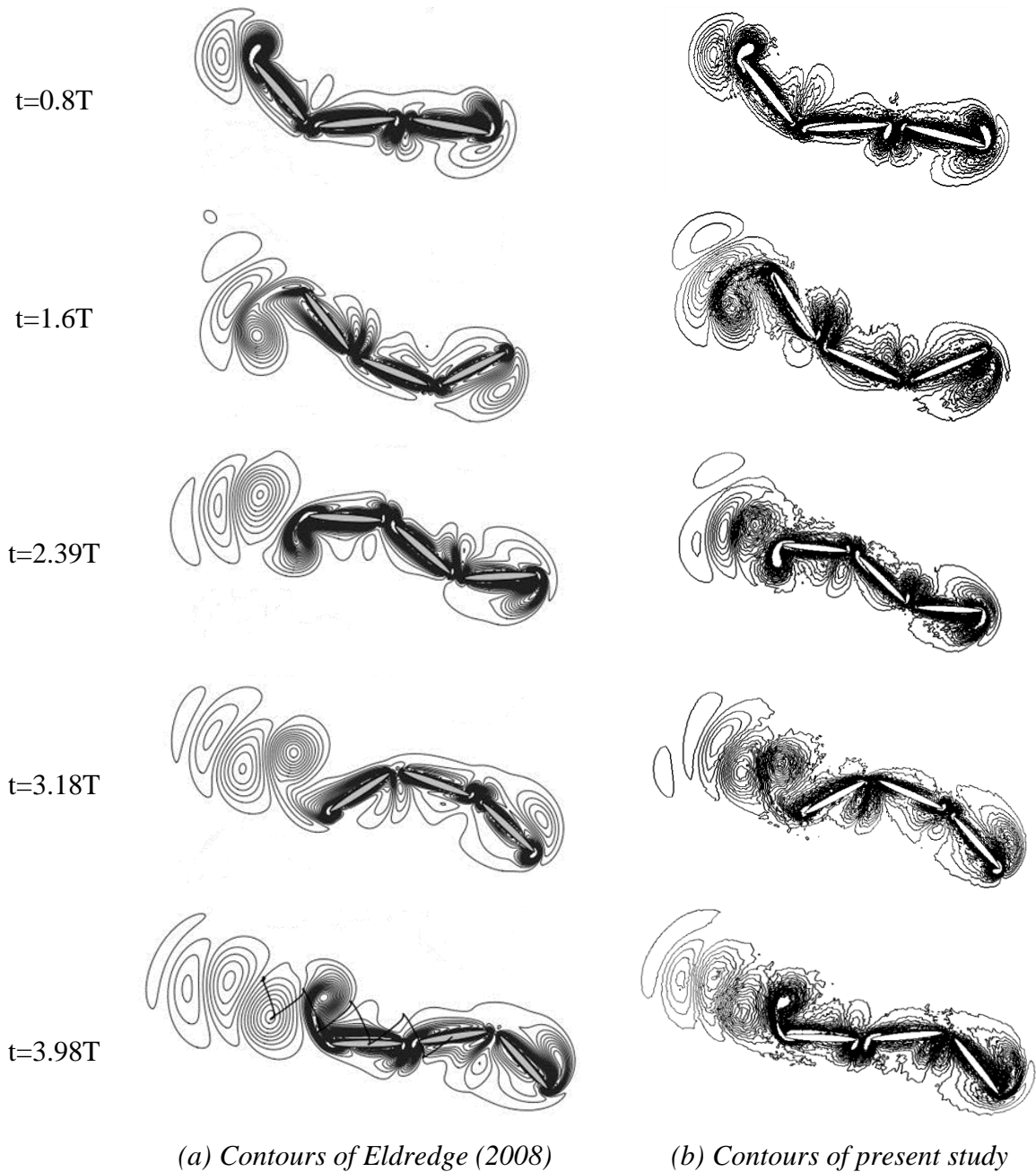


Figure 4.4 Vorticity structure comparisons with the values from -5 to 5 in 40 levels

The successful validation of this MBD applied to this discrete model is vital in the bio-inspired robot area, as most of anguilliform robot fish are made of a series of modules with motion control actuators placed between two adjacent modules like AmphiBot III (Porez et al., 2014b).

4.1.2 Continuous Anguilliform fish undulation

To demonstrate that the established MBD is also applicable to modelling a continuous body locomotion like an anguilliform mode, a two-dimensional self-propelled eel-like fish model is selected in this section, which is taken from Carling et al. (1998).

The model is constructed using eight trapezoidal bodies, as shown in Figure 4.5. The length Δs of each body at initial time is identical. Based on the geometry provided by Carling et al. (1998), the total fish length l is 0.08m. The width of the whole model is defined as:

$$w_n = 0.0064 - 0.0048(3 - 2s_n / l) s_n^2 / l^2 \quad (4.3)$$

where s_n stands for the distance from the fish head to the current hinge location (n th). The widest length of the model w is at fish head with a value of 0.0064m.

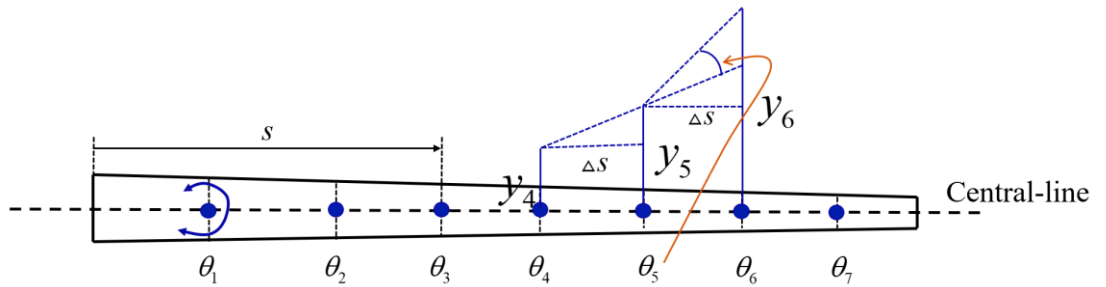


Figure 4.5 Anguilliform fish model

At the onset, there is no bending of the fish body, thus its central line is a straight line. Previous studies prescribed a kinematic undulating motion to the central line to drive

the fish to move forward. The vertical linear motion of the central line was described as:

$$y_n = \frac{s_n/l + 0.25}{1.25} \sin[(s_n/l - t) \cdot 2\pi/T] \quad (4.4)$$

where y_n stands for the vertical movement of the central line at the location s_n (Carling et al., 1998). Simulation is carried out at a specific period T of 1.2s.

To use the present MBD algorithm, the central line motion is converted to a series of angular motions imposed at each virtual hinge. The angular motion on hinge n is determined by three successive vertical movement y_{n+1} , y_n and y_{n-1} at the location of s_{n+1} , s_n and s_{n-1} , respectively, which is indicated in Figure 4.5 and described by the following equation:

$$\theta_n = \arctan \frac{y_{n+1} - y_n}{\Delta s} - \arctan \frac{y_n - y_{n-1}}{\Delta s} \quad (4.5)$$

The variable θ_n is the angular motion on the n th hinge and is given as a known variable into the MBD algorithm. A transition function β , as shown in Equation (4.6), is utilised in the first undulation period to ensure the angle increases gradually such that no break-down of the iteration could occur due to a dramatic change of angle. Figure 4.6 displays the prescribed angular motion profiles θ_n at all seven hinges within the first cycle - a transition cycle, as discussed above.

$$\theta_n = \beta \hat{\theta}_n$$

$$\beta = \begin{cases} \frac{1 - \cos(\pi t / 1.2)}{2} & 0 \leq t \leq 1.2s \\ 1 & t > 1.2s \end{cases} \quad (4.6)$$

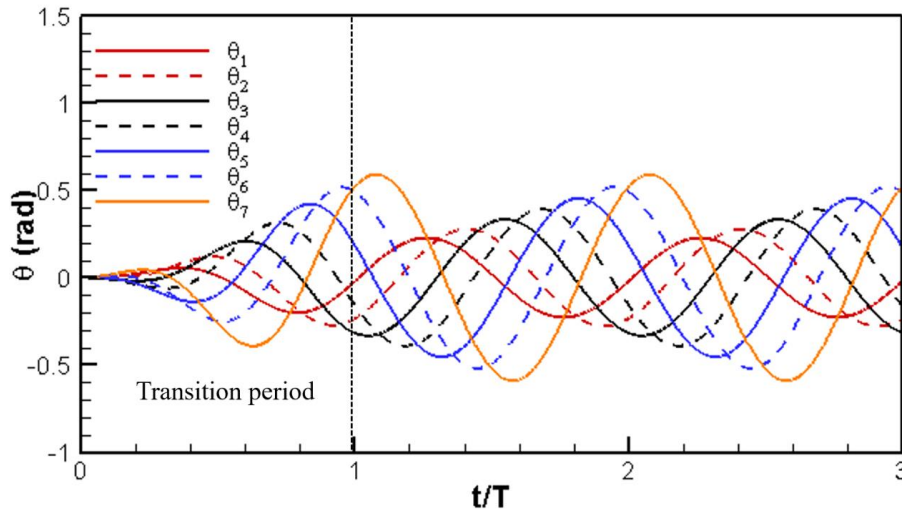


Figure 4.6 Prescribed angular motion on hinges of anguilliform fish

The simulation is carried out in a domain as presented in Figure 4.7. The model is placed $5l$ away from the outlet boundary. The whole domain is split into inner and outer zones to ensure good mesh quality around the model. No slip boundary is set on the surface of the fish. The pressure at the downstream boundary is given as ambient pressure. The other three boundaries are set as constant velocity ($\vec{u} = (0, 0, 0)$). The mesh in the entire domain is triangular mesh. A time step of $\Delta t = \frac{T}{300}$ is selected for the simulation.

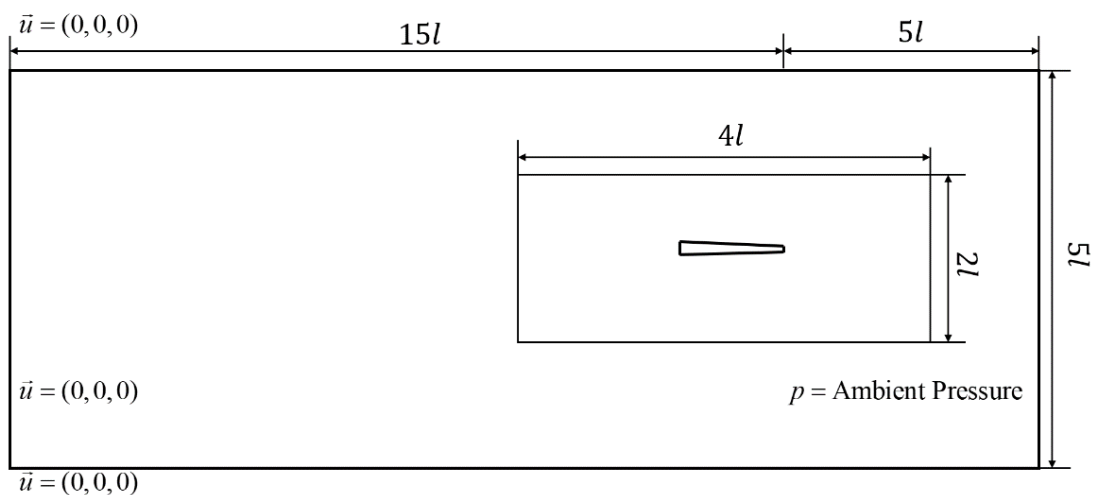


Figure 4.7 Computational domain of anguilliform fish

Figure 4.8 shows the forward and lateral velocity comparisons with Carling et al. (1998). It is clear that the obtained results using present MBD method compare well with the previous study. As the first undulating period is taken as a transition stage, only the body shape is modified. Thus, the FSI induced forward velocity remains zero and there is no translational motion for the fish. From the second period onwards, the fish begins to accelerate and then reaches a quasi-stable status.

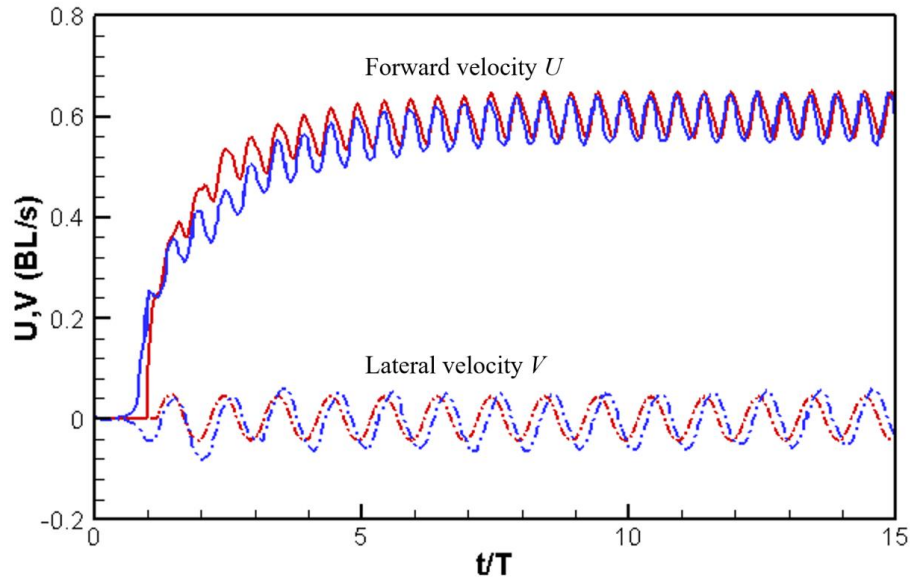


Figure 4.8 Time history of forward and lateral velocity (Blue lines: results of Carling et al. (1998); red lines: present results)

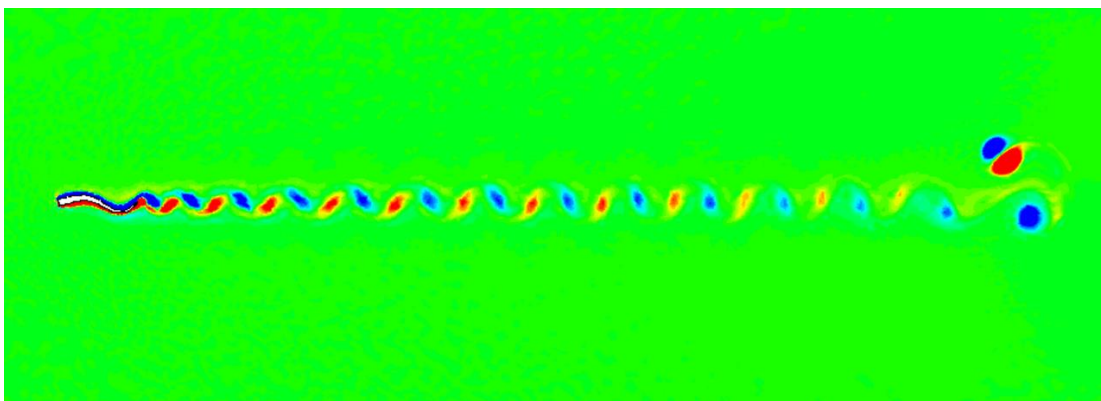


Figure 4.9 Vorticity contour for 15 undulating periods (z vorticity with the values from -3 to 3 in 20 intervals)

The vorticity field of the fish swimming within 15 undulating periods is plotted in Figure 4.9 with the existence of a typical reversed Karman Vortex structure. In one undulating period, the beating amplitude of the fish tail has two peaks indicating that vortex is shed twice in one period.

The good agreement shown above between present numerical results and those by Carling et al. (1998) provides evidence that the developed tool offers a new means to address a continuous fish body undulation via splitting a deformable body into multiple rigid elements.

4.1.3 Fish Peduncle-Caudal Cupping Motion

A series of experimental work has been performed (Hu et al., 2016; Ren et al., 2016a; Ren et al., 2016b) to study the hydrodynamic characteristics of a robotic caudal fin to mimic the homocercal tail of the Bluegill Sunfish. Motions of both peduncle and caudal fin were replicated via a properly designed robotic model as shown in Figure 4.10.

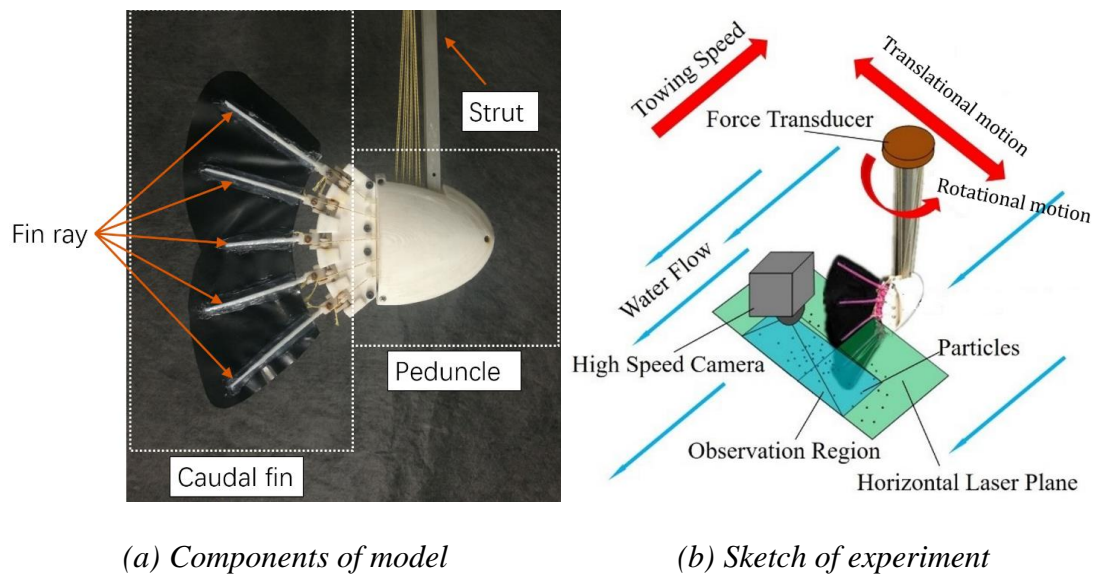


Figure 4.10 Experimental model of fish peduncle-caudal (Hu et al., 2016)

The peduncle is connected to a strut, which allows translational and rotational motions. An experiment (Hu et al., 2016) was carried out in a small water tunnel using a constant towing speed u . The cupping motion of a passively deformable caudal fin was achieved via fabricating the fin surface using a black silicone membrane and prescribing the motion of each fin ray.

Based on the experimental model, the CFD model is constructed and displayed in Figure 4.11(a). The caudal fin is modelled as an axisymmetric shape with its thickness omitted. The geometry is defined by providing the chord lengths at four angles (7.5° , 17.5° , 27.5° and 37.5°) as shown in Figure 4.11(b). The caudal peduncle is modelled as a wedged body with its three dimensions ($L \times W \times H$) indicated in Figure 4.11(c) and (d).

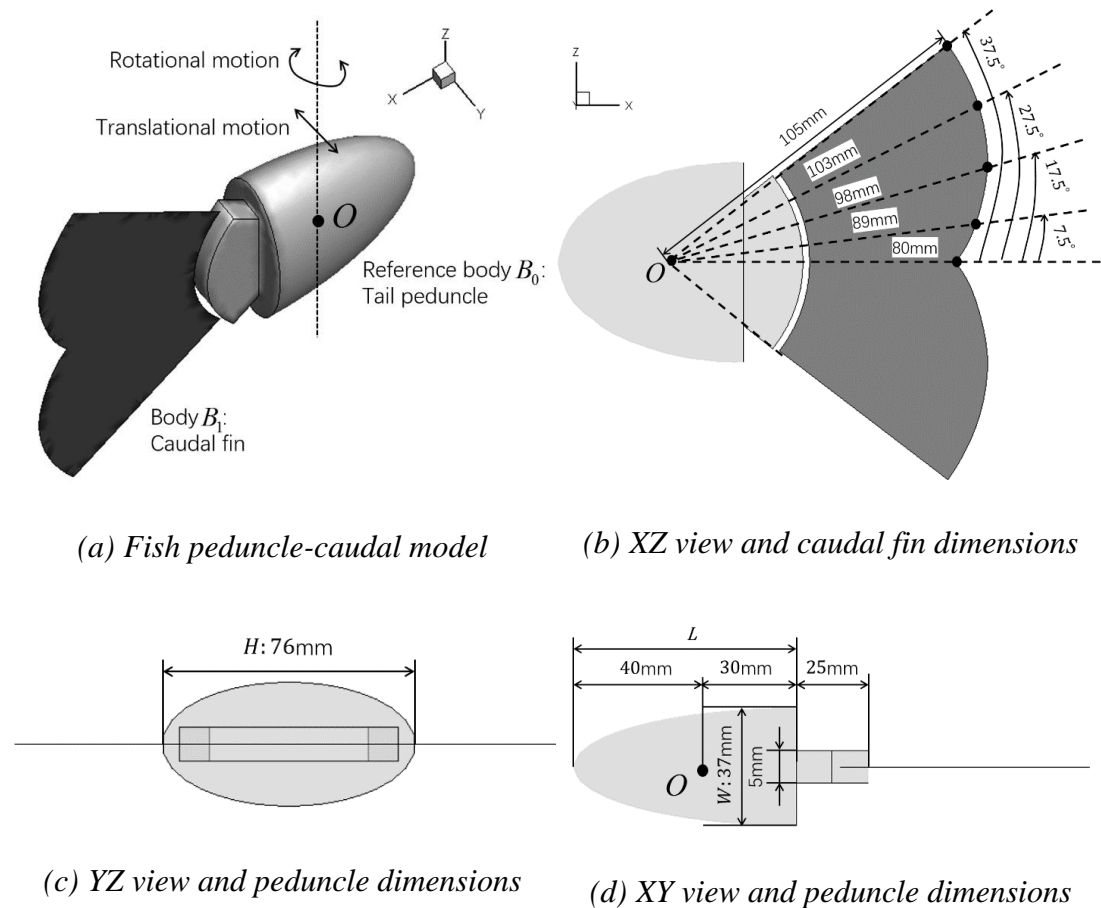


Figure 4.11 Fish peduncle-caudal CFD model and dimensions

The computational domain, as shown in Figure 4.12, is large enough to minimise the influence of the outer boundaries. The model was placed $4L$ away from the inlet boundary. Two mesh zones are generated with an inner zone having unstructured tetrahedral elements and an outer zone with structured hexahedral mesh. The total mesh number is approximately 430,000 and the unsteady time step is selected as 500 steps per time period. The inlet boundary is given as a constant velocity, equal to the towing speed during the experiment, which is determined by the Strouhal number, and defined as:

$$St = \frac{f \cdot A}{u} \quad (4.7)$$

where f , A and u is the frequency, translational motion amplitude and the inlet velocity, respectively. The pressure at the right boundary is set to ambient pressure and the surrounding boundary is symmetry. The surface of the peduncle-caudal model is treated as a no slip boundary.

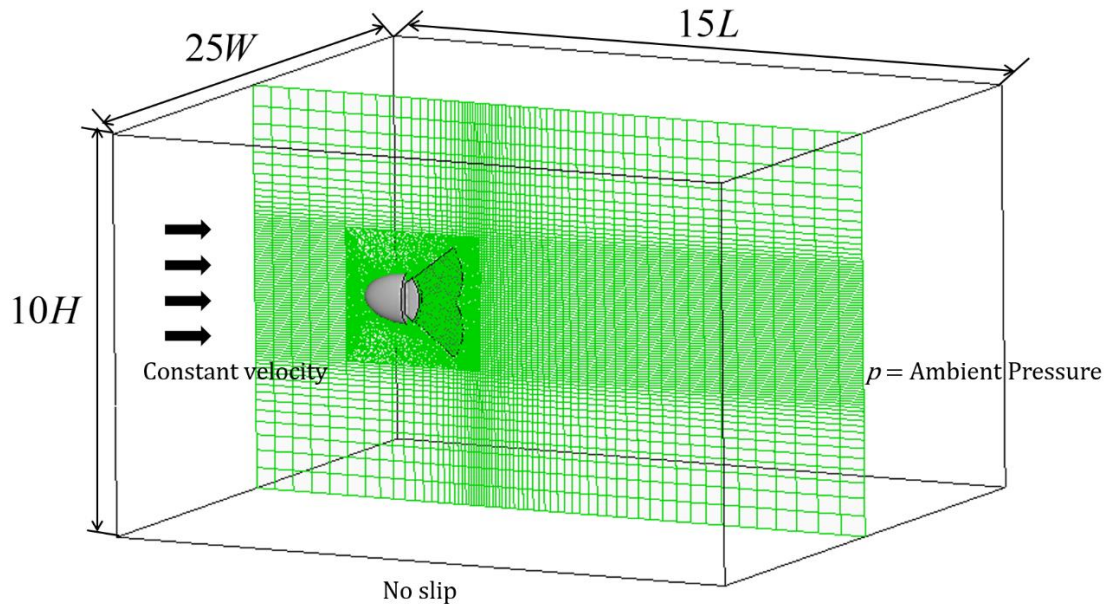


Figure 4.12 Sketch of fish peduncle-caudal computational domain

In accordance with the Multi-Body Dynamics algorithm, the present model is considered as a two-element system, i.e., the caudal peduncle (set as the rigid reference body B_0) and the deformable caudal fin (B_1). The caudal fin is connected to the peduncle by a virtual hinge with no rotational motion allowed. Referring to the experiment, the rotational and translational motions are provided on B_0 , as defined in the following equations:

$$\begin{aligned} \text{Translational } S_T &= 0.02 \sin(2\pi t) \\ \text{Rotational } A_R &= 0.2618 \sin(2\pi t - \frac{\pi}{2}) \end{aligned} \quad (4.8)$$

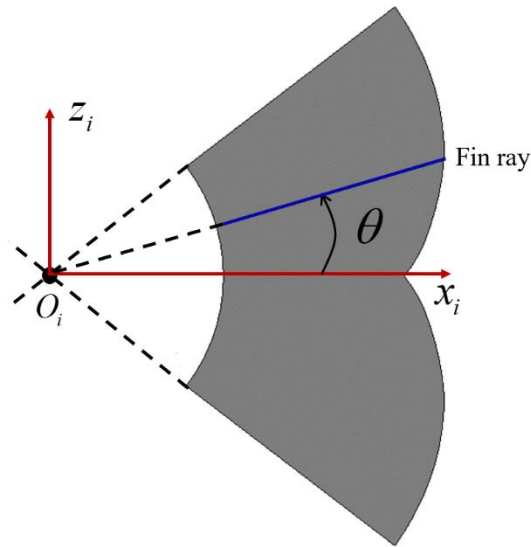


Figure 4.13 Definition of θ for peduncle-caudal model

The cupping motion of the deformable caudal fin can be treated as successive fin rays with different undulating amplitudes, given as:

$$\varphi = A(\theta) \sin(2\pi t) \quad (4.9)$$

where θ is the angle between each fin ray (blue line in Figure 4.13) and the x axis relative to its local coordinate (red line in Figure 4.13); $A(\theta)$ is the amplitude of each undulating fin ray, described as:

$$A(\theta) = a_1 - a_2\theta + a_3\theta^2 \quad (4.10)$$

Detailed values of the parameters used in Equation (4.10) are given in Table 4.2 taken from Hu et al. (2016).

Table 4.2 Motion parameters for peduncle-caudal model

a_1	a_2	a_3
16	0.4677	0.0068

Simulations are performed for four Strouhal numbers. Figure 4.14 compares the time averaged thrust between the experiment and CFD modelling at four St , where the thrust is defined as the total force acting on the peduncle and caudal fin in x direction:

$$F_{\text{thrust}} = F_{\text{peduncle}} + F_{\text{caudal}} \quad (4.11)$$

As can be seen from Figure 4.14, the predicted results are consistent with the experiment. Within the St range tested, thrust increases along with St . It should be noted that some subtle differences can be observed between experiment and the CFD at $St = 0.2, 0.5$. This might be caused by the caudal fin edge effect since it has a passive motion in the experiment, while in the CFD modelling the whole surface of the caudal fin is given a prescribed deformation extracted from experimental data.

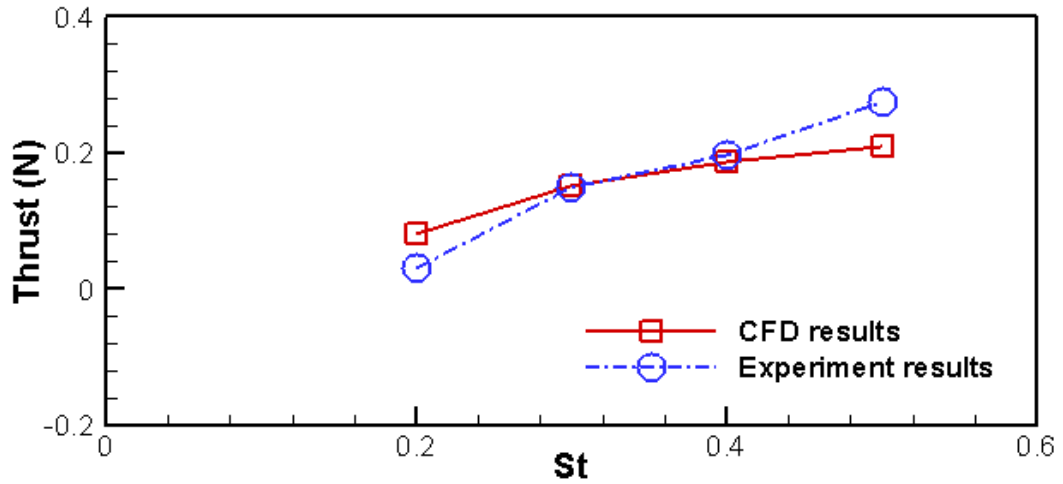


Figure 4.14 Thrust comparisons between CFD results and experiment results (Hu et al., 2016)

A variation of time-dependent force is displayed in Figure 4.15 at $St=0.3$ for five time periods. Negative values stand for resistance while positive values reflect propulsion force. Clearly, as indicated by their signs, peduncle always suffers the resistance, possibly due to its blunt shape, while the deformable caudal fin generates propulsion force.

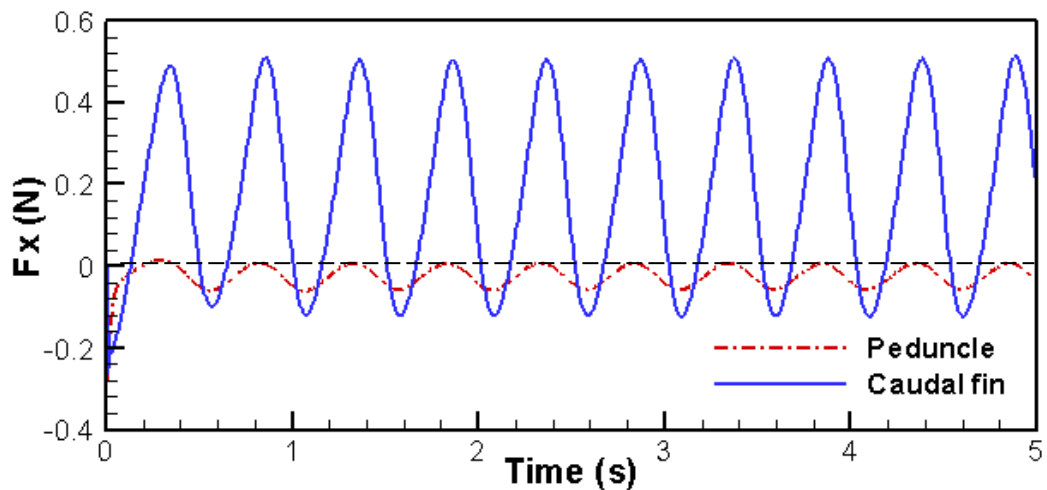


Figure 4.15 Forces on peduncle and caudal fin in x direction at $St=0.3$

The flow visualization on the instantaneous vortex topology in one time period at $St=0.3$ is shown in Figure 4.16 from two planes. The vortices shed from caudal fin generate a chain of vortex rings convected into downstream and the vortex rings are linked, which agrees with the findings of Lauder and Drucker (2002).

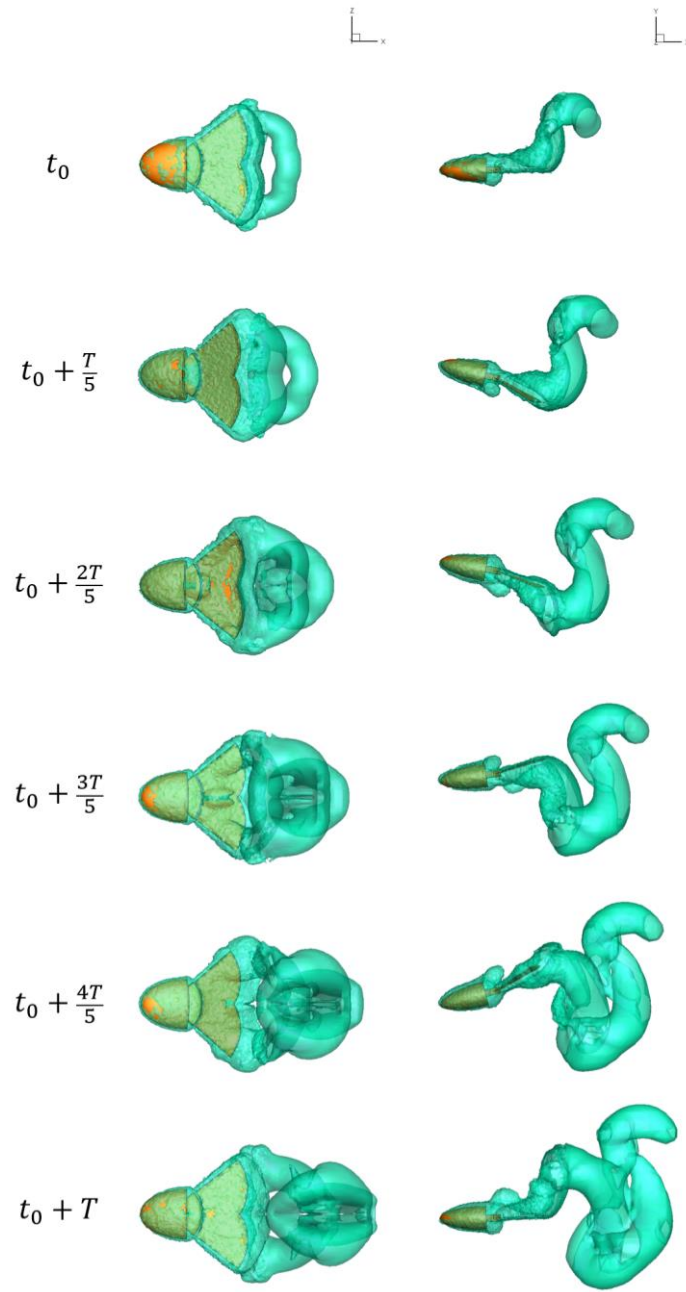


Figure 4.16 Vortex topology (vorticity magnitude with values from 0 to 15 in 16 levels) for peduncle-caudal model at $St=0.3$ in one period from XZ and XY view

The quantitative comparison between the CFD prediction and experimental data further demonstrates that the present MBD model can deal with a complicated swimming locomotion, including both rotational translational motions of a caudal peduncle and undulation of flexible fin rays.

4.2 Passive connection case study

In order to validate the passive connection condition, a passive flapping wing model previously simulated by Toomey and Eldredge (2008), as shown in Figure 4.17, is studied in this section. The model is composed of two identical rigid ellipses, which are named as the driven element/component (set as reference body B_0) and the passive element/component (body B_1), separately. The whole simulation is carried out in water.

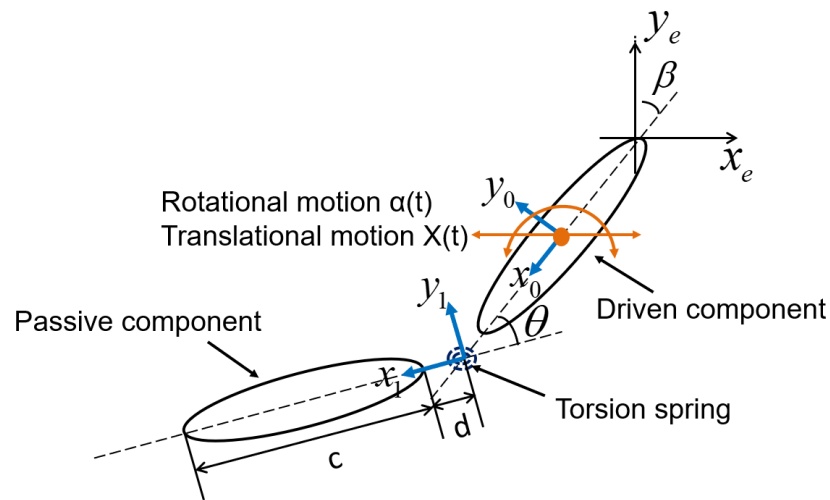
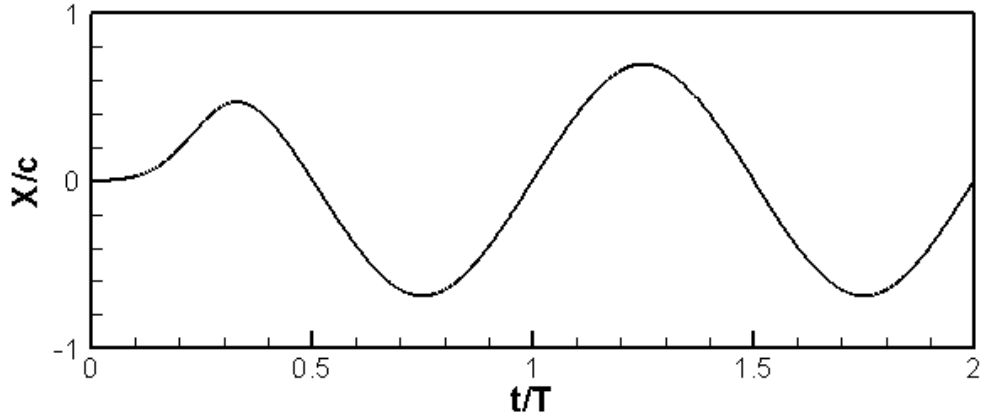


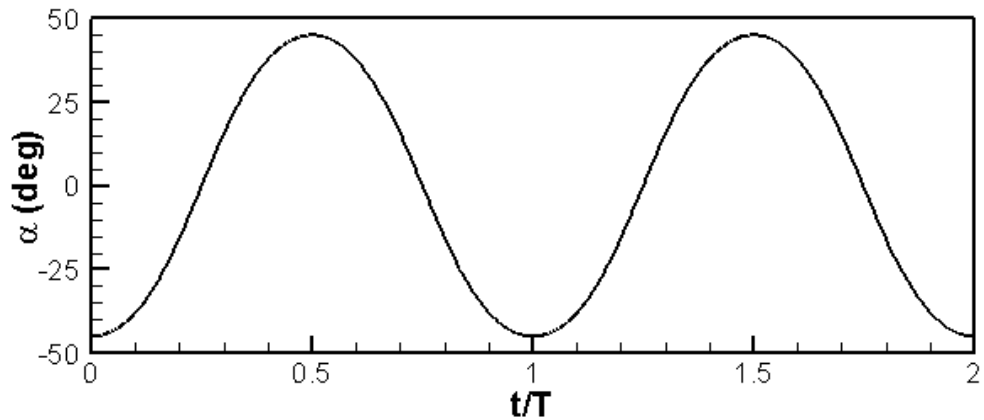
Figure 4.17 Sketch of the passive flapping wing model

The length of each element c is 0.051m and the aspect ratio between the length and width is 5. The gap d between each element and a virtual connecting joint is 0.0025m. The density of the model is $5080 \text{ kg} / \text{m}^3$. The initial status of the whole model is that the two elements are placed in a line and the reference body B_0 has a sweep angle β

defined in the earth coordinate. The origin of the local coordinate for B_0 and B_1 is set to the mass centre and the connection joint, respectively, as shown in Figure 4.17.



(a) Translational motion $X(t)$



(b) Rotational motion $\alpha(t)$

Figure 4.18 Prescribed motions on reference body

Translational $X(t)$ and rotational $\alpha(t)$ motions are prescribed to the centre of reference body. The time series of $X(t)$ normalised by the element length c and $\alpha(t)$ within the first two periods are plotted in Figure 4.18. Their mathematics expressions used in the present study are identical to the ones given by Toomey and Eldredge (2008) as:

$$X(t) = \frac{A G_t(t)}{2 G_{t,\max}} C(t) \quad (4.12)$$

$$\alpha(t) = -\beta \frac{G_r(t)}{G_{r,\max}}$$

where t is time, G_t and G_r are the translational and rotational shape functions:

$$G_t(t) = \int_t \tanh[\sigma_t \cos(2\pi ft)] dt \quad (4.13)$$

$$G_r(t) = \tanh[\sigma_r \cos(2\pi ft)]$$

and $C(t)$ is a start-up conditioner for translational kinematics as:

$$C(t) = \frac{\tanh(8ft - 2) + \tanh 2}{1 + \tanh 2} \quad (4.14)$$

The definitions and values for the parameters used in equations (4.12) and (4.13) are given in Table 4.3.

Table 4.3 Parameters used in the passive flapping wing model

Notation	Unit	Definition	value
β	rad	Sweep angle	$\frac{\pi}{4}$
A	m	Translational amplitude	0.071
$G_{r,\max}$	-	Maximum value of rotational/translational shape function G_r / G_t in one motion cycle	0.5567
$G_{t,\max}$	-		0.6178
σ_r	-	Rotational/translational shape parameter	0.628
σ_t	-		0.628
f	Hz	Oscillating frequency of the driven element	0.15

The passive joint can be considered as a linear spring-damper model and the included angle θ between the passive element and the driven element is fully induced by a virtual torsional spring-damper. The torque provided by the spring-damper can be described as:

$$\tau = -R\dot{\theta} - K\theta \quad (4.15)$$

where $\dot{\theta}$ is the velocity of the included angle, K and R are the spring stiffness (equal to $0.068 \text{ kg} \cdot \text{m}^2 / \text{s}^2$) and damping coefficient (equal to $0.0039 \text{ kg} \cdot \text{m}^2 / \text{s}$)

A rotation Reynolds number is defined in the work of Toomey and Eldredge (2008) as the following:

$$\text{Re}_r = \frac{2\pi\beta\sigma_r f c^2 / \tanh \sigma_r}{\nu} \quad (4.16)$$

where ν is the kinematic viscosity of water. Re_r in the present study is equal to 100.

The size of the computational domain is $20c \times 30c$, and the virtual joint in the middle of the model is placed at the centre of the domain, as shown in Figure 4.19. The whole domain is split into a central circular inner zone with a radius of $5c$ and an outer zone. Compared with the outer zone, finer mesh is generated within the inner zone so that the vortices generated by the model can be better captured. The outer boundaries are far enough to avoid boundary influences. Unstructured triangular meshes are generated in the whole domain and the total mesh number is about 23,000. The dynamic mesh functionality is employed to update the computational mesh, with smoothing and remeshing features enabled to ensure good mesh quality. In terms of the boundary condition, the upper, lower and left boundaries are set as constant velocity inlet ($u = 0$), an ambient pressure is applied to the right boundary. The two rigid elements are treated as no slip walls. Time step size is set as $\Delta t = \frac{T}{500}$, with $T = 2\pi f$.

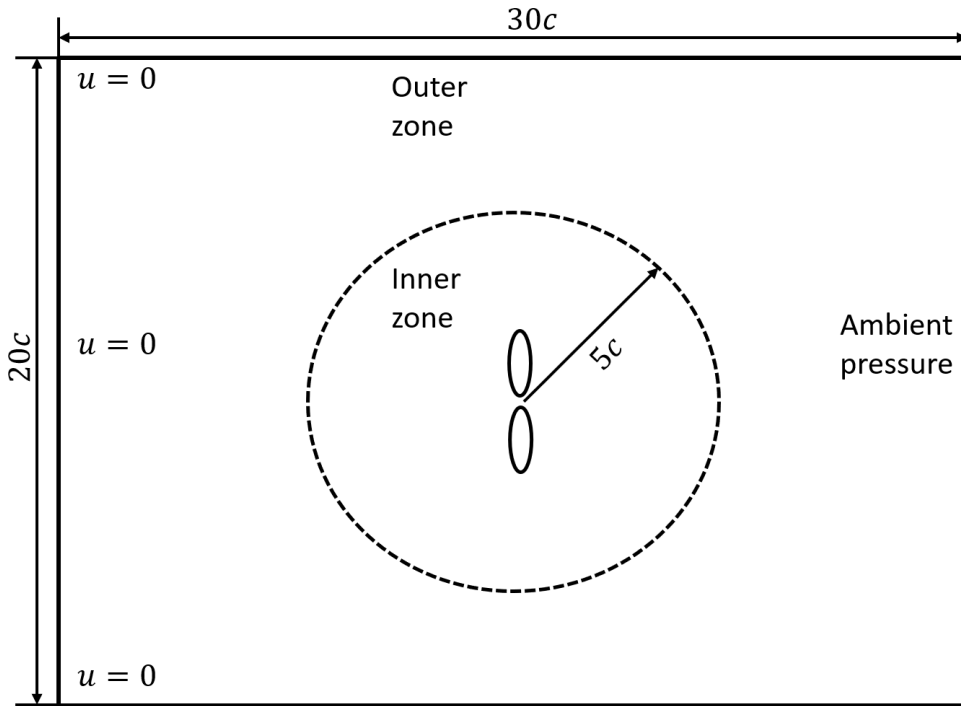


Figure 4.19 Computational domain of the passive flapping wing model

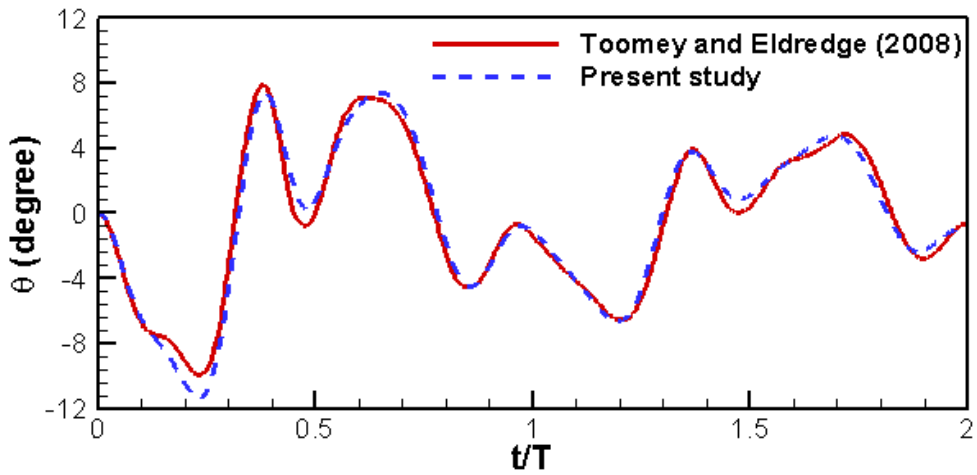


Figure 4.20 Included angle comparison between Toomey and Eldredge (2008) and present study

The induced included angle θ and dimensionless horizontal force C_x predicted by the present study are compared with those from Toomey and Eldredge (2008). Figure 4.20 illustrates the change of induced angle θ in the first two flapping cycles. With the

passive input method in the present MBD algorithm, the result matches well with the previous study. In general, when the prescribed motions are applied to the driven element, the included angle between the passive element the driven element is small, i.e., less than 10 degrees.

The comparisons of dimensionless force C_x in global x direction is presented in Figure 4.21. The dimensionless force C_x is obtained as:

$$C_x = \frac{2F_x}{\rho_f f^2 c^3} \quad (4.17)$$

Here, F_x is fluid force of the whole model in x direction, ρ_f is water density, f is the flapping frequency and c is the length of each element. Again, the present results show good agreement with previous predictions by Toomey and Eldredge (2008).

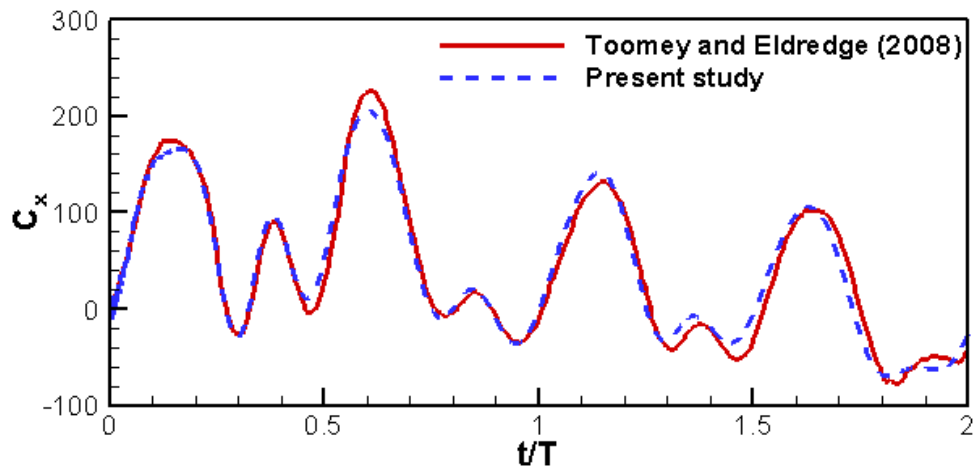
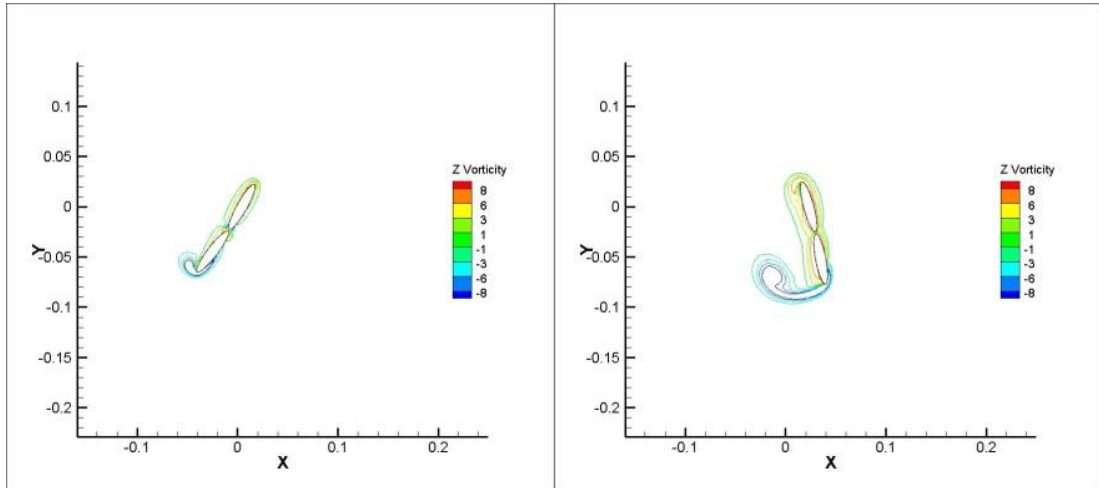
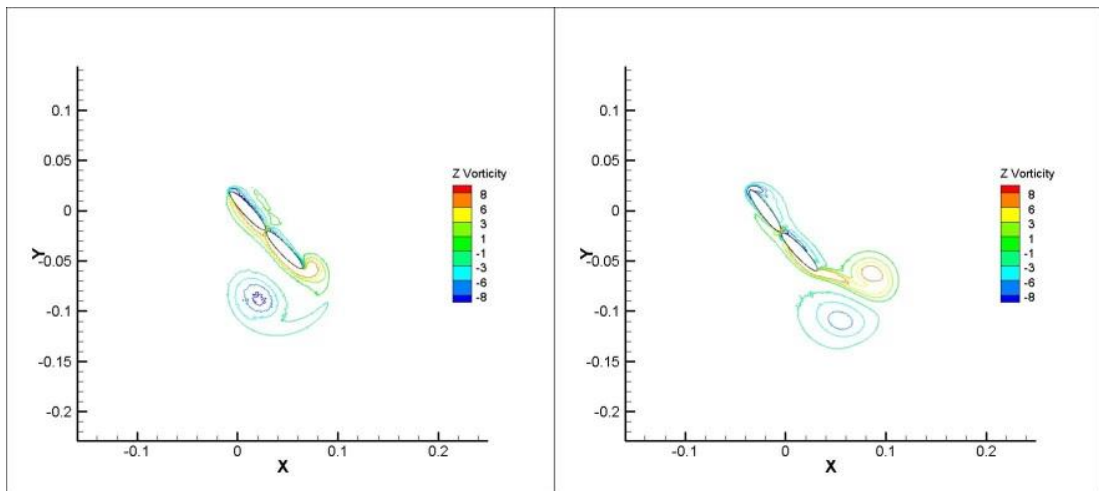


Figure 4.21 Dimensionless force comparisons in x direction

Besides the above comparisons, the development of the vortex field for the flapping wing model at 6 instants within one period is also given in Figure 4.22. It can be seen that, as the driven component flaps from its left most position to the right most position, vortices are generated on both sides of the model and one vortex is shed off the passive

element to the left side of the model in approximately half a period. During the other half of the flapping motion, another vortex is formed at the right side of the model. Finally, at the end of the period, a pair of vortices are produced in the downstream area.

(a) $t=0.15T$ (b) $t=0.3T$ (c) $t=0.45T$ (d) $t=0.60T$

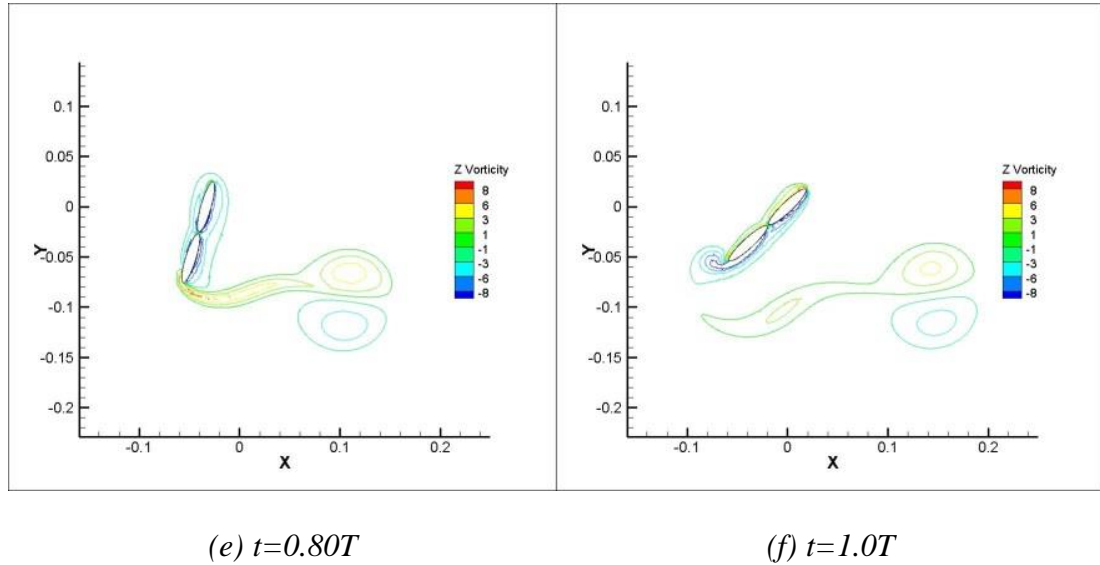


Figure 4.22 Vortex development in one flapping cycle (z vorticity from -8 to 8 with 7 intervals)

4.3 Concluding remarks

In this chapter, four test cases with different computational models and input conditions are set up to validate the various features of the newly developed tool in this project that couples a Multi-Body Dynamic code with a CFD method.

For the case of discrete eel fish with undulating motions presented in Section 4.1.1, three rigid elements are included in the model and two successive elements are connected by a virtual hinge. Prescribed angular motions are given on each hinge. Comparisons of the velocity and displacement on the reference body are presented between a previous study and the present work. Good agreement is achieved, which validates the swimming simulation of discrete models.

In Section 4.1.2, one continuous anguilliform fish model is studied to validate the continuous modelling feature of the tool. A classic analytical model of eel fish is selected and divided into eight virtual elements. Prescribed motion on the midline is transferred into the angular motions on the connected hinges. The lateral and

transitional displacements are compared with the previous results and generally good agreement is achieved.

The hydrodynamic modelling of the connection between deformable and rigid elements is validated in Section 4.1.3 by investigating a deformable caudal fin behind the caudal peduncle. The motion profiles of the caudal fin are provided by a previous experimental study and prescribed on the fin surface. The hydrodynamic force on the fin is firstly predicted to validate the reliability of this method to solve the rigid-deformable connection problem. The hydrodynamic force on the whole model and the vortex structures obtained with present method are then presented to reinforce the experimental study.

Finally, in Section 4.2, the flapping problem of a system that is comprised of two rigid elements connected by a passive torsional spring-damper is investigated. Translational and rotational motions are prescribed to the reference element. The induced included angle between the two elements and the dimensionless force of the whole model in x direction are predicted, which agree very well with the published data from a previous research, further demonstrating the capability of the present coupled tool. The development of the vortex field is also illustrated.

To sum up, for all the four cases with either actuated or passive joints studied in this chapter, good agreement is achieved between the results obtained with the present MBD tool and those from existing studies. The successful validation of the tool proves that it is reliable and can be applied to subsequent investigations.

Chapter 5 Self-Propelled Pufferfish with Multiple Fins

The main objective of this chapter is to analyse the influence of multiple flexible fins on the propulsion performance of a free-swimming fish. A self-propelled pufferfish with dorsal, anal and caudal fins is studied by combining the tree-like MBD algorithm code with 3D numerical approach. Rigid and flexible conditions of fins are considered while the fish body is modelled as rigid. Two kinds of kinematics of fins are investigated, which were obtained from experimental measurement for the incoming current with a velocity of $1BL/s$ and $2BL/s$.

5.1 Problem Descriptions

5.1.1 Kinematics of a Pufferfish Body-Caudal-Dorsal-Anal Model

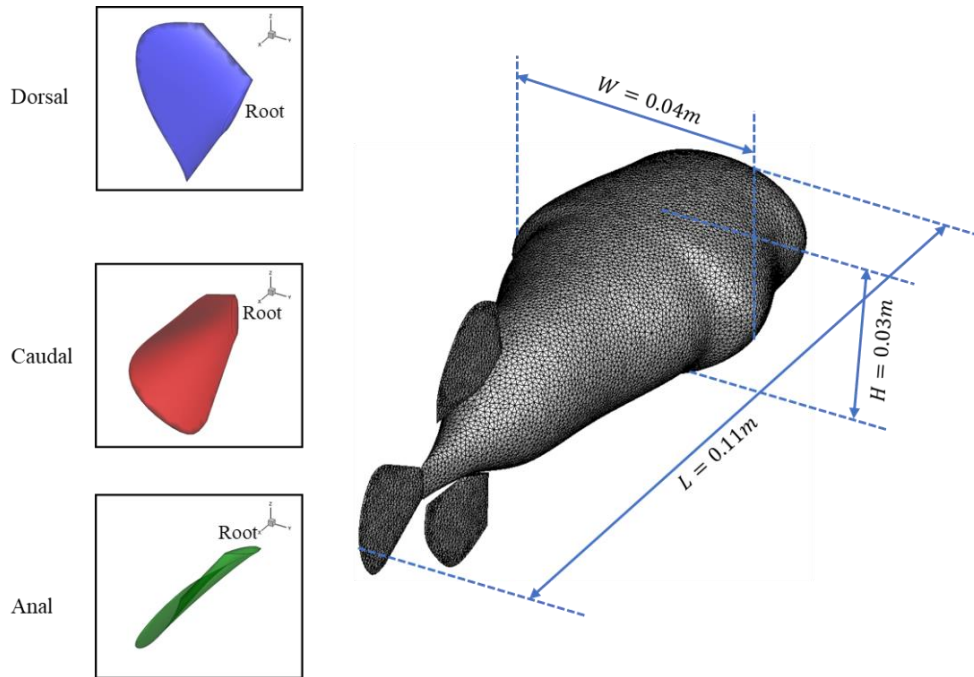
Pufferfish is a typical MPF Tetradontiform swimmer whose pectoral, dorsal anal and caudal fins could mobilise independently (Gordon et al., 1996; Blake and Chan, 2011). Figure 5.1(a) and (b) show a vertical and a side view of the pufferfish measured in the experiment conducted by Li et al. (2018). A 3D fish geometry (Li et al., 2018) was constructed from the experiment and is employed in the present numerical study, as sketched in Figure 5.1(c). The total length (L) of the model is approximately 0.11m. The shape of each cross-section of the body is approximated as an ellipse. The width W and height H of the model are approximately 0.04 and 0.03m, respectively. Each of the three fish fins is modelled as a wedged body surface and its thickness gradually decreases to zero from the root to the edges including tip, leading and trailing fin rays (as shown in Figure 5.2). The live fish experiment was conducted in a circulating water tank with a controllable constant incoming current speed (Li et al., 2018). High-resolution video cameras were used to record the dynamic responses of the fish and the surface motions of its fins. It was found in the experiment that pectoral fins adhered firmly to the main fish body without any oscillations (Li et al., 2018). Therefore, the impact of the pectoral fins on the swimming behaviour is not numerically modelled in this numerical study.



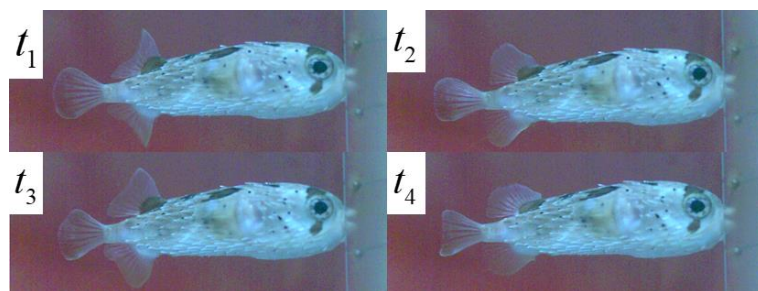
(a) Vertical view



(b) Side view



(c) Dimensions of the fish



(d) Captures of four instantaneous moments in the live fish experiment

Figure 5.1 Live pufferfish in the experiment (Li et al., 2018) and CFD model and sketches for flexible dorsal, caudal and anal fins

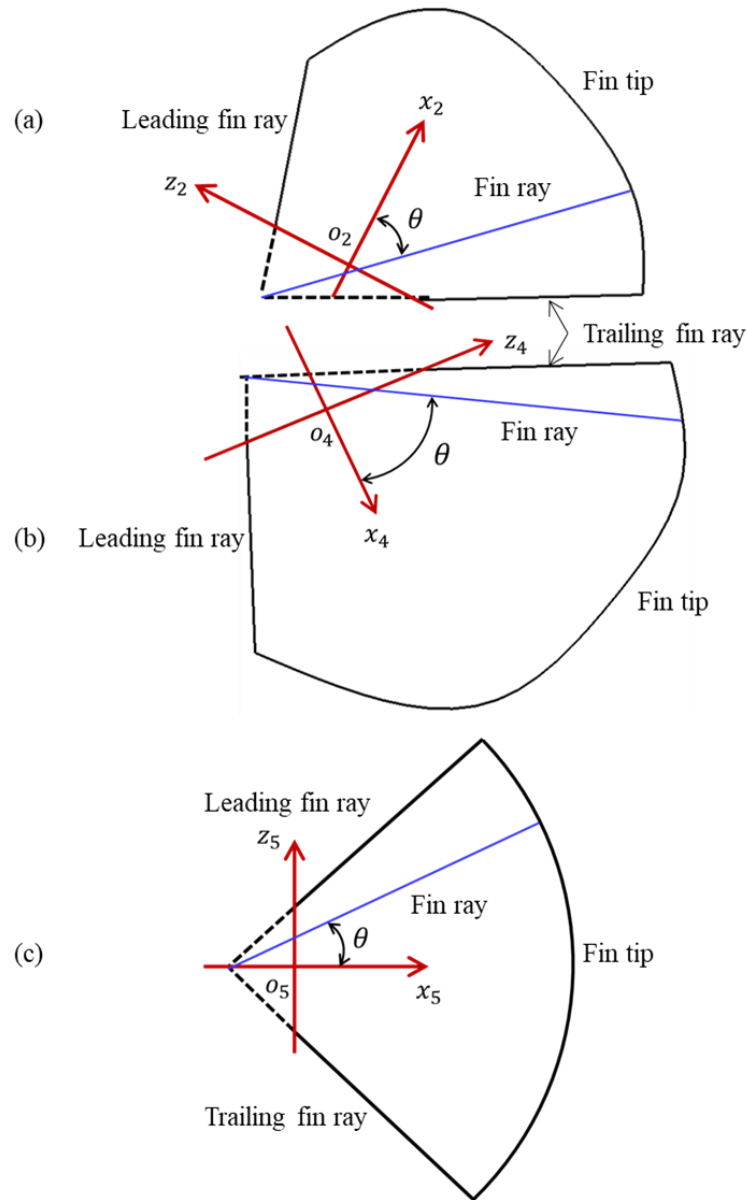


Figure 5.2 Sketches for the definition of θ , leading, trailing fin ray and fin tip for (a) dorsal, (b) anal and (c) caudal fins. Red lines are X and Z axis in the local coordinate for each fin, and blue line stands for a random fin ray.

The fish body is modelled as rigid and pectoral fins are omitted. Figure 5.1(d) displays the experimental captures at four different instantaneous time in one motion cycle, indicating the profound undulating motions of the dorsal, anal and caudal fins. Subsequently, the obtained kinematics of each fin surface is imposed into the CFD model as prescribed fin deformation. In the present work, this condition is defined as

flexible, which is different from the conventionally accepted passively deformed fins. For each fin surface in the experiment, the motions of seven fin rays were tracked as illustrated in Figure 3.8. In the present CFD study, each fin surface could be considered as a series of successive fin rays. Driven by the leading fin ray, a sinusoidal wave travels from the anterior-most edge and spreads down to the rest of the fin surface. By interpolating the motions of those tracked fin rays in the experiment, the motion of the entire fin surface could be approximately obtained and subsequently prescribed in CFD simulations as the flexible condition.

Table 5.1 Parameters in the kinematics equations

Case 1, 2 $\omega = 21.4 \text{ rad/s}$		Amplitude A (rad)			Phase angle ψ (rad)			
		Dorsal	Anal	Caudal		Dorsal	Anal	Caudal
Case 1 (Rigid)		0.94	0.94	0.276		0	0	π
Case 2 (Flexible)	ω_a	-	-	6.601	ω_p	-	-	4.087
	a_I	0.378	-0.184	0.357	p_I	-1.144	-	1.111
	a_{II}	0.699	0.455	0.092	p_{II}	-1.487	-0.31	-0.843
	a_{III}	0.264	-0.237	-	p_{III}	1.452	-1.123	-
	a_{IV}	0.789	0.791	-	p_{IV}	5.151	5.101	-
Case 3, 4 $\omega = 32.8 \text{ rad/s}$		Amplitude A (rad)			Phase angle ψ (rad)			
		Dorsal	Anal	Caudal		Dorsal	Anal	Caudal
Case 3 (Rigid)		1.03	1.03	0.31		0	0	π
Case 4 (Flexible)	ω_a	-	-	6.07	ω_p	-	-	3.48
	a_I	0.135	0.007	0.386	p_I	0.725	0.725	0.725
	a_{II}	0.32	0.32	0.32	p_{II}	0.265	0.265	0.265
	a_{III}	0.356	0.356	-	p_{III}	1.473	1.473	-
	a_{IV}	0.89	0.89	-	p_{IV}	4.106	4.106	-

The kinematics of the flexible fins measured in the experiment under two velocity conditions are tested in this work, i.e., $1BL/s$ and $2BL/s$, where BL is the body length of the pufferfish. Theoretically, the predicted cruising velocity of a self-propelled pufferfish in an initially still water environment should be equal to the incoming current speed specified in the experiment if the kinematic motion profiles of the CFD model extracted from the live fish are imposed to the fins. To analyse the effects of flexible fins in relation to fish propulsion, the rigid fins for the same pufferfish model are also simulated. Table 5.1 summarises the main motion parameters for both rigid and flexible conditions. For the flexible fins, the motion profiles of Case 2 and Case 4 are taken from the experimental data associated with a current velocity of $1BL/s$ and $2BL/s$. Figure 5.3 shows the sketches of the leading, trailing fin rays and fin tips for the dorsal, anal and caudal fins.

The kinematic equation to describe the surface motion of a flexible fin can be expressed as:

$$\varphi(t) = A(\theta) \sin(\omega t + \psi(\theta)) \quad (5.1)$$

where θ is the angle between a fin ray (a blue line in Figure 5.2) and x axis relative to its local coordinate (red lines in Figure 5.2); $A(\theta)$ and $\psi(\theta)$ are the amplitude and phase angle for the fin ray, respectively; ω is the flapping frequency and changes for different cases. By varying $A(\theta)$ and $\psi(\theta)$, the deformation of the flexible fin surface over one motion period is shown in the left column of Figure 5.3. For dorsal and anal fins, the amplitude $A(\theta)$ and phase angle $\psi(\theta)$ can be expressed as:

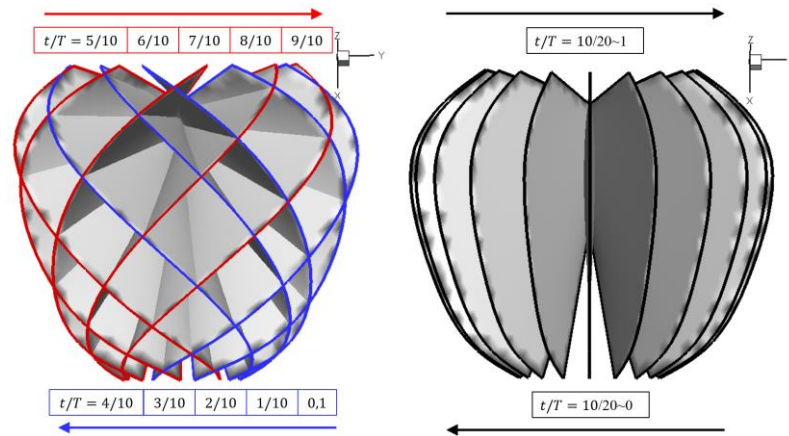
$$\begin{aligned} A(\theta) &= a_I \theta^3 + a_{II} \theta^2 + a_{III} \theta + a_{IV} \\ \psi(\theta) &= p_I \theta^3 + p_{II} \theta^2 + p_{III} \theta + p_{IV} \end{aligned} \quad (5.2)$$

The prescribed motion of a flexible caudal fin surface can be defined as:

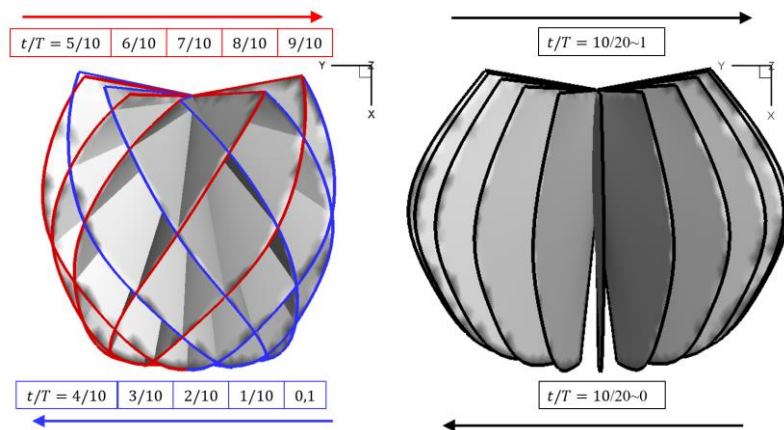
$$\begin{aligned}
 A_c(\theta) &= a_I + a_{II} \cos(\theta\omega_a) \\
 \psi_c(\theta) &= p_I + p_{II} \cos(\theta\omega_p)
 \end{aligned}
 \tag{5.3}$$

Values for the parameters in Equations (5.2) and (5.3) can be found in Table 5.1.

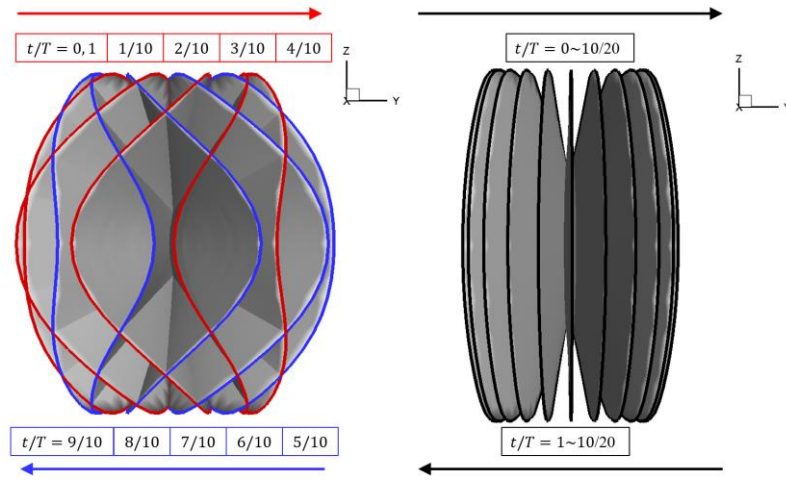
A rigid-fin model is also set up as Case 1 and Case 3 in Table 5.1. As all flexible fins are driven by their leading fin rays (Li et al., 2018), the amplitudes of the leading fin rays for rigid fins are set to be identical to their flexible counterparts to ensure that the results are comparable. It was noted from the experiment that the dorsal and anal fins undulated in phase with each other, while there was a 180-degree (π) phase lag between the caudal fin and the other two fins.



(a) Dorsal fin



(b) Anal fin



(c) Caudal fin

Figure 5.3 Sketches for the envelopes of dorsal, anal and caudal fins in one motion period. Each envelope slice represents one motion moment. Red and blue lines in flexible condition (Case 4 left) stand for undulating from left to right and right to left respectively. Fins with rigid condition are presented at right and use Case 3 as an example. The motion period is split into 10 moments evenly for the rigid condition.

The motion profile is mathematically given in Equation (5.4) and graphically plotted in Figure 5.3 for Case 4 (left, flexible) and Case 3 (right, rigid), where the shape envelopes of each fin at ten evenly distributed time instants are displayed in one motion cycle.

$$\varphi(t) = A \sin(\omega t + \psi) \quad (5.4)$$

where ω is the flapping frequency; ψ is the phase lag and A is the flapping amplitude. Typical values for ω , ψ and A can be found in Table 5.1.

5.1.2 Computational domain and boundary conditions

The computational domain is generated using a cylindrical topology and separated into inner and outer zones, as displayed schematically in Figure 5.4. The length and the

radius of the overall computational domain are $12L$ and $10W$, separately, where L and W are the length and width of the fish model. As the fish swims towards the inlet boundary, the distance from the fish to the inlet is set to be larger than the distance away from the outlet. The outer zone is designed to be wide enough to avoid the influence of outer boundaries, and a relatively coarse mesh is adopted to achieve a reasonable mesh number. Meanwhile, as the self-propelled pufferfish model swims mainly in the inner cylindrical zone with a dimension of $10L \times 3W$, the mesh is deliberately refined in the inner zone to better capture flow characteristics and ensure the accuracy of numerical results.

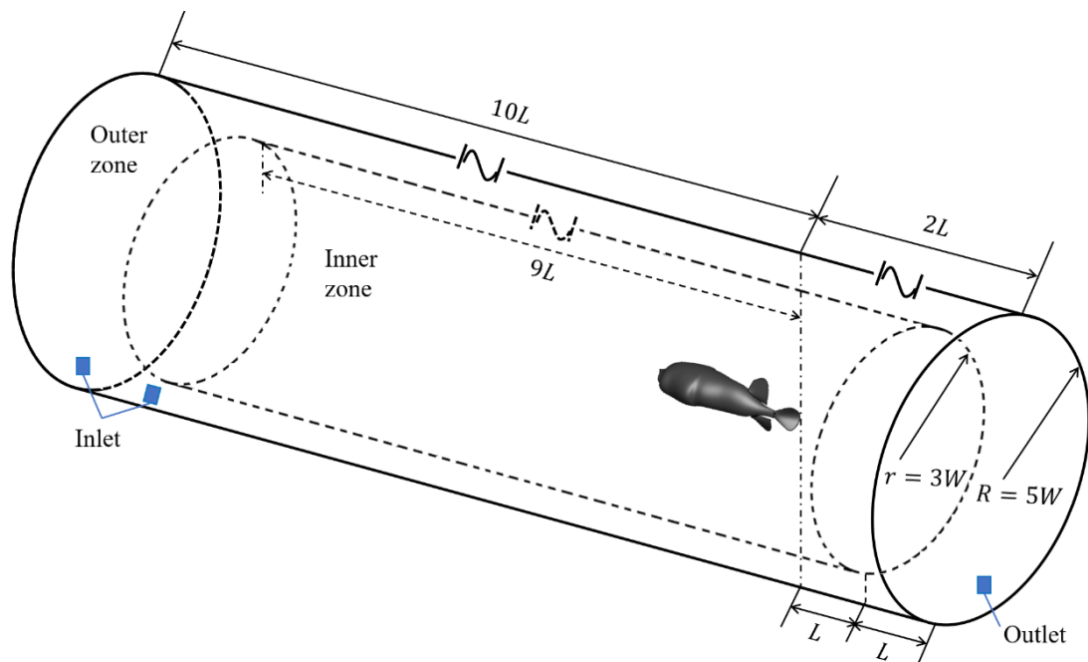


Figure 5.4 Computational domain. The whole domain is split into inner and outer zone. Inner zone has finer mesh, comparing to outer zone, to better capture the flow structure of fluid field.

Unstructured tetrahedral elements are used in the computational domain. The upstream and surrounding boundary is set as velocity inlet (i.e., $\vec{u} = (0,0,0)$). The downstream boundary is set as pressure outlet with zero gauge pressure. A no slip boundary

condition is applied to the surface of the fish model. Since the fish swims in still water, the initial flow field velocity is set to zero.

5.1.3 Grid and time step size independence tests

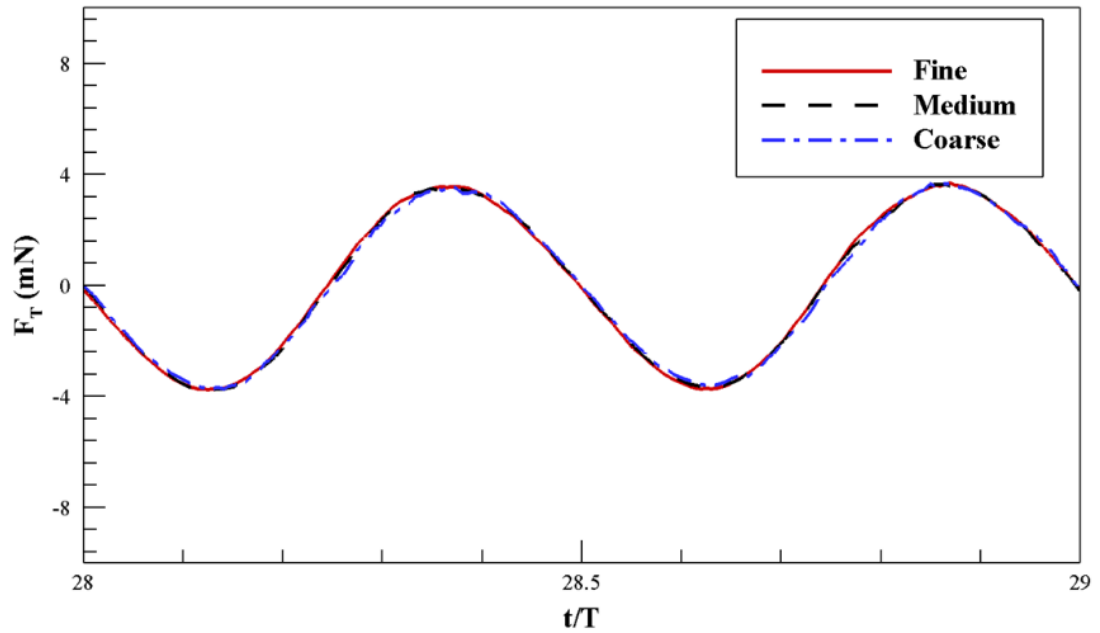
Due to the large deformation of the mesh when fish swims, the dynamic mesh functionality available in FLUENT is used. In order to guarantee the mesh quality during the simulation, smoothing and re-meshing functions are employed.

Table 5.2 Information for three different meshes

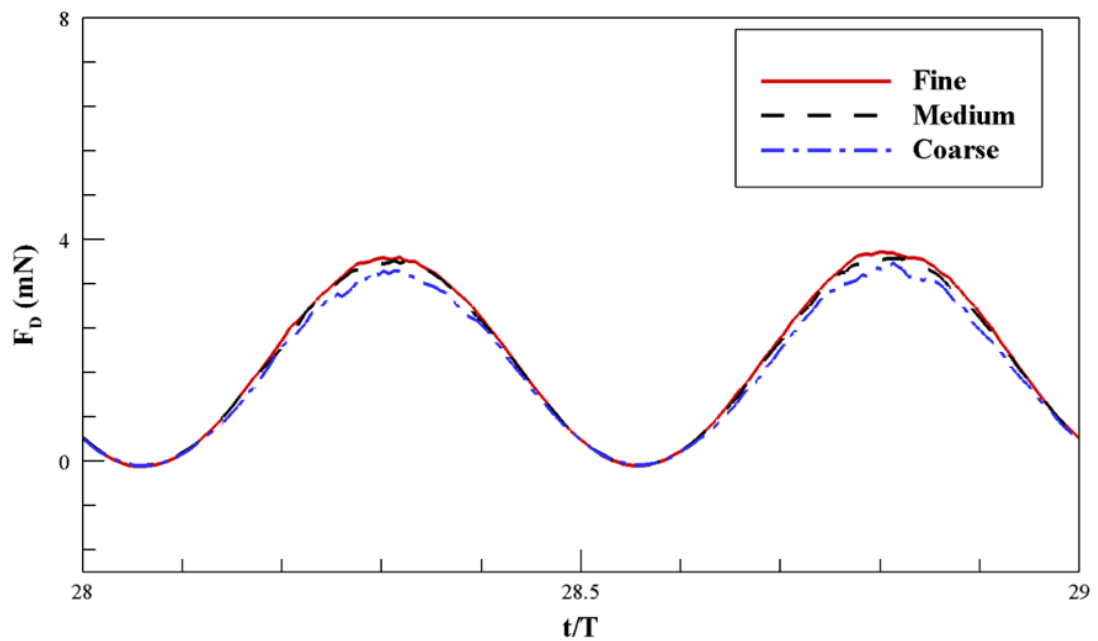
Mesh	N_{face} (M)	$N_{element}$ (M)	$\Delta z_{min} / L$	$\Delta z_{max} / L$
Coarse	0.013	0.56	5.2e-3	4.2e-1
Medium	0.029	1.59	3.4e-3	2.9e-1
Fine	0.051	3.06	2.9e-3	2.2e-1

To quantify the dependency of the numerical results on the mesh density, a simulation of a free-swimming pufferfish with the kinematics in Case 4 is performed. Three sets of mesh with different grid density are generated as summarised in Table 5.2, in which N_{face} , N_{cell} , $\Delta h_{min} / L$ and $\Delta h_{max} / L$ represent the number of faces on the surface grid of the fish, the number of mesh cells in the computational domain, the minimum and maximum dimensionless cell height, respectively. The cell height is normalised by the fish length L . The total mesh number of the medium mesh is 1.6 million, which is about three times the coarse mesh and half of the fine one. Figure 5.5(a) shows the results of grid independence tests in the 29th undulating period with respect to total force F_T . It illustrates that F_T obtained from the medium mesh is almost identical to the result from the fine mesh but slightly different from that with the coarse one. Meanwhile, as the grid around the fins are deformed greatly during fish swimming, force results around the dorsal fin from the mesh independence test are also compared in Figure 5.5(b). It is shown that the time series of force obtained with medium and fine mesh density are almost the same while the result from the coarse mesh is

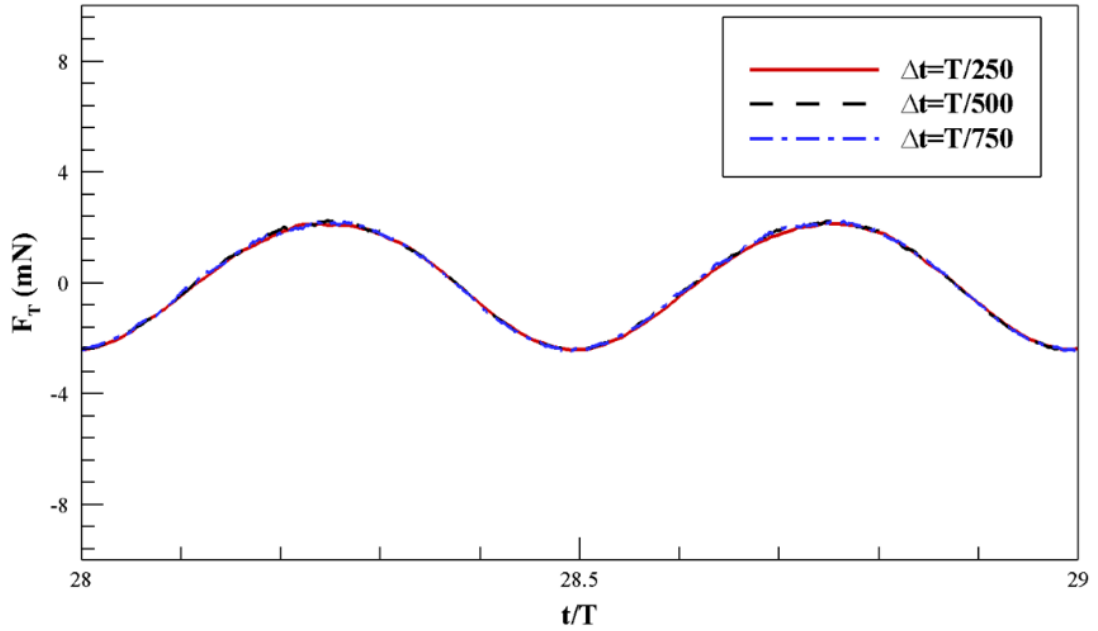
noticeably smaller than the other two cases. Hence the medium mesh is selected for all subsequent simulations.



(a) Three different mesh densities for Case 4



(b) Mesh density tests of force on dorsal fin for Case 4



(c) Three different time-step sizes for Case 2

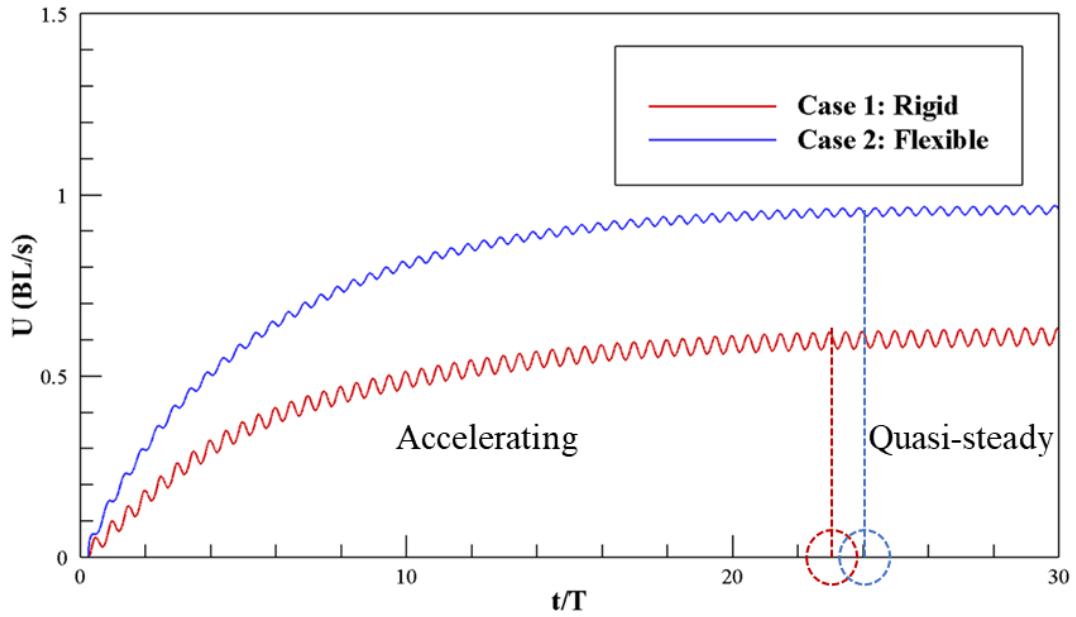
Figure 5.5 Grid and time-step size independence tests

As it is an unsteady problem, a time-step size dependency test is also conducted with a medium mesh using the kinematics of flexible fins in Case 2. Three time-step sizes are selected, namely $\Delta t = T/250, T/500, T/750$, where T stands for the motion period ($T = 2\pi/\omega$). Figure 5.5(c) compares the total force F_T on the fish during the 29th motion cycle among the cases. The results are almost identical between $\Delta t = T/500$ and $\Delta t = T/750$, and a slight difference exists for $\Delta t = T/250$ compared to the other two cases. Thus, a time-step size $\Delta t = T/500$ is adopted for the rest of modelling.

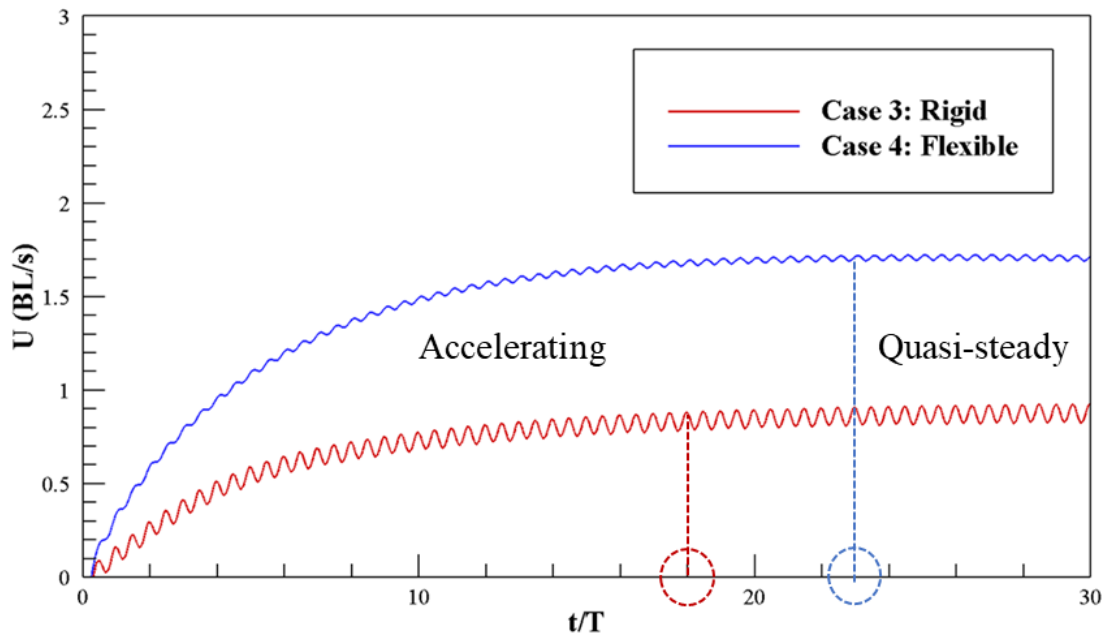
5.2 Results and Discussions

In this section, a three-dimensional self-propelled pufferfish induced by the motions of rigid/flexible dorsal, anal and caudal fins are simulated over a total of 30 motion cycles. As listed in Table 5.1, Case 2 and Case 4 focus on the pufferfish with flexible fins, and their corresponding conditions with rigid fins are given in Case 1 and Case 3, respectively. The preliminary results from the CFD simulations revealed that the fish

mainly swam in X translational direction. Thus, the following discussions are mainly concentrated on the analysis of swimming velocity and force in the X direction.



(a) Velocity development for Case 1 (rigid) and 2 (flexible)



(b) Velocity development for Case 3 (rigid) and 4 (flexible)

Figure 5.6 Velocity comparisons between rigid (Case 1 and 3) and flexible (Case 2 and 4) fins cases

5.2.1 Induced velocity U

The development of velocity in the X direction over 30 motion cycles is presented and compared in Figure 5.6. It can be seen that fish swimming follows a similar trend regardless of whether they are driven by the rigid or flexible fins, i.e., a pufferfish accelerates from motionless to a quasi-steady stage as indicated in Figure 5.6. Similar development stages have also been found for other types of self-propelled swimmers, such as thunniform (Li et al., 2017), carangiform (Borazjani and Sotiropoulos, 2010; Li et al., 2012) and anguilliform (Kern and Koumoutsakos, 2006). Acceleration takes about 23, 24, 18 and 23 motion cycles for Cases 1 to 4, respectively.

Table 5.3 Time-averaged velocity in x direction for quasi-steady stage

Case No.	1	2	3	4
\bar{U} (BL/s)	0.61	0.96	0.87	1.71

It is interesting to note that the fish with flexible fins moves faster than that driven by rigid ones. The time-averaged velocity \bar{U} during the quasi-steady stage is summarised in Table 5.3 for the four cases. The velocity generated by flexible fins can be up to twice as much as that with rigid fins. Evaluated against the experimental measurement (Li et al., 2018), where the velocities of 1BL/s and 2BL/s were specified for a live fish associated with Case 2 and 4, the predicted CFD simulations predict a forward speed of 0.96BL/s and 1.71BL/s, which are underestimated by about 4% and 14.5%, respectively. Obviously, the consistency between CFD predicted results and experiment is very well at a low speed, but the discrepancy increases when the speed increases. A relevant previous study by Wiktorowicz et al. (2007) pointed out that fish caudal peduncle started its oscillating motion at high swimming speeds above 1BL/s, while in the present CFD model the caudal peduncle motion is excluded, which likely accounts for the discrepancy between the experimental and numerical results at 2BL/s. It is thus suggested that the caudal peduncle motion of the pufferfish during self-propulsion may not be omitted when the swimming velocity is larger than 1BL/s. This would be considered in the near future study.

It is also observed from Figure 5.6 that the cruising velocity fluctuates around a mean value after reaching the stage of quasi-steady swimming. The fluctuation amplitude of the velocity for each case is $0.024BL$ (Case 1, rigid fins), $0.049BL$ (Case 3, rigid fins), $0.012BL$ (Case 2, flexible fins), and $0.015BL$ (Case 4, flexible fins). For flexible fins, velocity fluctuation accounts for 1.25% (Case 2) and 0.8% (Case 4) of the mean velocity \bar{U} , separately. Whereas for the two rigid cases, this fluctuation increases significantly to 3.9% and 5.6% for Cases 1 and 3, respectively. A further analysis on the difference of fluctuation amplitude of cruising velocity will be carried out in Section 5.2.2 along with the investigation on hydrodynamic forces.

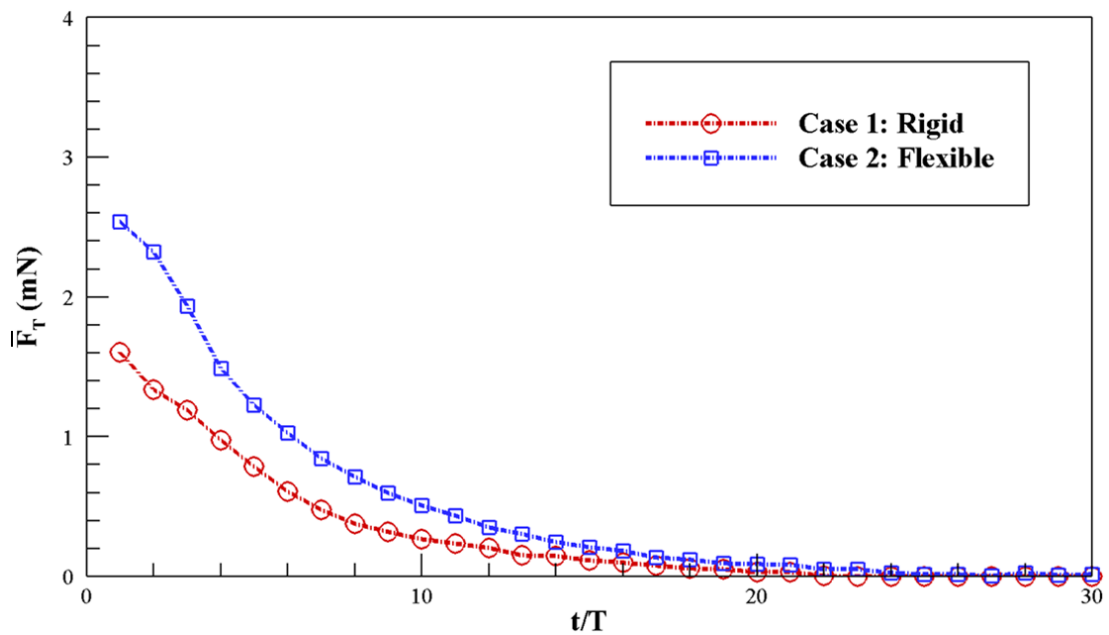
The phenomenon of a fluctuating cruising velocity was also observed in previous studies for other species of fish though the fluctuating amplitude might be different. For instance, a self-propelled zebrafish larva (carangiform swimming) reached $18BL/s$ with a 11.1% fluctuation (Li et al., 2012). In the study of Kern and Koumoutsakos (2006), the final quasi-steady velocity for a typical anguilliform swimmer was $0.33BL/s$ with 2.1% fluctuation. For a thunniform fish with a rigid caudal fin, it was found that a cruising velocity of $0.278BL/s$ could be achieved with a fluctuation amplitude of 0.41% (Li et al., 2017).

5.2.2 Hydrodynamic force and surface pressure

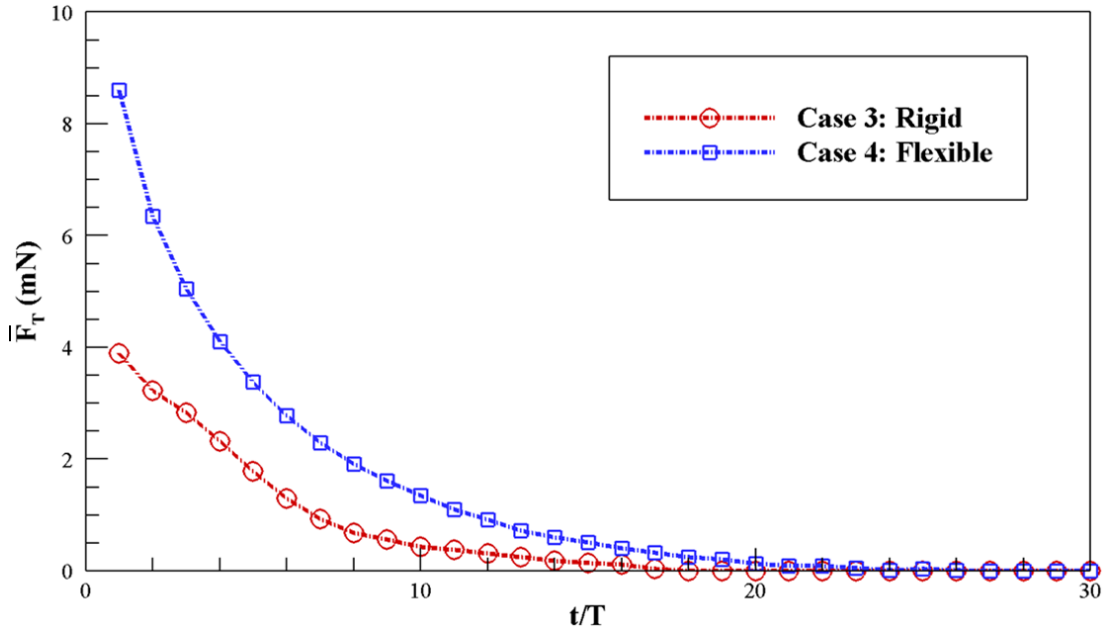
In this section, hydrodynamic forces on the fish body and its fins will be discussed in the following aspects: cycle-averaged total force \bar{F}_T , instantaneous propulsive force F_p , instantaneous force on each fin F_D , F_A and F_C , force F_B and pressure distribution on the fish body. For these forces, a positive value represents a thrust force, while a negative one is an indication of drag or resistance force.

5.2.2.1 Cycle-averaged total force \bar{F}_T and instantaneous total force F_T

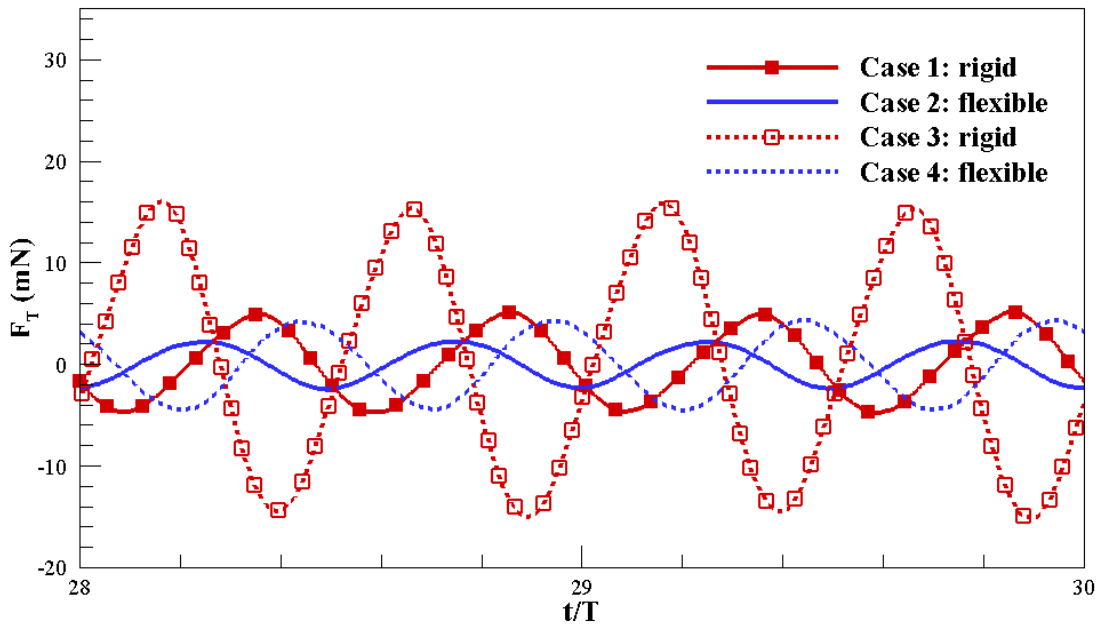
Figure 5.7(a) and (b) illustrate the cycle-averaged total force \bar{F}_T over each single cycle within 30 periods for Cases 1-4. It is seen that \bar{F}_T for a self-propelled pufferfish with flexible fins is larger than that with rigid fins, implying that a fish with flexible fins has a larger acceleration than its counterpart of rigid fins. In addition, it is also noted that \bar{F}_T decreases to zero after 23, 24, 18 and 23 motion periods for Cases 1-4, suggesting that fish starts its cruising stage from those cycles onwards. This is in line with the duration of the acceleration stage discussed in the previous Section 5.2.1 on the induced velocity. For the pufferfish with flexible fins, the obtained larger acceleration plus the longer accelerating time leads to its larger mean swimming velocity compared to that with rigid fins.



(a) Cycle-averaged total forces for Cases 1 and 2



(b) Cycle-averaged total forces for Cases 3 and 4



(c) Total force for four cases in two motion cycles

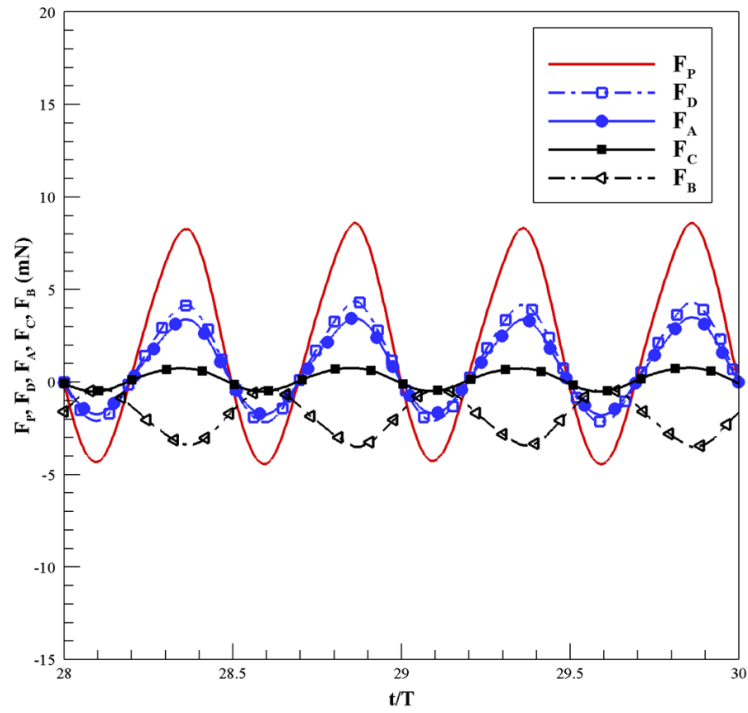
Figure 5.7 Comparisons of Cycle-averaged total forces \bar{F}_T and total force F_T between rigid (Cases 1 and 3) and flexible (Cases 2 and 4) fins cases

Figure 5.7(c) shows the time history of the instantaneous total force F_T for four cases in the 28th to 29th motion cycle. It is noted that with rigid fins, the amplitude of F_T is larger than that of flexible conditions. A large force amplitude represents a large fluctuation in F_T , and this has been reflected in the fluctuating velocity shown in Figure 5.6 as discussed in Section 5.2.1. This phenomenon is also in line with a previous study about a self-propelled thunniform fish by Li et al. (2017), whose results showed that a large force amplitude led to a large fluctuation on the cruising velocity of the fish.

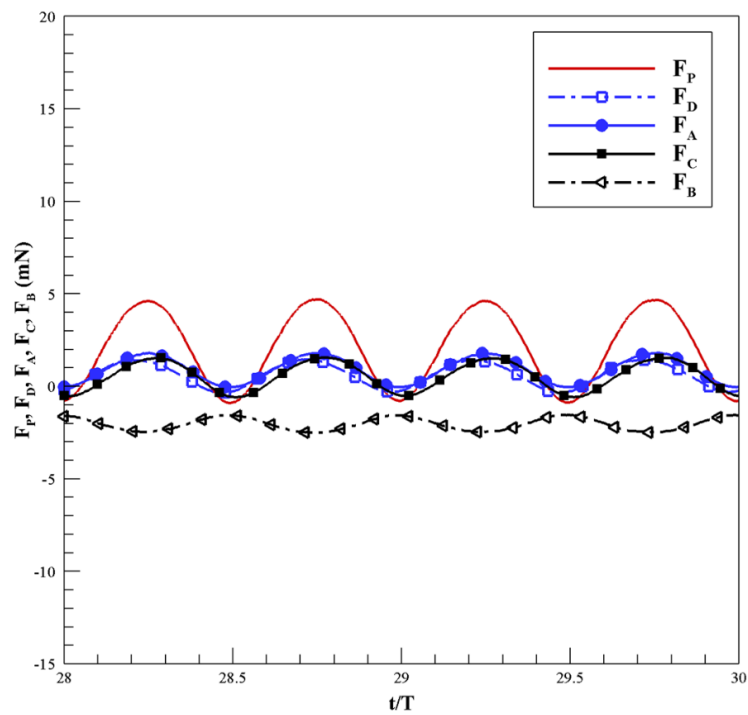
5.2.2.2 Propulsive force F_p

The instantaneous hydrodynamic propulsive force F_p , which is the sum of forces generated by anal, dorsal and caudal fins as defined in Section 3.5.3, is illustrated in Figure 5.8(a)-(d). With an identical kinematic motion profile being imposed on the leading fin ray for both rigid and flexible fins, the amplitude of F_p for the fish with rigid fins is larger than that of the fish driven by flexible fins. Moreover, by comparing the two results within the same time frame, it can be found that there is a phase lag between the flexible and rigid fins. Although the motions of the fins are driven by the leading fin ray, the trailing edge fin ray also undulates for a flexible fin, leading to a diverse surface locomotion of flexible and rigid fins, which is the reason behind for the phase lag between the propulsion forces.

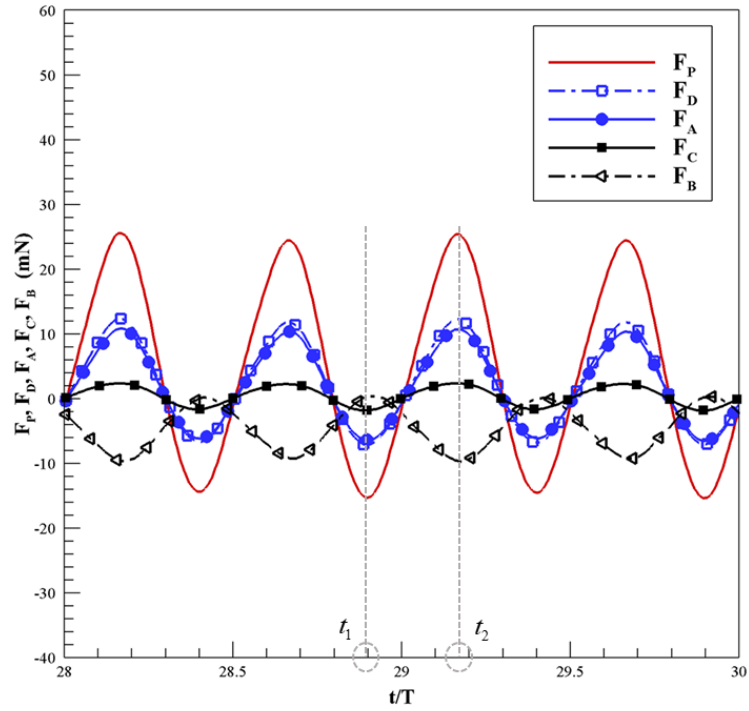
One important feature from Figure 5.8 is that the propulsive forces F_p associated with flexible fins are almost positive, while the rigid fins generate both positive and negative forces. This suggests that flexible fins mostly generate thrust forces whereas rigid fins produce not only thrust but also drag forces.



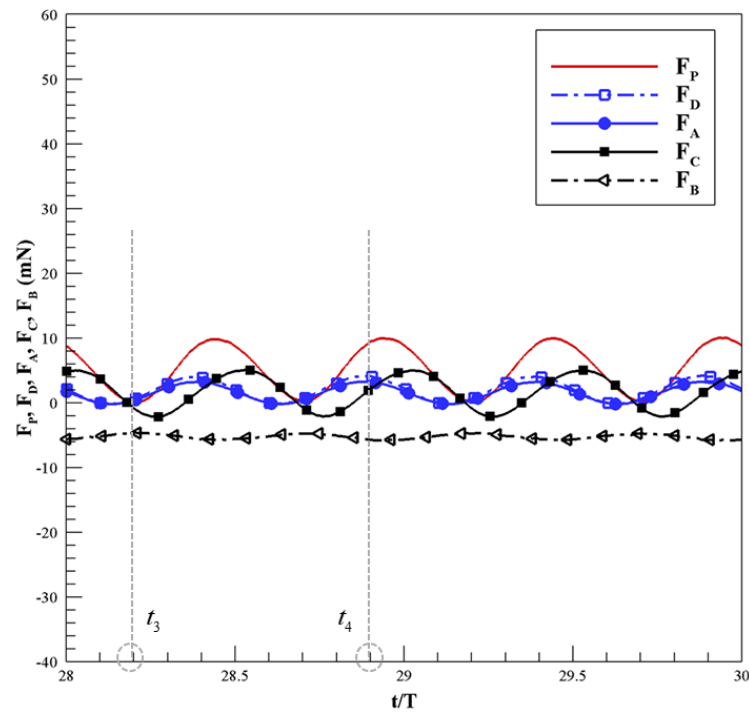
(a) Hydrodynamic forces of Case 1 (rigid fins)



(b) Hydrodynamic forces of Case 2 (flexible fins)



(c) Hydrodynamic forces of Case 3 (rigid fins)



(d) Hydrodynamic forces of Case 4 (flexible fins)

Figure 5.8 Hydrodynamic propulsive force F_p , force on dorsal F_D , anal F_A , caudal F_C and body F_B for four cases.

5.2.2.3 Force on each fin: F_D , F_A and F_C

To have a better understanding on the hydrodynamic performance of the fish fins, the instantaneous forces on each fin, i.e., dorsal F_D , anal F_A and caudal F_C , are plotted in Figure 5.8. Apart from the caudal fin, the dorsal and anal fins also produce propulsive forces thus contribute to the propulsion of fish swimming. For both rigid and flexible conditions, the dorsal and anal fins have nearly equal contributions to the propulsive force, which is indicated by the amplitude of F_D and F_A . This is consistent with the findings from previous studies (Han et al., 2016; Liu et al., 2017a). Han et al. (2016) found that the mean thrust coefficient of a fish with dorsal and caudal fins was equal to that with anal and caudal fins. Liu et al. (2017a) studied a full fish body-fin model, which included fish body, dorsal, anal and caudal fins. In their study, dorsal and anal fins undulated with the fish body without individual motions. Results of thrust force on dorsal and anal fins indicated that these two fins played similar roles in fish propulsion.

For the rigid cases of Figure 5.8 (a) and (c), the amplitude of F_C is smaller than that of F_D and F_A . However, for cases with flexible fins, the amplitude of F_C is equal to (for Case 2) or larger than (for Case 4) that of dorsal and anal fins as illustrated in Figure 5.8 (b) and (d). Meanwhile, compared to the rigid conditions, the amplitude of F_C with flexible fins significantly increases, but F_D and F_A considerably decreases. This clearly demonstrates the important impacts of flexible fins on fish hydrodynamic performance.

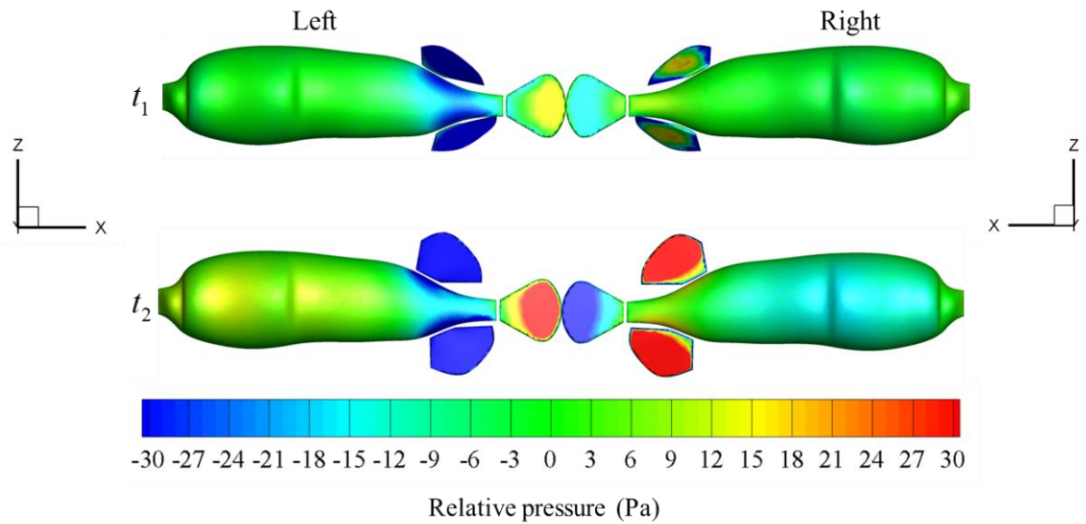
In addition to the above differences in the amplitude, it is also noted that there is phase lag among F_C , F_D and F_A . It can be seen from Figure 5.8 that F_C is out of phase with F_D and F_A for the flexible conditions, especially for Case 4. On the contrary, these forces are always in phase with each other for the rigid cases. As the propulsive force F_p is the sum of the forces produced by all the fins, i.e., F_D , F_A and F_C , the

difference in the phase angle of these forces leads to a smaller fluctuation of F_p for flexible fins. Moreover, although the force generated by each individual fin can be negative within a certain amount of time in one motion cycle, the phase lag between these forces results in a mostly positive F_p .

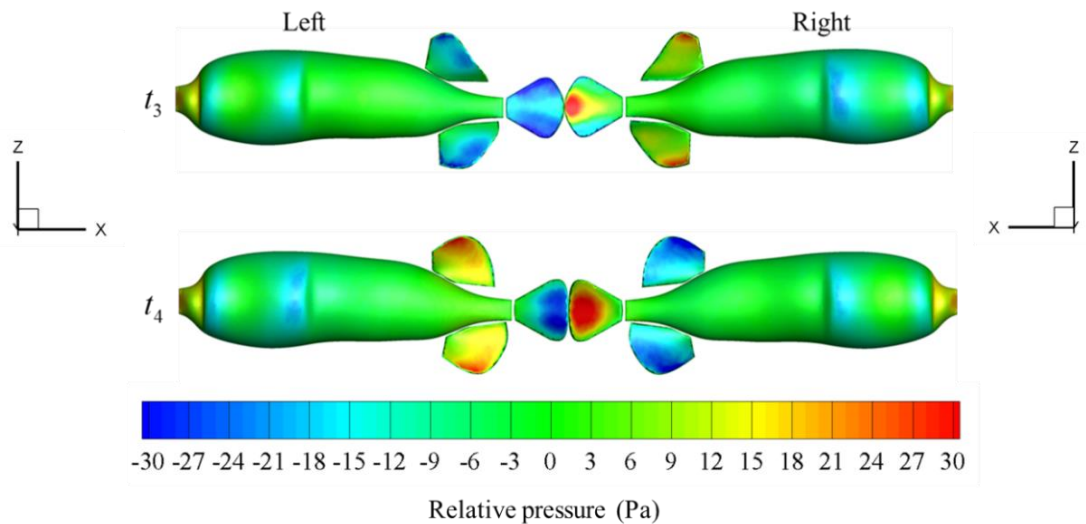
5.2.2.4 Force F_B and surface pressure on body

Apart from the aforementioned forces on fins, Figure 5.8 also displays the hydrodynamic force on the fish body F_B . As indicated in the plot, F_B always fluctuates with an averaged negative value. In addition, similar to F_D , F_A and F_C , the force F_B on the fish body with rigid fins also suffers larger fluctuation than with flexible ones. This can be further demonstrated from the pressure contour plots in Figure 5.9 for Cases 3 and 4 as examples.

Figure 5.9 presents the relative pressure (relative to the zero gauge pressure at the outlet boundary) distribution around the fish body. The selected time instants $t_1 - t_4$ are also marked in Figure 5.9 and correspond to the moment when F_B reaches its maximum/minimum for rigid and flexible conditions. For the rigid condition in Figure 5.9(a), $t_1 = 28.89T$ is the time at which F_B falls to its minimum and at $t_2 = 29.18T$ it reaches its maximum. For the flexible case displayed in Figure 5.9(b), F_B reaches its minimum and maximum at $t_3 = 28.22T$ and $t_4 = 28.91T$, respectively.



(a) Rigid: $t_1 = 28.89T$ (minimum F_B) and $t_2 = 29.18T$ (maximum F_B) for Case 3



(b) Flexible: $t_3 = 28.22T$ (minimum F_B) and $t_4 = 28.91T$ (maximum F_B) for Case 4

Figure 5.9 Distribution of pressure on fish surface relative to gauge pressure at outlet boundary

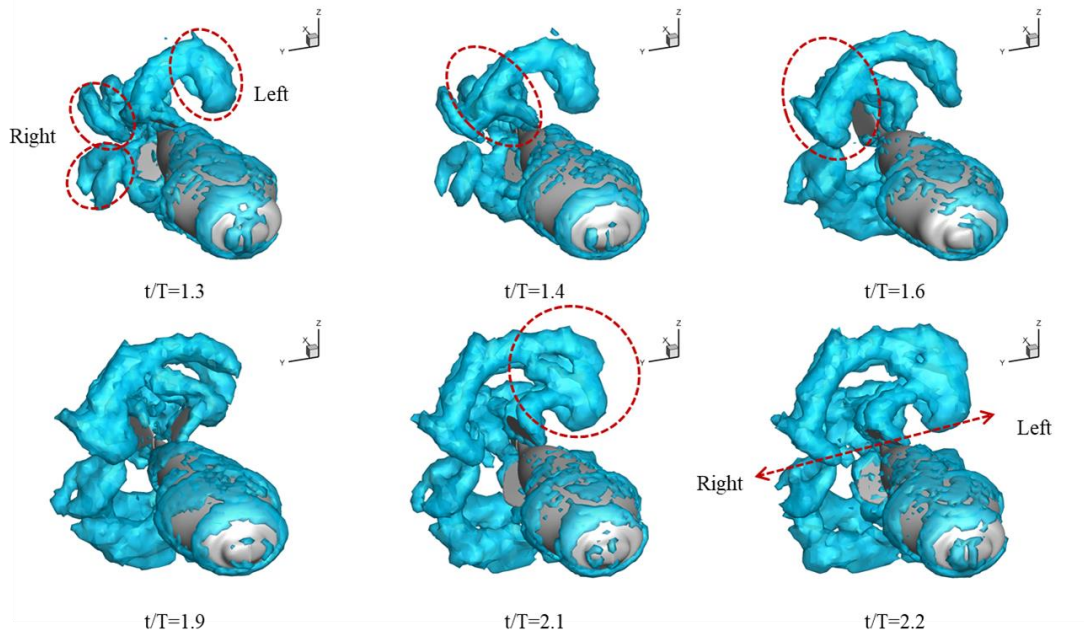
The differences of the body pressure distribution for both fin conditions exist even though the fish body is always rigid. By comparing the results at t_1 and t_2 , it reveals that the pressure on the fish body changes dramatically for the rigid condition, especially in the anterior body. Left and right views also show the differences in these

two moments, which explains the large fluctuation in F_B in Figure 5.8. The uniform motion of each rigid fin perturbs a larger amount of water around the model, which could be reflected by the pressure distribution on the rigid fins and will be further analysed in Section 5.2.3 from the aspect of vortex structure. On the contrary, the difference of the pressure distribution on the fish body between t_3 and t_4 for the flexible condition is subtle. This is in accordance with the small variation of F_B for flexible condition in the simulation. The anterior part of the fish body suffers a relatively larger pressure than the posterior part, indicating that resistance forces are exerted upon the fish body.

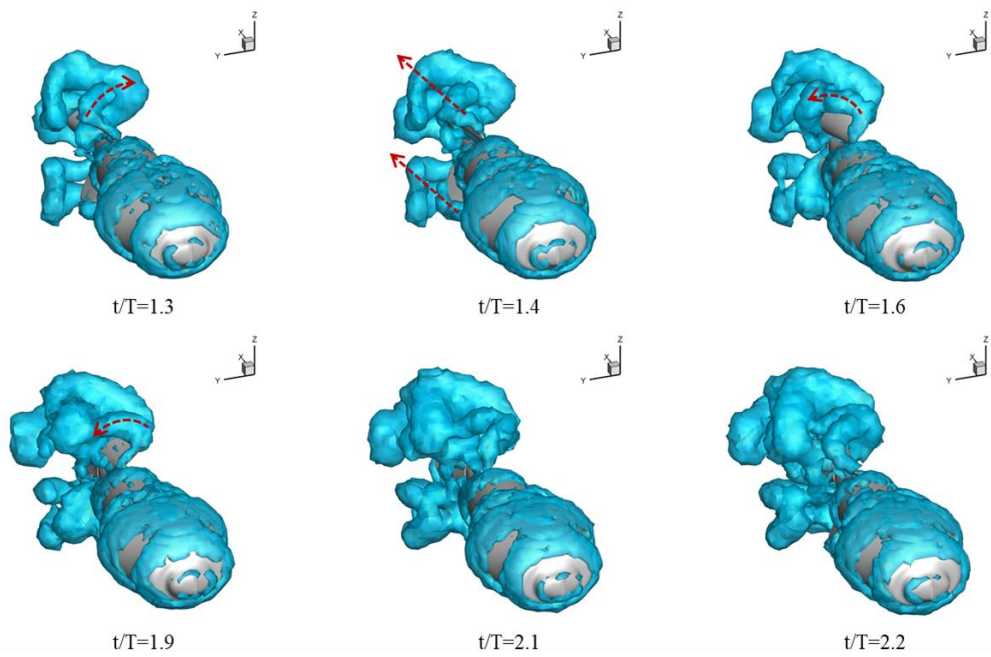
5.2.3 Vortex structure

To gain a better understanding on the formation and development of vortices, as well as the interactions between the vortices generated by rigid/flexible dorsal, anal and caudal fins, the vortex structure will be discussed in detail in this section. Examples about the formation of 3D wake structures will be firstly focused on Case 3 and 4 within the accelerating stage representing the rigid and flexible conditions. Subsequently, 2D contours will be presented for the slices of dorsal, anal and caudal fins for the four cases. Finally, comparisons of 3D vortex structure associated with Cases 1-4 at a given instant will be illustrated in XY and XZ planes.

Figure 5.10 presents three-dimensional wake structures for (a) Case 3 (rigid) and (b) Case 4 (flexible) as examples within one motion cycle. For both conditions, similar to the caudal fin, the dorsal and anal fins also create vortex rings. The locomotion of the fins causes the perturbation of fluid around the fish, especially the anterior part. This leads to the variation in the distribution of body pressure and the vortices are shed into the wake by different fins during the locomotion, thus propelling the fish forward. For the rigid condition in Figure 5.10(a), it is noted that the vortices are mainly generated by the leading and trailing fin rays and shed off laterally.



(a) Formation of vortices of pufferfish with rigid fins



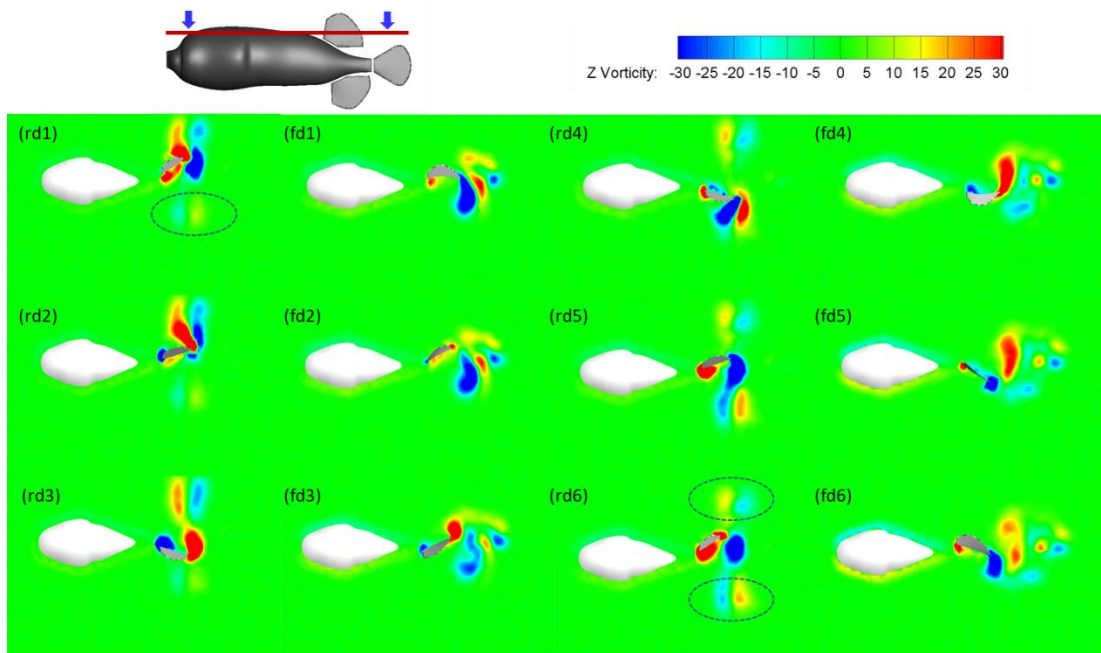
(b) Formation of vortices of pufferfish with flexible fins

Figure 5.10 Vortex topology for $t/T=1.3-2.2$ with Iso-surface $Q=2$ for (a) Case 3 and (b) Case 4

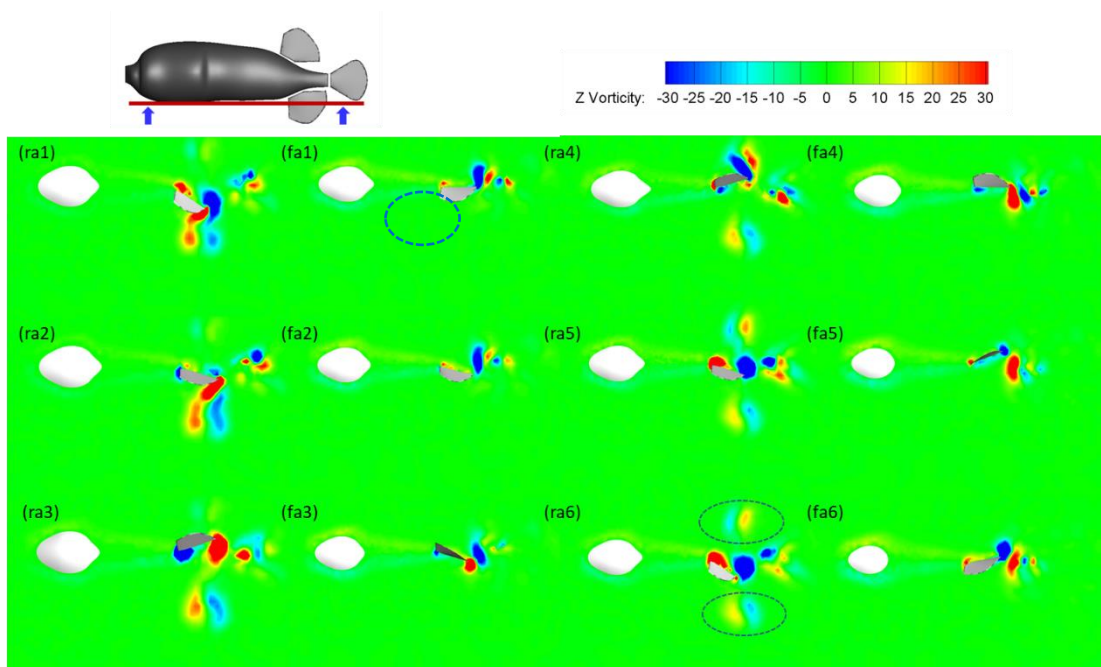
The dorsal fin is selected as an example to study the evolution of vortices. After one completed motion cycle, one separate vortex can be found on the right side of the fin and another one is being generated on its left side at $t/T=1.3$. From $t/T=1.3$ to 1.6, the dorsal fin flaps from right to left and generates a new vortex. It merges with the previous vortex on the right side. This phenomenon of vortex merging can also be observed when the fin flaps from the left to the right from $t/T=1.9$ to 2.2. Thus, the vortices formed with rigid fins are primarily shed in the lateral direction at this stage. For the flexible fins plotted in Figure 5.10(b), vortices are also created by the leading and trailing fin rays. With the undulating motion of the dorsal fin, the vortices are shed off from the fin tip to the downstream of the fish, which is in contrast with the rigid fin. The differences in the wake for rigid and flexible conditions can also be found on the anal and caudal fins.

In order to have a better understanding on the interaction of vortices generated by different fins, three plane slices are presented in Figure 5.11 at six selected time instants for Cases 3 and 4. A red line indicates the slice position and blue arrows show the perspective. Contours of the Z component of vorticity are displayed for the dorsal fin in Figure 5.11(a) and for the anal fin in Figure 5.11(b). Figure 5.11(c) shows the contour plots for X vorticity for the caudal fin. From these slice views, disparities in the development and interaction of vortices can be obviously noted. For instance, the rigid dorsal fin creates large vortices around both its leading fin ray and the fin tip while the flexible fin mainly induces vortices near its tip. Moreover, as discussed above, the vortices indicated inside the dashed-line boxes in Figure 5.11(a) clearly demonstrate their movement in lateral directions for the rigid fin while vortex streets mainly form in the downstream of the flexible fin. Similar results can be found for the anal fin as illustrated in Figure 5.11(b). For the caudal fin in Figure 5.11(c), vortices generated by the dorsal and anal fins are also noticeable as highlighted in dashed-line boxes. It is found that compared to the rigid fins where these vortices are scattered, the vortices from the flexible dorsal and anal fins are much closer to those from the caudal fin. Some merged vortices in the wake could also be observed at some instants, such

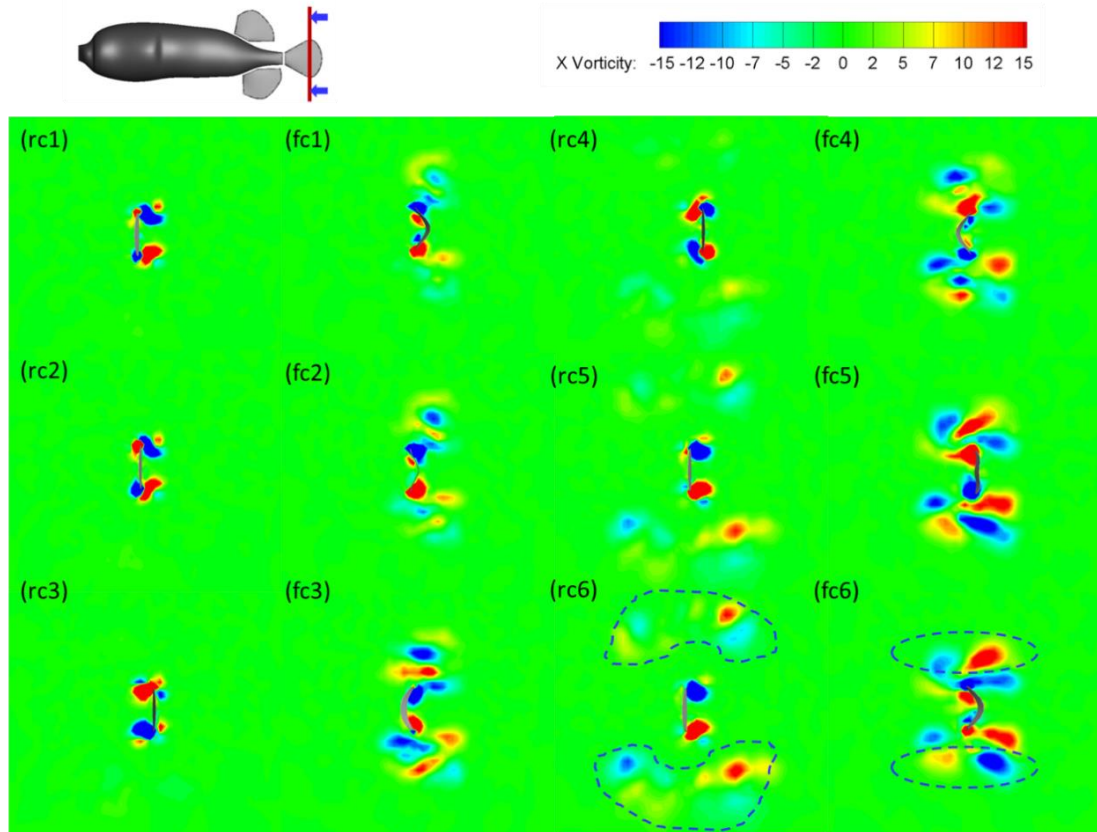
as (fc3) and (fc6). This implies that the flexible caudal fin is largely influenced by its upstream dorsal and anal fins and a strong interaction exists among those fins.



(a) Contour of z vorticity on dorsal slice. Rigid dorsal (rd) and flexible dorsal (fd)



(b) Contour of z vorticity on anal slice. Rigid anal (ra) and flexible anal (fa)



(c) Contour of x vorticity on caudal slice. Rigid caudal (rc) and flexible caudal (fc)

Figure 5.11 Contours of slices for dorsal, anal and caudal fins for Cases 3 and 4 at

$t/T = (1) 1.3, (2) 1.4, (3) 1.6, (4) 1.9, (5) 2.1, (6) 2.2$

The vortex structure for Cases 1-4 from different views at a specific time instant of $t/T=5.2$ is illustrated in Figure 5.12 to better demonstrate their dissimilarities during the accelerating stage. For the two rigid cases, the vortices produced by the dorsal and anal fins are shed off away from caudal fin with an oblique angle **A** in XZ plane in Figure 5.12(a). Another oblique angle **B** is also observed in the vertical view between two rows of vortices from the dorsal and anal fins in XY plane in Figure 5.12(b). With a forward speed of 0.33 BL/s and 0.51BL/s for Case 1 and Case 3, respectively, it is clearly seen that both angles **A** and **B** decrease as the induced swimming velocity increases. In contrast to the rigid cases, it is noted that in the near wake, a single row of vortices, made of a series of linked vortex rings, is generated by each flexible fin. Unlike the rigid fins which shed scattered vortices travelling laterally, the flexible

dorsal and anal fins generate vortices that are close to each other and move in the streamwise direction. Although the aforementioned 3D wake structure is complicated, some previous studies also showed similar vortex structures using simplified models. For instance, by varying the aspect ratio, which was defined as the ratio of major and minor axis of the ellipse, Dong et al. (2005) found that the aspect ratio of a 3D elliptical foil had significant impact on the wake structures. Two sets of vortex rings were generated by the low aspect ratio foils and formed an oblique angle to the wake centreline in the XY plane. An increasing aspect ratio led to these two rows merging with each other, i.e., a single wake in the streamwise direction.

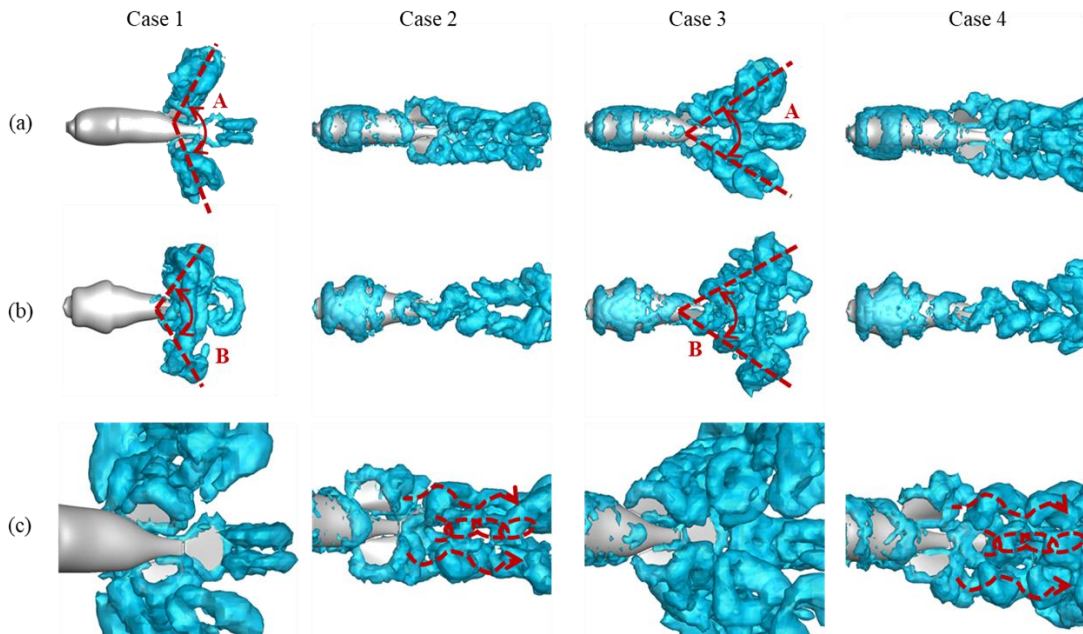


Figure 5.12 3D vortex topology of Iso-surface $Q=2$ at $t/T=5.2$ for four cases from (a) XZ view with included angle **A**, (b) XY view with included angle **B** and (c) zoomed-in XZ view

With a zoom-in view in XZ plane, it can be found that the vortices generated by different rigid fins are more scattered in Figure 5.12 (c) and thus little vortex interaction is discovered between the caudal fin and the other two fins. In contrast, the vortices generated by the flexible caudal fin are directly affected by those shedding from flexible dorsal and anal fins. Moreover, it can be obviously observed that the

vortices generated by flexible dorsal, anal and caudal fins merge in some wake regions, as mentioned previously. This phenomenon is roughly in line with the 3D view proposed by Tytell (2006) about the vortex structures in the streamwise direction, where the hairpin vortex rings generated by the caudal fin were influenced by the vortices from the dorsal and anal fins, and these three vortices were probably linked up. It is well accepted that the vortex topology is the reflection of the energy consumption. As scattered vortex structure indicates a dissipation of energy, the above fluid flow visualization results reveal that more energy is dissipated and consumed with rigid fins compared to flexible fins, as will be discussed in the following section.

It is noted from the above analysis that a small oblique angle in the vortex structure is good for the increase of the swimming velocity during the accelerating stage. Meanwhile, the vortices generated by fish with flexible fins can be better utilised because of the merging phenomenon. Thus, the self-propelled fish in Case 4 has the largest velocity and highest efficiency whereas the performance of fish in Case 1 is the worst among the four cases.

5.2.4 Power and Efficiency

A summary of the power and efficiency for four cases, which are defined in Section 3.5.3, is given in Table 5.4. With the same motion imposed on the leading fin ray, the pufferfish with rigid fins (Case 1 and 3) requires 4.6 and 6.7 times more consumed power than the corresponding flexible fins (Case 2 and 4). However, it only produces 59.9% and 62.5% of the output power, i.e., the useful power, from flexible fins. These results demonstrate that the rigid fins consume more energy/power but generate relatively less useful power than the flexible fins, implying that most of the input energy is dissipated with rigid fins as discussed in the previous section of vortex structure. Hence, a dramatic improvement in efficiency is achieved for a self-propelled pufferfish with flexible fins, as presented in Case 2 and 4.

Table 5.4 Averaged Power and Efficiency

Case No.	1	2	3	4
Averaged Consumed Power \bar{P}_c (mW)	2.5	0.544	12	1.79
Averaged Output Power \bar{P}_{out} (mW)	0.13	0.217	0.5	0.8
Efficiency η_{eff}	5.3%	39.89%	3.87%	45.44%

The efficiency for several types of swimming fish from other studies are compared in Table 5.5. Due to the diverse definitions about the efficiency of fish swimming, the studies that gave the Froude efficiency are compared to the present study. Meanwhile, the efficiency given in Table 5.5 for the present study is the self-propelled pufferfish with flexible fins, i.e., the realistic pufferfish (tetradontiform). It is noted that its efficiency is lower than the thunniform fish, the swimming mode of which is widely considered to be the most efficient among the various swimming types (Roper et al., 2011). However, it is noted that with multiple fins, tetradontiform fish could achieve a relatively high efficiency, compared to anguilliform and carangiform fish.

Table 5.5 Efficiency comparisons for different swimmers

Literature	Fish	Efficiency
Li et al. (2017)	Tuna (Thunniform)	30-65%
Present study	Pufferfish (Tetradontiform)	39% - 45%
Borazjani and Sotiropoulos (2010)	Eel (Anguilliform)	17.5%-32.1%
Borazjani and Sotiropoulos (2010)	Mackerel (Carangiform)	18.6% - 22.1%

5.3 Concluding remarks

In this chapter, following the experimental study of multi-fin kinematics (Li et al., 2018), numerical simulations are carried out to investigate a self-propelled pufferfish

with multiple flexible fins in accelerating and quasi-steady swimming stages. To reveal the impacts of flexible fins on thrust generation, cases with rigid fins are also considered with comparable conditions. The locomotion of the pufferfish is solved with an in-house Multi-Body Dynamics approach, which is coupled with the commercial CFD software package ANSYS Fluent used to solve the fluid field.

Given identical motions on the leading fin rays of dorsal, anal and caudal fins for rigid and flexible fins, the development of the forward swimming velocity associated with four test cases, i.e., two rigid and two flexible fins, has the same tendency as those previously studied for other types of swimmers (Kern and Koumoutsakos, 2006; Borazjani and Sotiropoulos, 2010; Li et al., 2012; Li et al., 2017). Consistent with the findings from the tethered swimming (Liu et al., 2017a), it is found that dorsal and anal fins also contributed to the propulsive force generation under self-propelled conditions. However, the hydrodynamic performance of the pufferfish with flexible fins is found to be distinctively improved, which is evidenced via a deep analysis on the predicted velocity, hydrodynamic force, power, and efficiency.

In addition, it is also noted that, driven by flexible fins, the fish can swim 1.6~2 times faster than that with rigid fins due to a larger acceleration and a longer accelerating procedure to develop compared to the rigid conditions. Meanwhile, flexible fins mostly generate positive forces with a small fluctuation, but rigid fins produce both positive and negative forces with a large oscillation amplitude. Obviously, these results support the previous finding that a swimmer with flexible fins is more efficient than the one with rigid fins. Further analysis on the vortex structure revealed that, the vortex shedding energy can be better utilized by the fish with flexible fins, which leads to less power consumption and further results in an enhanced efficiency. Although only four cases are examined due to limited experimental data, the numerical modelling methodology developed herein can be applied to a wide range of parametric studies for MPF swimmers under free-swimming conditions.

Chapter 6 The Role of Dorsal and Anal Fins during Unsteady Fish Swimming

A further analysis on the role of dorsal and anal fins during unsteady swimming will be carried out in this chapter. A fish will be exposed to a small perturbation and the time it takes for the fish to return to a quasi-steady status will be investigated. Based on the results of pufferfish with a Body-Dorsal-Anal-Caudal (BDAC) model in Chapter 5, another model will be established, named as Body-Caudal (BC) by removing the dorsal and anal fins of the pufferfish, and its self-propelled motion entirely relies on the caudal fin. Results obtained with the two models will be compared.

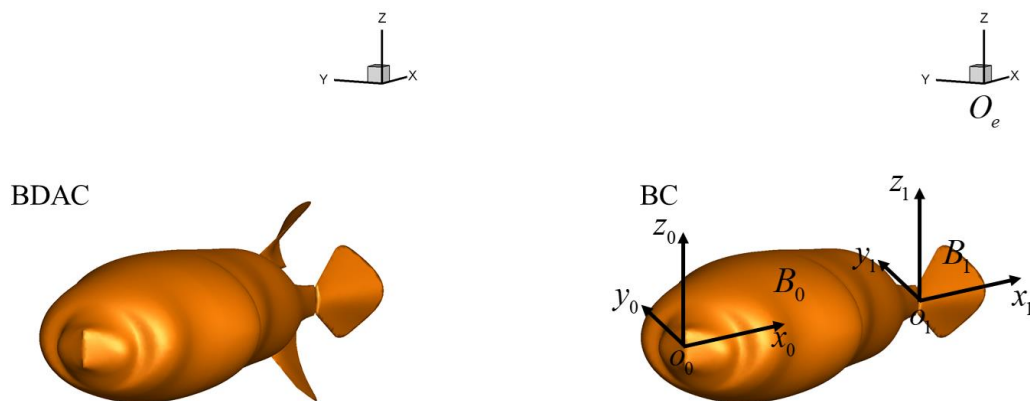


Figure 6.1 Sketches of Body, Dorsal, Anal, Caudal (BDAC, left) and Body, Caudal (BC, right) models

6.1 Motivation

In nature, fish perform fast start (Chao et al., 2017) to respond to sudden changes in their surroundings, e.g. being hunted by predators or variation of ambient flow. During this period, a series of unsteady motions, such as accelerating and manoeuvring, will be executed. Within a short period of time, fish will reach a steady swimming state. This ability of fish is normally referred to as stability (Webb and Weihs, 2015), which

is essential for fish to survive and is thus worth investigations. Meanwhile, a previous study by Standen and Lauder (2005) found that dorsal and anal fins of fish could produce balancing torques during steady swimming. However, how these fins, i.e., dorsal and anal fins, function during unsteady fish swimming has been rarely analysed. It is thus both interesting and of importance to investigate the roles of dorsal and anal fins in fish stability studies. In this work, the stability of a pufferfish is assessed by firstly imposing a constant incoming current as a perturbation in ambient flow and then analysing its swimming performance, as will be presented in subsequent sections.

6.2 Model Description

6.2.1 Model creation

To further evaluate the function of dorsal and anal fins during unsteady swimming, besides the BDAC model used in Chapter 5, a pufferfish model with only a caudal fin is employed in this chapter as well, shown in Figure 6.1 as BC. Without the dorsal and anal fins, this model can be considered as a two-element serial-like MBD model and the coordinate systems are presented in Figure 6.1. Like previous modelling, the fish body is set as the reference body B_0 and the caudal fin is numbered as B_1 . For the BDAC model, the setup is the same as the case investigated in Chapter 5. The computational domains for the two models are identical.

Table 6.1 Case Number and Condition

Case No.	Model Components	Perturbation
1	BDAC	No
2	BDAC	Yes, $U_{in} = 0.96BL/s$
3	BC	No
4	BC	Yes, $U_{in} = 0.4BL/s$

6.2.2 Simulation cases

In this chapter, two kinds of working conditions, i.e., normal condition and perturbation condition, are investigated for both BDAC and BC models. Under both conditions, the models are stationary in the beginning of the simulations and start to swim with prescribed fin kinematics. For the normal condition, the fish model swims in still water to reach a quasi-steady status. Whereas under the perturbation condition, the fish model is subjected to frontal current with a constant velocity, which is determined as the value of the cruising velocity obtained in the normal condition. It should be mentioned that these two models have different incoming current velocity values, which ensures the current is suitable but not too strong to flush the fish away and cause simulations to fail. The MBD coordinate settings and kinematic profiles of Case 2 in Chapter 5 are also applied in this chapter to analyse the hydrodynamic performance of the fish. The four investigated cases in the following sections are numbered as shown in Table 6.1.

6.3 Results

In this section, results about the self-propelled BDAC and BC models in still water and in incoming current will be presented. Displacement of the models will firstly be given for the cases with perturbation. Velocity will also be presented until the model becomes quasi-steady swimming. Hydrodynamic forces exerted upon the models are then analysed. Furthermore, the vorticity structures for the four cases during the 2nd period will be shown to illustrate the differences among the different swimming conditions. Finally, power and efficiency will be calculated and compared.

6.3.1 Displacement and Velocity Development

Figure 6.2 shows the displacement of the two models swimming in incoming current, i.e., Cases 2 and 4. At the initial stage, both models experience negative displacement which increases with time. This indicates that the two models are flushed backwards, away from their starting position. Subsequently, the displacement reaches its largest

negative value and starts to decrease until zero. Finally, the models swim past their starting position and move forward. It is immediately noted that the time it takes for the two models to achieve the turning points is different.

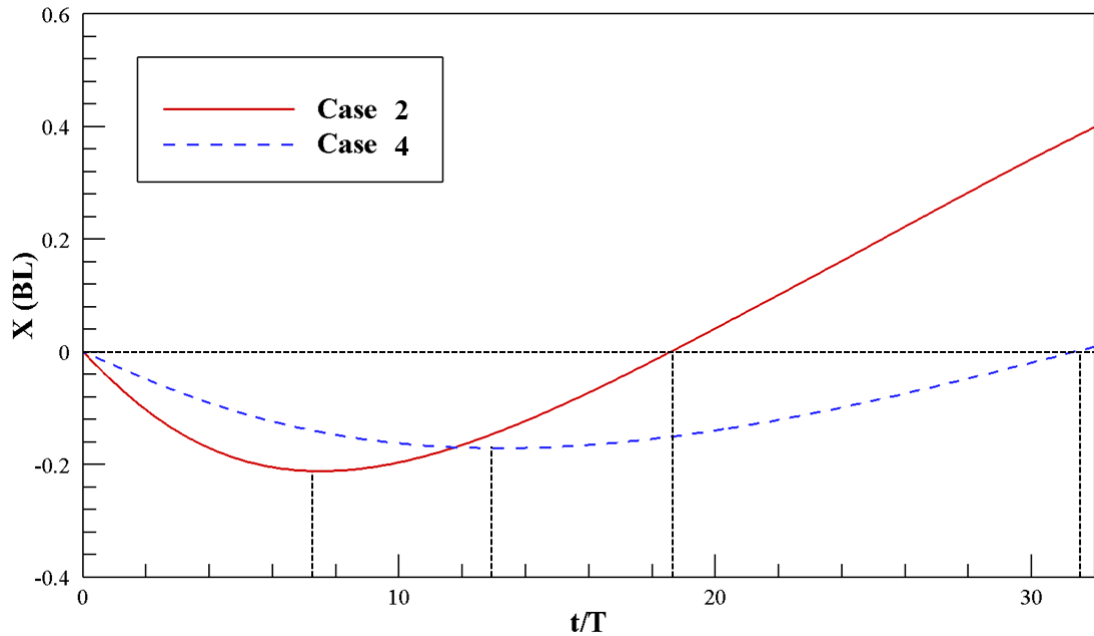
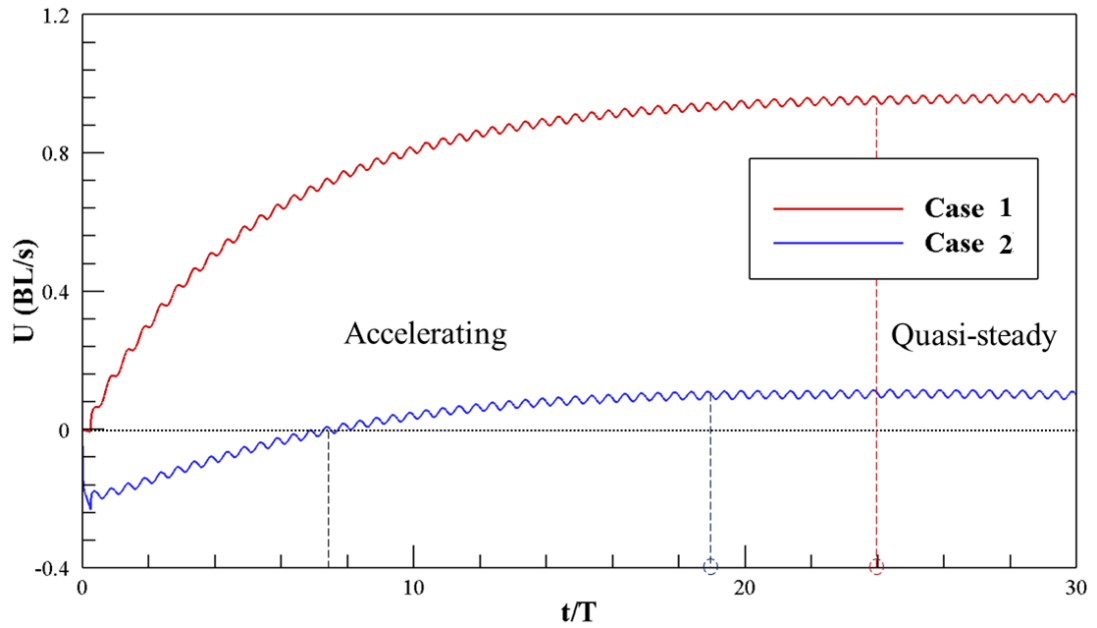


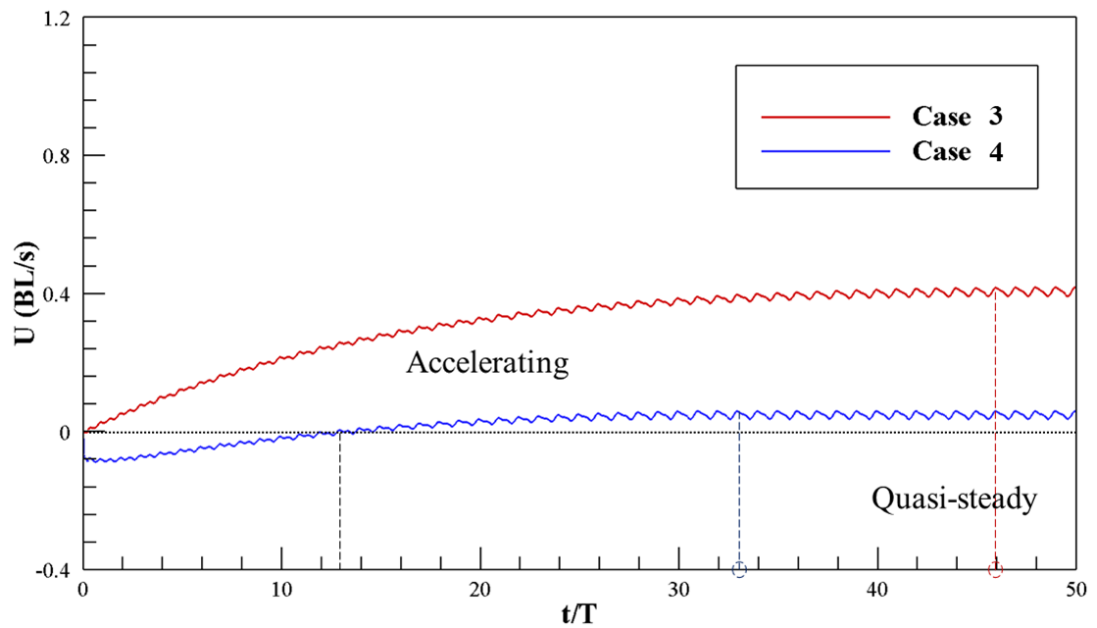
Figure 6.2 Displacement in X direction for Cases 2 and 4

The development of displacement is directly related to velocity, which is presented in Figure 6.3 for the four cases. Giving a constant velocity as the incoming current, both models (Cases 2 and 4) experience a decreasing negative swimming velocity. At the initial periods, the velocity generated by the fins (with or without dorsal and anal fins) is smaller than the current, so the fish has negative velocity and is flushed backwards, causing the displacement to increase in the negative (backward) direction. With the locomotion of the fish fins, the fish starts to resist the current. Its negative velocity becomes smaller and when it decreases to zero (black horizontal dashed lines in Figure 6.3), the displacement reaches its largest in the negative direction. It is found that it takes around 7.71 and 12.77 periods for the velocity of BDAC and BC models to cross zero, respectively. Then the velocity becomes positive, and the fish starts to swim in the positive (forward) direction. The fish finally returns to its original location after

18.56 and 31.27 periods for BDAC and BC models, respectively. It is thus noted that dorsal and anal fins may play important roles in helping fish recover from perturbation.



(a) Velocity development for Cases 1 and 2



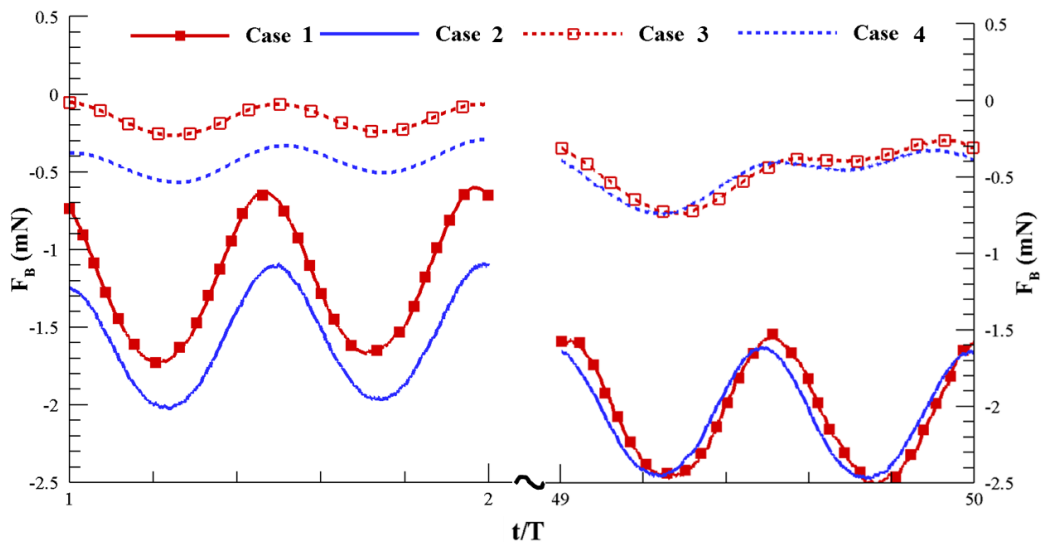
(b) Velocity development for Cases 3 and 4

Figure 6.3 Velocity comparisons for four cases

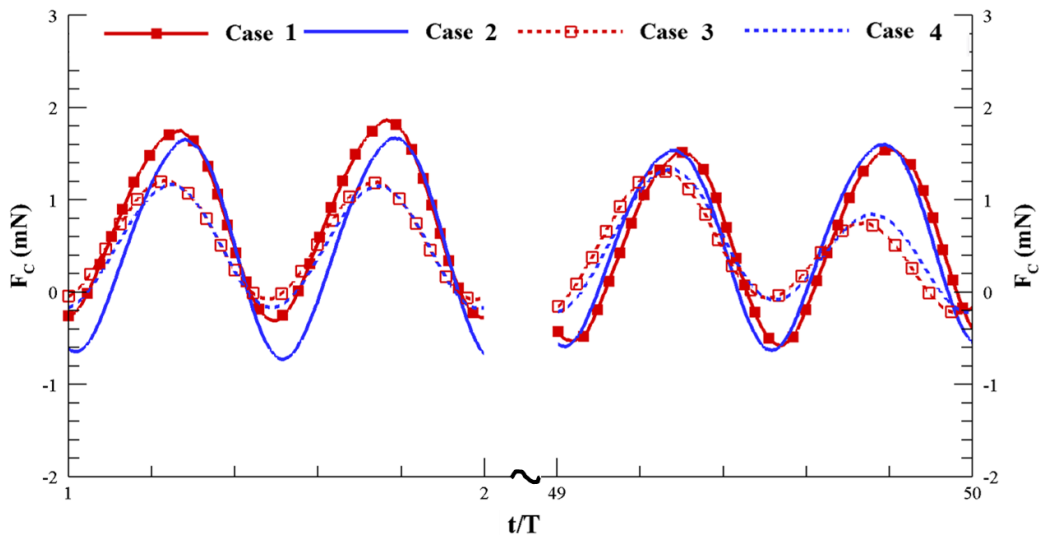
It can be seen that regardless of perturbation, the fish can always reach a quasi-steady status after an accelerating period. In still water, a BDAC model accelerates for 24 cycles, while it is 46 for the BC model. With the perturbation, it takes 19 cycles for the BDAC model to reach quasi-steady status, but this duration increases to 33 cycles for the BC model. The BC model spends almost twice the time of the BDAC model to become quasi-steady. As the model in the current gains a smaller velocity than in the still water, the duration of unsteady periods is shorter.

6.3.2 Hydrodynamic Forces

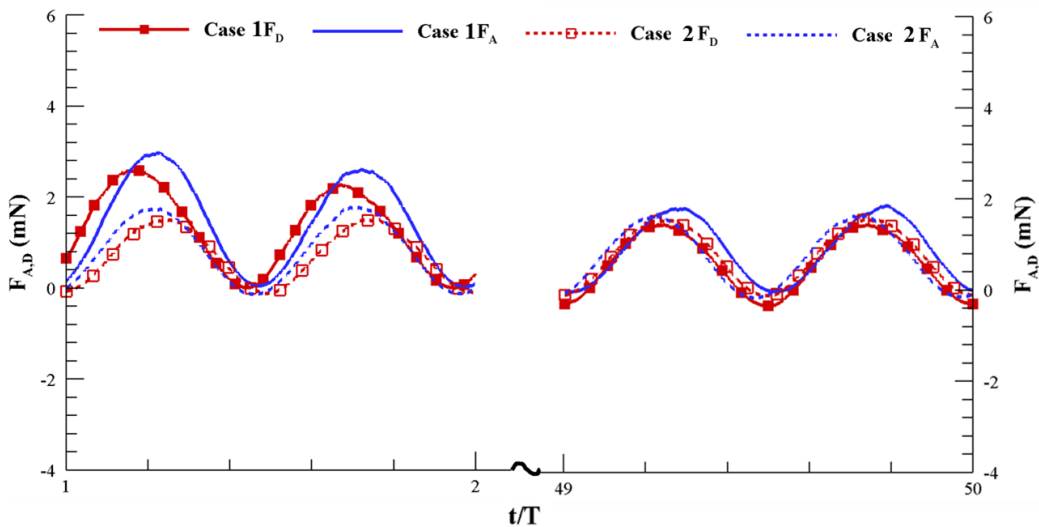
Figure 6.4 presents the development of the hydrodynamic forces during the 2nd and 50th periods. In the 2nd time-cycle, the velocity of both BDAC and BC models with the incoming current is negative, and all the models are in the accelerating stage. For the 50th period, the four cases are in the quasi-steady stage. The forces on fish body F_B , caudal fin F_C , dorsal and anal fins F_D , F_A and total force of the fish model F_T are presented. A negative value stands for resistance and a positive one represents propulsion. It was noted that in the quasi-steady stage, only slight differences could be found for these four cases between the models in the still water (Case 1, 3) and in the incoming current (Case 2 and 4).



(a) Force on fish body F_B



(b) Force on caudal fin F_C



(c) dorsal and anal force F_D, F_A

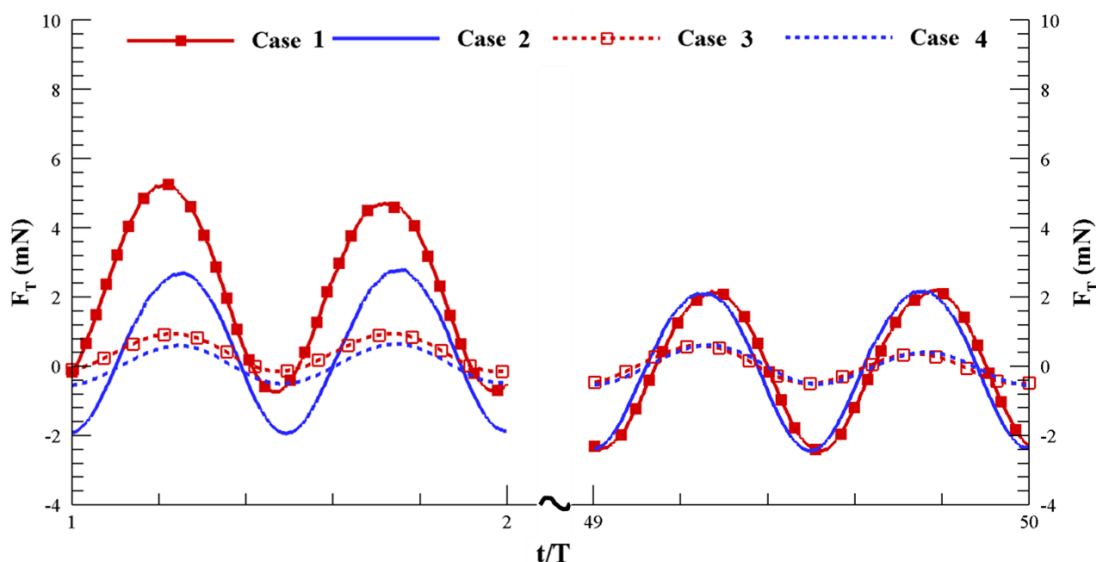
(d) Total force F_T

Figure 6.4 Force on the fish in 2nd and 50th period

For the hydrodynamic force on fish body F_B as shown in Figure 6.4(a), its value is negative for all four cases, which indicates that the force on the fish body is always resistance. During the accelerating stage, the body force of the model in the current is larger than that in still water. Meanwhile, the fish body with the dorsal and anal fins suffers a larger resistance than the model with only the caudal fin. After the velocity becomes quasi-steady, the force on the fish body is larger than that in the accelerating stage. As the fish body is rigid and cannot produce propulsive force, the value of its hydrodynamic force mainly depends on the speed of the model. A quicker speed will lead to a larger resistance on the body. For the fish propelling in the current in the 2nd period, the relative value of velocity is greater than the fish propelling in still water. Moreover, with dorsal and anal fins, the fish swims faster than that only with caudal fin. Thus, F_B of the Case 2 and Case 3 is the largest and smallest one for the four cases in the 2nd period, respectively.

There is no obvious difference on the force of caudal fin between fish swimming in still water and in the incoming current during the accelerating stage for the BC model,

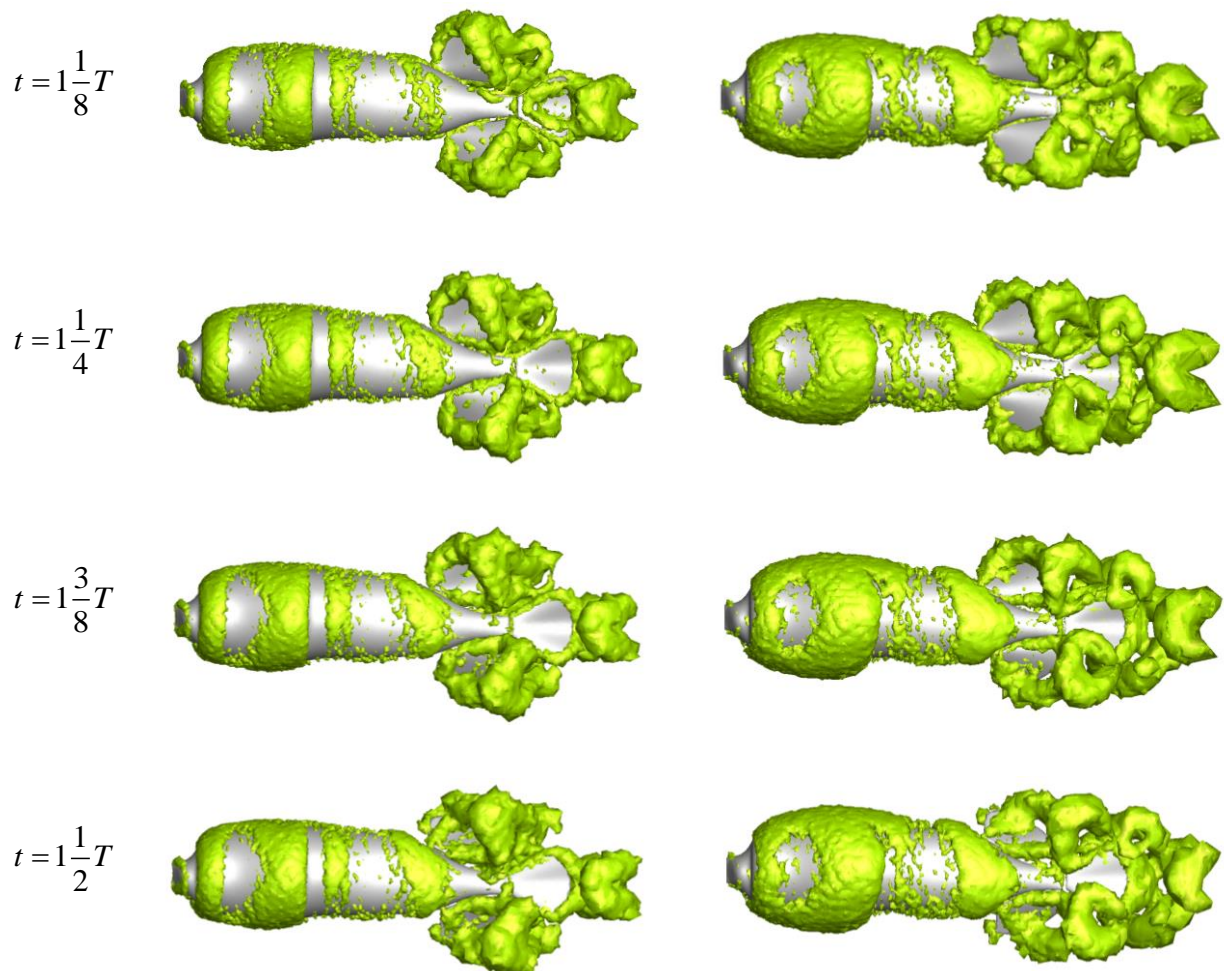
as shown in Figure 6.4(b). Comparing with the BDAC model, the force generated by caudal fin in the BC model is relatively smaller. A single caudal fin can only generate such a small force that is unable to propel the fish forward fast. It was noted that with the dorsal and anal fins, the force on the caudal fin in Cases 1 and 2 becomes larger. Thus, the dorsal and anal fins help the caudal fin to generate a larger propulsive force. This may be explained by the fact that the caudal fin is located in the downstream of the dorsal and anal fins, thus it can absorb energy from the vortices generated by the upstream fins.

Figure 6.4(c) shows the force of the dorsal and anal fins in Cases 1 and 2. For both conditions, the anal fin generates a larger force than the dorsal fin. Both fins generate positive forces during acceleration. Some differences could also be found between the conditions with the fish swimming in still water and in the current. It is seen that the dorsal and anal fins of the BDAC model could generate a larger propulsive force in still water than in the incoming current during the accelerating stage. When the fish accelerates, the dorsal and anal fins play more important roles in propelling than the caudal fin. The forces on all fins become smaller when the fish reaches the cruising speed, and the force generated by the dorsal fin is almost equal to that produced by the caudal fin.

The total forces experienced by the models are also presented in Figure 6.4(d). For the self-propelled fish in still water, the total force is almost positive during the accelerating stage. However, when the fish swims in the incoming current, its total force fluctuates around 0 with a small averaged positive value. In the 2nd period, the total force in still water is greater than that in the current for both models. Meanwhile, the BDAC model generates larger total force than the BC model. This is because the BDAC model has dorsal, anal and caudal fins as three propellers, but the BC model only has a caudal fin. Moreover, the force on the caudal fin of the BC model becomes smaller without the dorsal and anal fins.

6.3.3 Vorticity Structure

To have a better understanding of the differences between the fish with and without dorsal and anal fins, the formation of vorticity structures for the four cases is illustrated in Figure 6.5 and Figure 6.6. The time span analysed is set to the 2nd cycle, because during this period the self-propelled fish in still water accelerates forward and the velocity is positive. On the contrast, the model in the current is flushed backward with a negative velocity. Thus, the vortex structure could be representative to explain the differences between the models with and without dorsal and anal fins under various conditions.



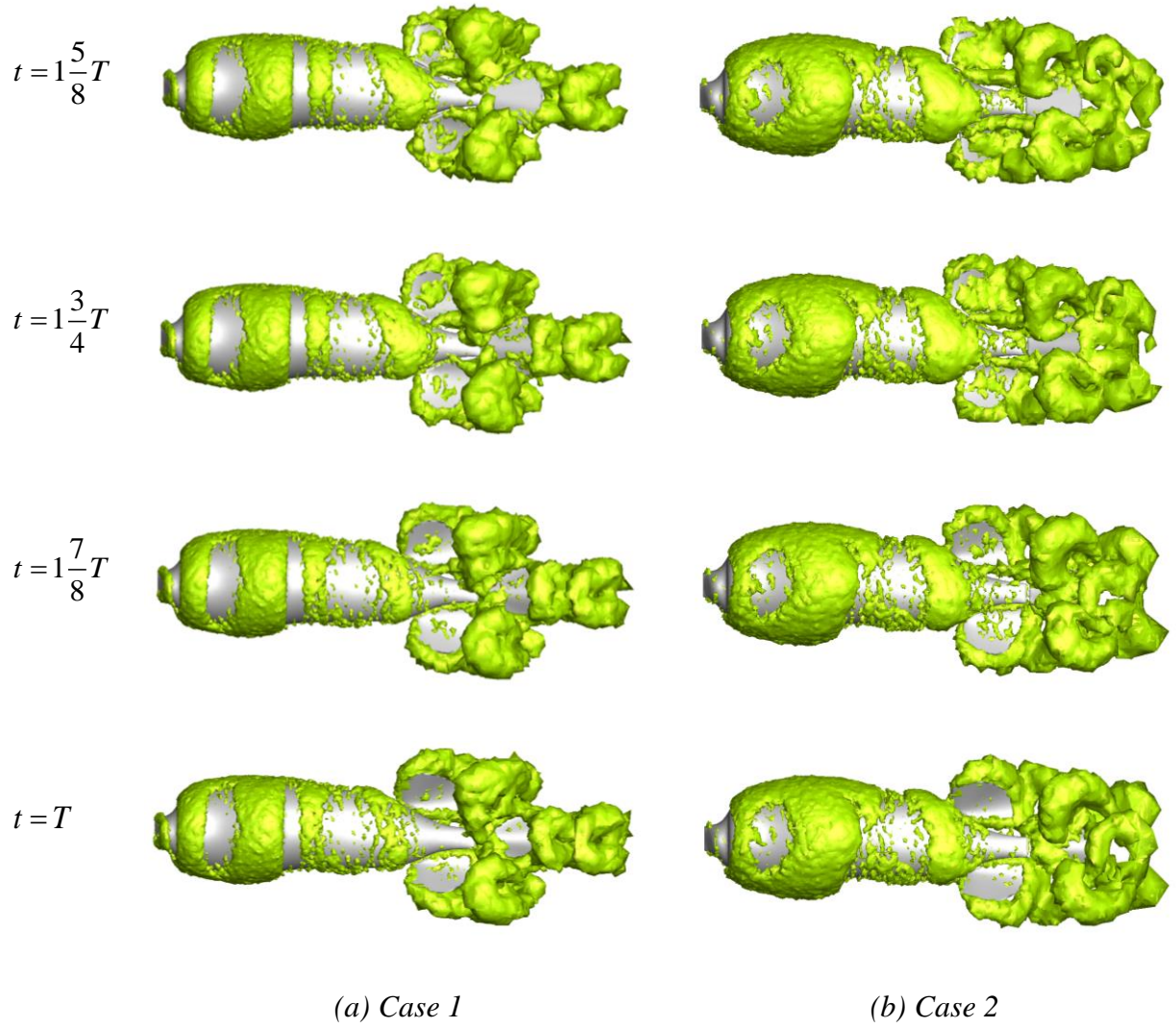
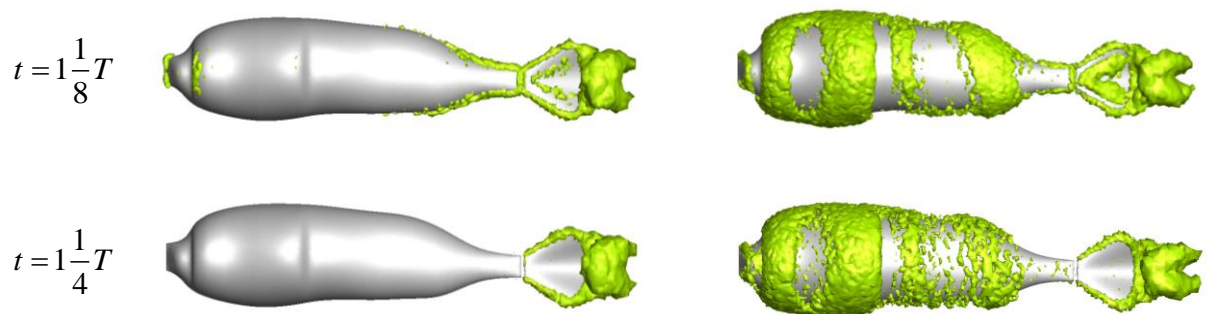


Figure 6.5 Vortex structures for Case 1 and Case 2 during the 2nd time period



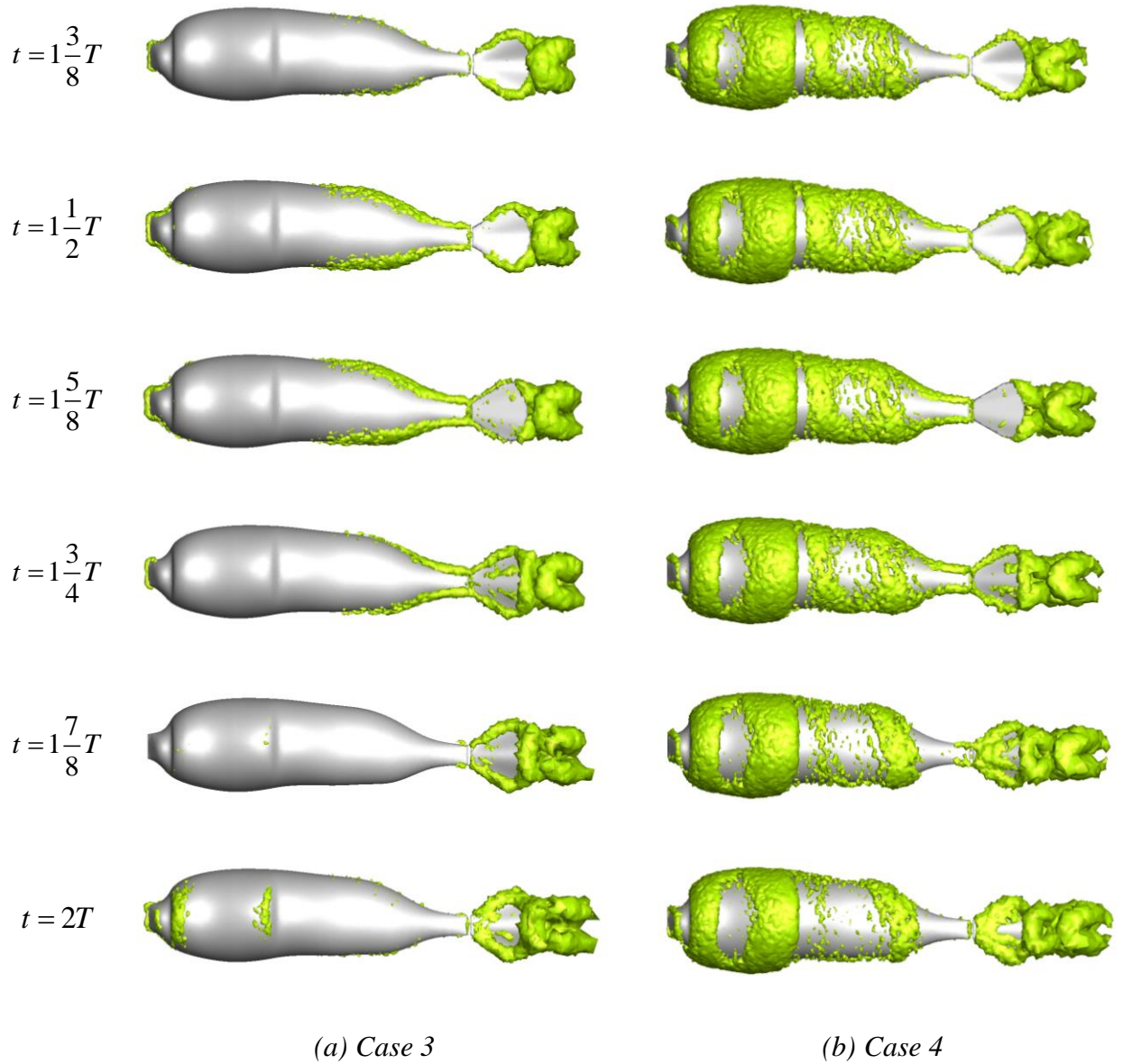


Figure 6.6 Vortex structures for Case 3 and Case 4 during the 2nd time period

Comparing the vortices generated by the fish swimming in still water and in the current, one obvious difference is that the vortices on the fish body become stronger when the fish swims in the current. This is also reflected on the body force, i.e., the drag force on body is larger for the fish swimming in the current. As the fish faces the incoming current and moves backward, its relative velocity is larger than the fish swimming in still water at the same moment. Thus, the fish body suffers more resistance than that

in the still water, especially the widest part as shown in the Figure 6.5(b) and Figure 6.6(b).

For the BDAC model in still water, the vortices generated by the dorsal and anal fins are still developing, whereas in the current condition they are already shed off and merge with those produced by the caudal fin. The velocity of the incoming current could be responsible for this as it drives the shed vortices to move further downstream compared to the still water condition.

Another difference is about the shedding duration of vortices behind the caudal fin. Comparing the two models in still water at the same instant reveals that vortices are found to form faster and shed off quicker. For example, at $t = 1\frac{5}{8}T$, a new vortex ring is being generated for BC model in the current and is going to be formed for that in the still water. It entirely shed off at $t = 2T$ in the current and at the same instant, this vortex ring is only formed halfway in the still water.

Meanwhile, some differences in the wake could be found between the BDAC and BC models. An obvious one is that the vortices become narrow in the XZ view without dorsal and anal fins. For the BDAC model, vortices could be generated by three fins. However, only the caudal fin produces vortices in the BC model. The vortices shed by the caudal fin in the BC model is found to be weaker than that in the BDAC model. This could be associated with the differences in the hydrodynamic force as well as swimming velocity of the two models.

6.3.4 Power and Efficiency

Values of the power and efficiency for the four cases are given in Table 6.2. Based on the definition in the Equation (3.42), the averaged consumed power P_c of a model in either still water or the incoming current remains the same. Thus, Case 1 and Case 2 have the same consumed power. This is also true for Case 3 and Case 4. For the output

power P_{out} , the results are quite different as presented in Figure 6.7. The BDAC model in still water and the BC model in the current has the largest and smallest output power among the four cases, respectively.

Table 6.2 Averaged power and efficiency

Case No.	1	2	3	4
Averaged Output power \bar{P}_{out} (mW)	0.217	0.023	0.021	0.003
Averaged Consumed power \bar{P}_c (mW)	0.544	0.544	0.181	0.181
Efficiency η_{eff}	39.89%	4.17%	11.52%	1.44%

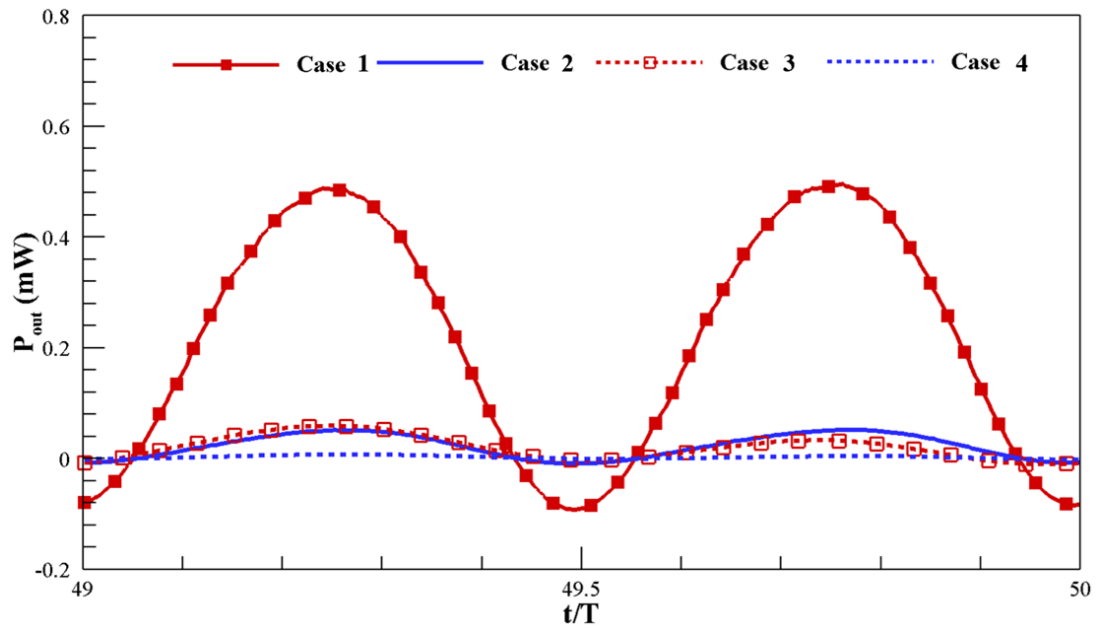


Figure 6.7 Output power in the 50th period

Without the dorsal and anal fins, the consumed power of the BC model in still water reduces by 66.73% compared to the BDAC model. However, its output power falls dramatically to only 9.68% of the BDAC model. For the swimming condition in the current, the output power of the BD model also drops considerably to 86.96% of the BDAC model. From these results, it is noted that the output power of the fish with only

the caudal fin decreases significantly in both still water and incoming current conditions, and the efficiency of the BC model is lower than half of the BDAC under the same flow condition. These results clearly demonstrate that with only the caudal fin, the swimming efficiency of the pufferfish is very low while the dorsal and anal fins play important roles in improving the output power, i.e., the useful power, as well as the efficiency.

6.4 Discussions

It is noted that in the quasi-steady swimming stage, there are two frequencies present for the velocity and force results of the BC model, as shown in Figure 6.3 and Figure 6.4. The two different peak values mean that the fish has an induced yaw angle with respect to the forward swimming direction. With the dorsal and anal fins, this angle is not found and only one frequency exists in the results of quasi-steady swimming. To verify that the angle is caused by the yaw motion and can be prevented by the dorsal and anal fins, another simulation is carried out where the self-propelled motion of the BC model in the still water is analysed while its rotational motions are constrained.

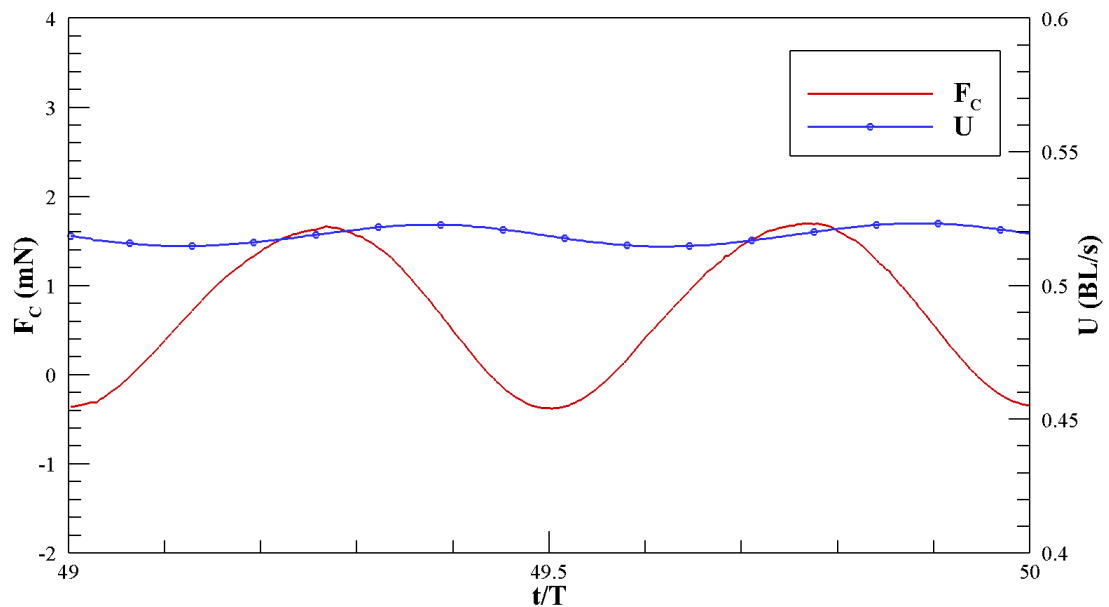


Figure 6.8 Hydrodynamic force F_C on caudal fin and the induced velocity U of the self-propelled BC model in the still water in 50th period

Results about the hydrodynamic force on the caudal fin F_c and the final induced velocity U during the 50th period (in the quasi-steady swimming stage) are given in Figure 6.8. It could be seen that the two peak values are almost identical for the BC model by constraining the rotational motions. This proves that the different peaks result from the rotational motions and the dorsal and anal fins could prevent the yaw motion of the model. Meanwhile, without the induced yaw angle, the BC model in still water could gain a larger velocity compared with the result from Case 3.

6.5 Concluding remarks

In this chapter, the role of dorsal and anal fins during unsteady swimming of a pufferfish is presented. Following the geometry and kinematic profiles of the pufferfish in Chapter 5, a perturbation in the form of a specified incoming current is applied to the self-propelled BDAC model. Furthermore, a BD model is constructed by removing the dorsal and anal fins are removed. Self-propelled motions are simulated for the two models in both still water and the incoming current. Results are compared and analysed in terms of motions, hydrodynamic forces, vorticity structure as well as power and efficiency.

It was firstly found that for both fish models in the current, the displacement negatively increases first, researches its largest value, and decreases to zero during the first several periods. The change of displacement is in relation with the velocity development. The difference of velocity and displacement between the BDAC and BC models in the current lies in the time each model takes to return to positive swimming velocity, i.e., moving forward. Without the dorsal and anal fins, it takes the BD model longer time to achieve positive velocity as well as quasi-steady swimming stage.

By comparing the hydrodynamic forces between the two models, it was found that difference also exists during the period when displacement is still negative. The hydrodynamic force of the fish body in the BDAC model is larger than that in the BC model. Meanwhile, the force generated by the caudal fin of the BDAC model is larger

than that of the BC model. One notable point is that after quasi-steady swimming, the BC model has two frequencies for the forces in both still water and current. This phenomenon could be eliminated by constraining the rotational motions, which means that the dorsal and anal fins play important roles in maintaining the swimming course.

Furthermore, analysis of the vorticity structures shows that without the dorsal and anal fins, the vortices generated by the BC model become narrower than the BDAC model. Without dorsal and anal fins, the distribution of the vortices on the fish body changes a lot. In the still water, the vortices gather mostly in the front of the fish body in the BDAC model while they appear at the head and posterior part of the body in the BC model.

Lastly, the output power for the BC model in the current is found to be extremely small. This could be reflected on the small swimming velocity of the BC model in both still water and current. The results demonstrate that if a pufferfish can only be propelled by its caudal fin, its swimming efficiency will be quite low.

Chapter 7 Conclusions, Discussions and Future Work

In order to analyse the complicated mechanisms between the surrounding fluid and the fish during different fish swimming, as well as the physics behind the deformation of fish morphology, a multibody-based analysis tool is developed in this thesis coupling with a fluid solver. Validation studies for this coupled tool are carried out first and self-propelled simulations of real fish are then conducted. Conclusions drawn from these studies are firstly reviewed in Section 7.1. Subsequently, some recommendations for future improvements and potential applications are provided in Section 5.

7.1 Conclusions

The main outcomes of this thesis are summarised as follows.

7.1.1 Four Kinds of Aquatic Biomimetic Problems

A newly developed method was presented in Chapter 4 to solve bio-inspired swimming problems. The locomotion of fish and fins is simulated using the Multi-Body Dynamic theory and the fluid flow field around the fish is investigated with a CFD numerical method. Four case studies were tested, including a three-linked rigid-body swimmer, an anguilliform fish model, a cupping motion of a caudal fin and a pair of passive flapping wings. The first three studies can be categorised as actuated cases while the last one belongs to the so-called passive input method. Numerical results are compared with data from other available resources and good comparisons are made. It was noted that this new modelling tool can be applied to comprehensive studies on fish swimming behaviour.

7.1.2 Self-Propelled Pufferfish with Multiple Fins

The self-propelled motion of a CFD pufferfish model with multiple fins is studied in Chapter 5. Comparisons between rigid and flexible fins are carried out, focusing on

the impacts on the hydrodynamic performance of the fish during accelerating and quasi-steady swimming. The deformation of the fins is achieved by prescribing the motions to the whole fin surface, and the kinematics are obtained via a live fish experiment. The locomotion of the CFD model is calculated with the developed MBD method. The following conclusions are drawn from this study:

1. The velocity development of pufferfish has the same trend whether it is driven by rigid or flexible fins, i.e., the swimming velocity would reach a quasi-stable stage after a period of accelerating. The duration for accelerating, however, is affected by the rigidity of fins.
2. With a larger acceleration and a longer accelerating period, the fish with flexible fins can swim 1.6~2 times faster than that with rigid fins. Flexible fins mostly generate positive forces with a small fluctuation, but rigid fins produce both positive and negative forces with a large oscillation amplitude.
3. Dorsal and anal fins also contribute to the generation of propulsive forces under self-propelled conditions.
4. The energy from vortex shedding can be better utilised by the fish with flexible fins, which leads to less power consumption and further results in an enhanced efficiency compared to the one with rigid fins.

7.1.3 The Role of Dorsal and Anal Fins during Unsteady Fish Swimming

A self-propelled pufferfish with (BDAC model) and without (BC model) dorsal and anal fins is studied in Chapter 6 and analysis on the hydrodynamic performance of the pufferfish in the current and still water are carried out. The following conclusions are drawn from this study:

1. The main differences between the BDAC and BC models in the still water and current exist during the accelerating stage.

2. In still water, the BDAC model could gain a larger quasi-steady velocity within a shorter accelerating time, which is due to the additional thrust generated by the dorsal and anal fins.
3. With dorsal and anal fins, the force generated by the caudal fin is larger than that without dorsal and anal fins and this is further reflected in the vortex field.
4. In the current, the fish with dorsal and anal fins spends a shorter time to return to the positive motion.
5. The dorsal and anal fins could compensate the angular motion generated by the caudal fin and minimize the induced angle to make the fish gain a larger swimming velocity.

7.2 Discussions

This thesis addressed three types of problems that had been investigated in the past decades: body undulating motion, single fin, and fish motion with multiple fins. It should be admitted that there were some gaps between these reviewed studies and the realistic problems.

The first gap was between simplified models employed in numerical simulations and complicated morphology/kinematics of fish in reality. A simplified model would only provide limited reference for theoretical investigations rather than become a meaningful tool for realistic conditions. In order to gain more in-depth understandings on biomimetic problems, numerical simulations of bio-inspired locomotion should be more comprehensive. In Chapter 5, a realistic self-propulsive pufferfish model with either rigid or flexible fins was established for numerical investigations to reveal the mechanisms behind its excellent hydrodynamic performance. Subsequently, the roles of dorsal and anal fins were investigated in Chapter 6 by including or removing the fins in the fish-fin model.

The author believes that the conclusions drawn from this thesis can help improve the design of fish-inspired robots. The numerical results in Chapter 5 showed that flexibility of fins could enhance the efficiency of the self-propelled system. Thus, the fins of fish-inspired robots are recommended to be constructed with the ability to deform rather than as stiff members so as to improve their propulsion efficiency. Furthermore, it was found in Chapter 6 that the stability of fish during unsteady swimming conditions could be improved by the inclusion of dorsal and anal fins. As a result, multiple fins should also be included for better stability when designing these robots for complex flow conditions.

Moreover, the author thinks that future designs of AUV could also draw on the experience of the self-propelled study in the present thesis. As mentioned in Section 1.1.1, AUV carries its power system for propulsion and the requirement of battery endurance is high. A new concept about the improvement on its propelling system is that besides the one propeller configuration traditionally adopted in AUV, multiple fin-like propellers can be installed just like fish. These bio-inspired propellers could be used either as an alternative method for propulsion under some emergent conditions or as a way to extract energy from wake structures for battery-charging purposes.

A second gap existed between the previous methodology and various kinds of fish locomotion. An ideal numerical tool should be suitable for different kinds of locomotion, rather than a specific type of fish motion. In this thesis, a numerical tool based on the MBD method was developed, which was able to simulate various types of aquatic animals. Both BCF and MPF swimmers can be simulated with the current MBD tool as demonstrated with the cases in Chapter 4, Chapter 5 and Chapter 6. In nature, fish use their pectoral fins for intricate manoeuvring motions such as turning, diving, and going up. By adding pectoral fins into the fish model and extending the present tool with a control system, the manoeuvrability of fish can be investigated with the numerical tool. Detailed information on flow field and fish motion dynamics can help understand the underlying mechanisms of fish manoeuvring, which will provide guidance for designing fish-inspired robots and AUV with improved manoeuvrability.

There are also some weaknesses that need to be improved in the present work. Firstly, as the flow field surrounding the fish was solved with the CFD method to obtain the hydrodynamic forces, one thing that must be mentioned is the computational efficiency. A well-agreed conception is that CFD simulations are relatively time-consuming. Taking the study of the self-propelled pufferfish in Chapter 5 as an example, the simulations were carried out on the High Performance Computer (HPC) of ARCHI-WeSt using two 2.0 GHz, 20-core Intel Xeon Gold 6138 CPUs, i.e., 40 cores in total. The overall CPU time for a single case was approximately 36 hours, which is rather long for design purposes. Nevertheless, recent progress in computer technology, e.g. GPU-accelerated computing and machine learning, has provided a promising solution to this issue.

The other weakness is the stability of present numerical simulations, which typically occurred at the beginning of calculations due to the strong change of the fluid field. This is related to the coupling procedure between the CFD solver and the MBD tool. In the current method, the data transfer between the two codes only happens once in one time step, which is normally referred to as “weak” coupling. The CFD simulations were found to be quite sensitive to the quality of computational grid and solver parameters. Through trial and error, convergence could only be achieved by applying the Fractional Step Method provided in ANSYS Fluent for velocity-pressure decoupling as well as carefully selecting mesh and solver settings. A more practicable method to overcome this weakness is to establish a “strong” coupling method, i.e., transferring data between the two codes more than once within each time step until certain convergence criteria are satisfied.

7.3 Recommendations for future work

This research focuses on the development of a multibody-based tool to solve the complicated motions of various types of fish swimming, and it can be coupled with fluid solver to analyse the complex fluid field and reveal the hydrodynamic mechanisms. However, due to the limited time and computational resource available,

the present tool still has some shortcomings and numerical analysis for different fish swimming was carried out under only a small number of motion conditions. Recommendations for further improvements to the tool and potential applications are briefly outlined below.

1. Future simulations can take into consideration more complicated and vivid motions of real fish, such as diving, rising, and sudden starting. In the present studies, pectoral fins are omitted. However, some motions in nature highly depend on the cooperation of different fins as well as the body of the fish. When investigating the manoeuvring, it is thus necessary to consider the pair of pectoral fins.
2. The functions of dorsal and anal fins during unsteady fish swimming are worth further investigation. In Chapter 6, two conditions of dorsal and anal fins are considered: undulating fins and no fins. A third condition can be simulated by keeping the fins in the model but without imposing any motions. Comparisons between the new condition and the other two conditions can help reveal the unsteady swimming mechanisms of fish with dorsal and anal fins.
3. The MBD tool developed in the present work is only applied to fish models. One of its future applications is to simulate the locomotion of underwater vehicles and further optimize the combination of aquatic animal swimming and unmanned underwater vehicles from the viewpoints of both morphology and hydrodynamic performance.
4. Control systems are essential for both real fish and unmanned underwater vehicles. However, a control module is currently not implemented in the present coupled tool. Future development of this code can focus on adding control functionalities so that numerical models can be utilised to simulate fish motions or vehicle operations closer to reality, e.g. object tracking and obstacle dodging.

5. The present MBD method provides a new idea to the development of future bio-inspired robots, i.e., modular units to adapt more complicated environment. For example, traditional methods are only capable of simulating an aquatic animal or a reptile. With the present conception of an MBD approach, the modelling of amphibious animals could be easily achieved by adding different functional modular units. Meanwhile, numerical simulations of experiments with modular units can be also carried out to support and help understand experimental results.

6. As the coupling method between the present MBD tool and the CFD solver only requires data transfer between the two codes once in one time-step, numerical convergence is very sensitive to the solver selection in ANSYS Fluent, mesh distribution and time-step size. For the future work, one way to improve its computational accuracy and stability is to change the frequency of data transfer from once to more times until results are converged. This could be considered as a strong coupling approach and it could significantly improve the stability of this tool, especially for unsteady simulations.

References

- Abbaspour M, Ebrahimi M (2015). Comparative numerical analysis of the flow pattern and performance of a foil in flapping and undulating oscillations. *Journal of Marine Science and Technology*, **20**(2), 257-277.
- Adkins D, Yan YY (2006). CFD Simulation of Fish-like Body Moving in Viscous Liquid. *Journal of Bionic Engineering*, **3**(3), 147-153.
- Anderson EJ, McGillis WR, Grosenbaugh MA (2001). The boundary layer of swimming fish. *Journal of Experimental Biology*, **204**(1), 81-102.
- Anderson JM, Chhabra NK (2002). Maneuvering and Stability Performance of a Robotic Tuna. *Integrative and Comparative Biology*, **42**(1), 118-126.
- ANSYS Fluent. ANSYS Fluent UDF Manual Release 15.0. 2013.
- Bhalla APS, Griffith BE, Patankar NA (2013). A Forced Damped Oscillation Framework for Undulatory Swimming Provides New Insights into How Propulsion Arises in Active and Passive Swimming. *PLoS Comput Biol*, **9**(6), e1003097.
- Blake RW, Chan KHS (2011). Biomechanics of swimming in the pufferfish *Diodon holocanthus*: propulsive momentum enhancement is an adaptation for thrust production in an undulatory median and paired-fin swimmer. *Journal of Fish Biology*, **79**(7), 1774-1794.
- Blidberg DR (2001). The development of autonomous underwater vehicles (AUV); a brief summary. *Ieee Icara*.
- Borazjani I (2013). The functional role of caudal and anal/dorsal fins during the C-start of a bluegill sunfish. *Journal of Experimental Biology*, **216**(9), 1658-1669.
- Borazjani I (2015). Simulations of Unsteady Aquatic Locomotion: From Unsteadiness in Straight-Line Swimming to Fast-Starts. *Integrative and Comparative Biology*, **55**(4), 740-752.
- Borazjani I, Daghooghi M (2013). The fish tail motion forms an attached leading edge vortex. *Proceedings of the Royal Society B: Biological Sciences*, **280**(1756).
- Borazjani I, Sotiropoulos F (2008). Numerical investigation of the hydrodynamics of carangiform swimming in the transitional and inertial flow regimes. *Journal of Experimental Biology*, **211**(10), 1541-1558.
- Borazjani I, Sotiropoulos F (2009). Numerical investigation of the hydrodynamics of anguilliform swimming in the transitional and inertial flow regimes. *Journal of Experimental Biology*, **212**(4), 576-592.
- Borazjani I, Sotiropoulos F (2010). On the role of form and kinematics on the hydrodynamics of self-propelled body/caudal fin swimming. *Journal of Experimental Biology*, **213**(1), 89-107.

- Borazjani I, Sotiropoulos F, Tytell ED, Lauder GV (2012). Hydrodynamics of the bluegill sunfish C-start escape response: three-dimensional simulations and comparison with experimental data. *The Journal of Experimental Biology*, **215**(4), 671-684.
- Broering TM, Lian Y-S (2012). The effect of phase angle and wing spacing on tandem flapping wings. *Acta Mechanica Sinica*, **28**(6), 1557-1571.
- Carling J, Williams TL, Bowtell G (1998). Self-propelled anguilliform swimming: simultaneous solution of the two-dimensional Navier-Stokes equations and Newton's laws of motion. *Journal of Experimental Biology*, **201**(23), 3143-3166.
- Chao L-M, Cao Y-H, Pan G (2017). A review of underwater bio-mimetic propulsion: cruise and fast-start. *Fluid Dynamics Research*, **49**(4), 044501.
- Chen J, Friesen W, Iwasaki T (2011). Mechanisms underlying rhythmic locomotion: body–fluid interaction in undulatory swimming. *Journal of Experimental Biology*, **214**(4), 561-574.
- Coral W, Rossi C, Martin IP (2015). Bio-inspired morphing caudal fin using shape memory alloy composites for a fish-like robot: Design, fabrication and analysis. *2015 12th International Conference on Informatics in Control, Automation and Robotics (ICINCO)*, Colmar, France, 336-343.
- Cui Z, Gu X, Li K, Jiang H (2017). CFD Studies of the Effects of Waveform on Swimming Performance of Carangiform Fish. *Applied Sciences*, **7**(2), 149.
- David MJ, Govardhan RN, Arakeri JH (2017). Thrust generation from pitching foils with flexible trailing edge flaps. *Journal of Fluid Mechanics*, **828**, 70-103.
- Dong H, Mittal R, Bozkurttas M, Najjar F, Wake Structure and Performance of Finite Aspect-Ratio Flapping Foils, in 43rd AIAA Aerospace Sciences Meeting and Exhibit. 2005, American Institute of Aeronautics and Astronautics. p. AIAA 2005-0081.
- Drucker EG, Lauder GV (2001). Locomotor function of the dorsal fin in teleost fishes: experimental analysis of wake forces in sunfish. *Journal of Experimental Biology*, **204**(17), 2943-2958.
- Eldredge JD (2006). Numerical simulations of undulatory swimming at moderate Reynolds number. *Bioinspiration & Biomimetics*, **1**(4), S19.
- Eldredge JD (2007). Numerical simulation of the fluid dynamics of 2D rigid body motion with the vortex particle method. *Journal of Computational Physics*, **221**(2), 626-648.
- Eldredge JD (2008). Dynamically coupled fluid–body interactions in vorticity-based numerical simulations. *Journal of Computational Physics*, **227**(21), 9170-9194.
- Esfahani JA, Barati E, Karbasian HR (2013). Effect of caudal on hydrodynamic performance of flapping foil in fish-like swimming. *Applied Ocean Research*, **42**(Supplement C), 32-42.

- Feeny BF (2008). A complex orthogonal decomposition for wave motion analysis. *Journal of Sound and Vibration*, **310**(1), 77-90.
- Feeny BF, Feeny AK (2013). Complex Modal Analysis of the Swimming Motion of a Whiting. *Journal of Vibration and Acoustics*, **135**(2), 021004.
- Gordon M, Plaut I, Kim D (1996). How puffers (Teleostei: Tetraodontidae) swim. *Journal of Fish Biology*, **49**(2), 319-328.
- Guido N, Siddhartha V, Dmitry A, Diego R, Wim MvR, Petros K (2017). Synchronisation through learning for two self-propelled swimmers. *Bioinspiration & Biomimetics*, **12**(3), 036001.
- Habib M, Davim JP, Engineering Creative Design in Robotics and Mechatronics, in *Advances in Mechatronics and Mechanical Engineering 2013*.
- Han P, Liu G, Ren Y, Dong H (2016). Computational Analysis of 3D Fin-Fin Interaction in Fish's Steady Swimming. *ASME 2016 Fluids Engineering Division Summer Meeting FEDSM2016*, Washington, DC, USA, FEDSM2016-7699.
- Hu J (2016). *Numerical study on hydrodynamic performance of bio-mimetic locomotion*. Ph.D Thesis, University of Strathclyde, Glasgow, Scotland, UK.
- Hu J, Xiao Q (2014). Three-dimensional effects on the translational locomotion of a passive heaving wing. *Journal of Fluids and Structures*, **46**, 77-88.
- Hu K, Ren Z, Wang Y, Wang T, Wen L (2016). Quantitative hydrodynamic investigation of fish caudal fin cupping motion using a bio-robotic model. *2016 IEEE International Conference on Robotics and Biomimetics (ROBIO)*, 295-300.
- Hunt JC, Wray AA, Moin P, Eddies, streams, and convergence zones in turbulent flows, in *Studying Turbulence Using Numerical Simulation Databases*, 2. Proceedings of the 1988 Summer Program; p. p 193-208. 1988.
- Kajtar JB, Monaghan JJ (2012). On the swimming of fish like bodies near free and fixed boundaries. *European Journal of Mechanics - B/Fluids*, **33**, 1-13.
- Kanso E, Marsden JE, Rowley CW, Melli-Huber JB (2005). Locomotion of Articulated Bodies in a Perfect Fluid. *Journal of Nonlinear Science*, **15**(4), 255-289.
- Kara LF, George VL (2015). Passive mechanical models of fish caudal fins: effects of shape and stiffness on self-propulsion. *Bioinspiration & Biomimetics*, **10**(3), 036002.
- Kern S, Koumoutsakos P (2006). Simulations of optimized anguilliform swimming. *Journal of Experimental Biology*, **209**(24), 4841-4857.
- Khalil W. *Modeling and Control of Manipulators*. Nantes.
- Kim B, Park SG, Huang W, Sung HJ (2016). Self-propelled heaving and pitching flexible fin in a quiescent flow. *International Journal of Heat and Fluid Flow*, **62**, 273-281.

- Kourosh S, Qiang Z (2015). Performance of synchronized fins in biomimetic propulsion. *Bioinspiration & Biomimetics*, **10**(2), 026008.
- Krishnadas A, Ravichandran S, Rajagopal P (2018). Analysis of biomimetic caudal fin shapes for optimal propulsive efficiency. *Ocean Engineering*, **153**, 132-142.
- Lauder GV (2015). Fish locomotion: recent advances and new directions. *Annual Review of Marine Science*, **7**, 521-545.
- Lauder GV, Drucker EG (2002). Forces, fishes, and fluids: hydrodynamic mechanisms of aquatic locomotion. *Physiology*, **17**(6), 235-240.
- Lauder GV, Madden PGA (2007). Fish locomotion: kinematics and hydrodynamics of flexible foil-like fins. *Experiments in Fluids*, **43**(5), 641-653.
- Li G, Müller UK, van Leeuwen JL, Liu H (2012). Body dynamics and hydrodynamics of swimming fish larvae: a computational study. *Journal of Experimental Biology*, **215**(22), 4015-4033.
- Li G, Müller UK, van Leeuwen JL, Liu H (2016). Fish larvae exploit edge vortices along their dorsal and ventral fin folds to propel themselves. *Journal of The Royal Society Interface*, **13**(116).
- Li L, Li G, Li R, Xiao Q, Liu H (2018). Multi-fin kinematics and hydrodynamics in pufferfish steady swimming. *Ocean Engineering*, **158**, 111-122.
- Li N, Liu H, Su Y (2017). Numerical study on the hydrodynamics of thunniform bio-inspired swimming under self-propulsion. *PloS one*, **12**(3), e0174740.
- Li N, Su Y (2016). Fluid Dynamics of Biomimetic Pectoral Fin Propulsion Using Immersed Boundary Method. *Applied Bionics and Biomechanics*, **2016**, 22.
- Lighthill M (1960). Note on the swimming of slender fish. *Journal of Fluid Mechanics*, **9**(02), 305-317.
- Lighthill MJ (1970). Aquatic animal propulsion of high hydromechanical efficiency. *Journal of Fluid Mechanics*, **44**(2), 265-301.
- Lighthill MJ (1971). Large-Amplitude Elongated-Body Theory of Fish Locomotion. *Proceedings of the Royal Society of London. Series B. Biological Sciences*, **179**(1055), 125-138.
- Lindsey CC, 1 - Form, Function, and Locomotory Habits in Fish, in *Fish Physiology*, W.S. Hoar and D.J. Randall, Editors. 1978, Academic Press. p. 1-100.
- Liu G, Ren Y, Dong H, Akanyeti O, Liao JC, Lauder GV (2017a). Computational analysis of vortex dynamics and performance enhancement due to body-fin and fin-fin interactions in fish-like locomotion. *Journal of Fluid Mechanics*, **829**, 65-88.
- Liu H, Kolomenskiy D, Nakata T, Li G (2017b). Unsteady bio-fluid dynamics in flying and swimming. *Acta Mechanica Sinica*, **33**(4), 663-684.
- Liu J, Hu H (2010). Biological Inspiration: From Carangiform Fish to Multi-Joint Robotic Fish. *Journal of Bionic Engineering*, **7**(1), 35-48.

- Liu P, Liu Y, Huang S, Zhao J, Su Y (2018). Effects of Regular Waves on Propulsion Performance of Flexible Flapping Foil. *Applied Sciences*, **8**(6), 934.
- Maertens AP, Gao A, Triantafyllou MS (2017). Optimal undulatory swimming for a single fish-like body and for a pair of interacting swimmers. *Journal of Fluid Mechanics*, **813**, 301-345.
- MAINONG AI, AYOB AF, ARSHAD MR (2017). INVESTIGATING PECTORAL SHAPES AND LOCOMOTIVE STRATEGIES FOR CONCEPTUAL DESIGNING BIO-INSPIRED ROBOTIC FISH. *Journal of Engineering and Science Technology*, **12**(1).
- Nangia N, Bale R, Chen N, Hanna Y, Patankar NA (2017). Optimal specific wavelength for maximum thrust production in undulatory propulsion. *PLOS ONE*, **12**(6), e0179727.
- Ogata Y, Azama T, Moriyama Y (2017). Numerical investigation of small fish accelerating impulsively to terminal speed. *Journal of Fluid Science and Technology*, **12**(1), JFST0009-JFST0009.
- Park SG, Sung HJ (2018). Hydrodynamics of a self-propelled flexible fin in perturbed flows. *Mechanical Engineering Reviews*, **5**(1), 17-00286-17-00286.
- Porez M, Boyer F, Belkhiri A (2014a). A hybrid dynamic model for bio-inspired robots with soft appendages-Application to a bio-inspired flexible flapping-wing micro air vehicle. *IEEE International Conference on Robotics and Automation (ICRA'2014)*, Hong Kong, hal-00861321.
- Porez M, Boyer F, Ijspeert AJ (2014b). Improved Lighthill fish swimming model for bio-inspired robots: Modeling, computational aspects and experimental comparisons. *The International Journal of Robotics Research*, **33**(10), 1322-1341.
- Reid DA, Hildenbrandt H, Padding J, Hemelrijk C (2012). Fluid dynamics of moving fish in a two-dimensional multiparticle collision dynamics model. *Physical Review E*, **85**(2), 021901.
- Ren Z, Hu K, Wang T, Wen L (2016a). Investigation of Fish Caudal Fin Locomotion Using a Bio-inspired Robotic Model. *International Journal of Advanced Robotic Systems*, **13**(3), 87.
- Ren Z, Yang X, Wang T, Wen L (2016b). Hydrodynamics of a robotic fish tail: effects of the caudal peduncle, fin ray motions and the flow speed. *Bioinspiration & Biomimetics*, **11**(1), 016008.
- Roper DT, Sharma S, Sutton R, Culverhouse P (2011). A review of developments towards biologically inspired propulsion systems for autonomous underwater vehicles. *Proceedings of the Institution of Mechanical Engineers, Part M: Journal of Engineering for the Maritime Environment*, **225**(2), 77-96.
- Salazar R, Fuentes V, Abdelkefi A (2018). Classification of biological and bioinspired aquatic systems: A review. *Ocean Engineering*, **148**, 75-114.

- Sfakiotakis M, Lane DM, Davies JBC (1999). Review of fish swimming modes for aquatic locomotion. *IEEE Journal of Oceanic Engineering*, **24**(2), 237-252.
- Shoel K, Zhu Q (2009). Fluid–structure interactions of skeleton-reinforced fins: performance analysis of a paired fin in lift-based propulsion. *Journal of Experimental Biology*, **212**(16), 2679-2690.
- Shoel K, Zhu Q (2010). Numerical simulation of a pectoral fin during labriform swimming. *Journal of Experimental Biology*, **213**(12), 2038-2047.
- Shoel K, Zhu Q (2012). Leading edge strengthening and the propulsion performance of flexible ray fins. *Journal of Fluid Mechanics*, **693**, 402-432.
- Standen EM, Lauder GV (2005). Dorsal and anal fin function in bluegill sunfish *Lepomis macrochirus*: three-dimensional kinematics during propulsion and maneuvering. *Journal of Experimental Biology*, **208**(14), 2753-2763.
- Standen EM, Lauder GV (2007). Hydrodynamic function of dorsal and anal fins in brook trout (*Salvelinus fontinalis*). *Journal of Experimental Biology*, **210**(2), 325-339.
- Tangorra JL, Mignano AP, Carryon GN, Kahn JC (2011). Biologically derived models of the sunfish for experimental investigations of multi-fin swimming. *2011 IEEE/RSJ International Conference on Intelligent Robots and Systems*, 580-587.
- Toomey J, Eldredge JD (2008). Numerical and experimental study of the fluid dynamics of a flapping wing with low order flexibility. *Physics of Fluids (1994-present)*, **20**(7), -.
- Tytell ED (2006). Median fin function in bluegill sunfish (*Lepomis macrochirus*): streamwise vortex structure during steady swimming. *Journal of Experimental Biology*, **209**(8), 1516-1534.
- Uddin E, Huang W-X, Sung HJ (2015). Actively flapping tandem flexible flags in a viscous flow. *Journal of Fluid Mechanics*, **780**, 120-142.
- van Rees WM, Gazzola M, Koumoutsakos P (2013). Optimal shapes for anguilliform swimmers at intermediate Reynolds numbers. *Journal of Fluid Mechanics*, **722**, R3.
- Vorus WS, Taravella BM (2011). Anguilliform fish propulsion of highest hydrodynamic efficiency. *Journal of Marine Science and Application*, **10**(2), 163.
- Wang S, Zhang X, He G (2012). Numerical Simulation of a Three-Dimensional Fish-like Body Swimming with Finlets. *Communications in Computational Physics*, **11**(4), 1323-1333.
- Wang Z-L, Su Y-M, Yu X-Z, Wang X-F (2010). Experimental and numerical study on pectoral-fin propulsive system. *China Ocean Engineering*, **24**(3), 513-522.
- Webb PW (1984). Form and function in fish swimming. *Scientific American*, **251**, 72-82.

- Webb PW, The biology of fish swimming, in *The Mechanics and Physiology of Animal Swimming*, L. Maddock, Q. Bone, and J.M.V. Rayner, Editors. 1994, Cambridge University Press: Cambridge. p. 45-62.
- Webb PW, Weihs D (2015). Stability versus Maneuvering: Challenges for Stability during Swimming by Fishes. *Integrative and Comparative Biology*, **55**(4), 753-764.
- Wiktorowicz AM, Lauritzen DV, Gordon MS (2007). Powered control mechanisms contributing to dynamically stable swimming in porcupine puffers (Teleostei: *Diodon holocanthus*). *Experiments in Fluids*, **43**(5), 725-735.
- Xu Y, Wan D (2012). Numerical simulation of fish swimming with rigid pectoral fins. *Journal of Hydrodynamics, Ser. B*, **24**(2), 263-272.
- Yang L, Su Y, Xiao Q (2011). Numerical Study of Propulsion Mechanism for Oscillating Rigid and Flexible Tuna-Tails. *Journal of Bionic Engineering*, **8**(4), 406-417.
- Yu C-L, Ting S-C, Yeh M-K, Yang J-T (2011). Three-dimensional numerical simulation of hydrodynamic interactions between pectoral-fin vortices and body undulation in a swimming fish. *Physics of Fluids*, **23**(9), 091901.
- Yuan C, Liu G, Ren Y, Dong H (2015). Propulsive Performance and Vortex Interactions of Multiple Tandem Foils Pitching In Line. *Conference: 45th AIAA Fluid Dynamics Conference*, Dallas, TX, AIAA-2015-3220.
- Zhang X, Ni S, Wang S, He G (2009). Effects of geometric shape on the hydrodynamics of a self-propelled flapping foil. *Physics of Fluids*, **21**(10), 103302.
- Zhang Y, He J, Low K-H (2013). Numeric simulation on the performance of an undulating fin in the wake of a periodic oscillating plate. *International Journal of Advanced Robotic Systems*, **10**(10).
- Zhou K, Liu J, Chen W (2016). Numerical simulation of bionic foils in tandem arrangement. *Advances in Mechanical Engineering*, **8**(5), 1687814016649299.
- Zhou K, Liu J, Chen W (2017). Study on the Hydrodynamic Performance of Typical Underwater Bionic Foils with Spanwise Flexibility. *Applied Sciences*, **7**(11), 1120.
- Zhu Q, Shoele K (2008). Propulsion performance of a skeleton-strengthened fin. *Journal of Experimental Biology*, **211**(13), 2087-2100.
- Zhu Q, Shoele K, Numerical Modeling of the Performance of Ray Fins in Fish Locomotion, in *Natural Locomotion in Fluids and on Surfaces*, S. Childress, et al., Editors. 2012, Springer New York. p. 151-157.

Publications

Journal Articles

Li R, Xiao Q, Liu Y, *et al* (2020). Computational investigation on a self-propelled pufferfish driven by multiple fins. *Ocean Engineering*, 197, 106908.

Li R, Xiao Q, Liu Y, *et al* (2018). A Multi-Body Dynamics based numerical modelling tool for solving biomimetic problems. *Bioinspiration and Biomimetics*, 13(5), 056001.

Conference Papers

Li R, Xiao Q, Li L, *et al* (2017). Study of self-propelled pufferfish driven by multiple fins – a comparison between rigid and deformable fins. In Proceedings of the *ASME 36th International Conference on Ocean, Offshore and Arctic Engineering (OMAE2017)*. Trondheim, Norway. Paper No. OMAE2017-61066.

Li R, Xiao Q, Li L, *et al* (2016). Multi-body dynamics modelling on a self-propelled pufferfish with its application in AUV. In Proceedings of the *10th Symposium on High-Performance Marine Vehicles (HIPER'16)*. Cortona, Italy.

Li R, Jia L, Xiao Q (2014). A study of vortex ring generation by a circular disc with its application in bionic investigation. In Proceedings of the *2nd International Conference on Maritime Technology (ICMT2014)*. Glasgow, UK.